Syawaluddin Akbar

Numerical Simulation of Deposit Formation in Coal-Fired Utility Boilers with Biomass Co-Combustion

Numerical Simulation of Deposit Formation in Coal-Fired Utility Boilers with Biomass Co-Combustion

Von der

Fakultät Energie-, Verfahrens- und Biotechnik

der Universität Stuttgart

zur Erlangung der Würde eines

Doktors der Ingenieurwissenschaften (Dr.-Ing.)

genehmigte Abhandlung

vorgelegt von

Syawaluddin Akbar

aus Kendari, Indonesien

Hauptberichter: Prof. Dr. techn. Günter Scheffknecht

Mitberichter: Prof. Dr.-Ing. Roman Weber

Tag der mündlichen Prüfung: 29.07.2011

Institut für Feuerungs- und Kraftwerkstechnik

der Universität Stuttgart

2011

Vorwort

Die vorliegende Arbeit entstand während meiner Tätigkeit am Institut für Feuerungs- und Kraftwerkstechnik (IFK) der Universität Stuttgart, mit Förderung des Deutschen Akademischen Austauschdienstes (DAAD).

Dem Leiter des Instituts, Herrn Prof. Dr. techn. Günter Scheffknecht danke ich für das große Interesse an diesem Thema und die Übernahme des Hauptberichts. Weiterhin danke ich Herrn Prof. Dr.-Ing. Roman Weber für die Übernahme des Mitberichts.

Mein herzlicher Dank gilt außerdem allen Kolleginnen und Kollegen des IFK für die zahlreichen fachlichen Diskussionen und für die äußerst angenehme Arbeitsatmosphäre. Vor allem Herrn Prof. Dr.-Ing. Uwe Schnell, Leiter der Abteilung Feuerungs- und Dampferzeugersimulation (FDS), bin ich zu großem Dank verpflichtet für sein großes Interesse an meiner Arbeit und seine immerwährende Unterstützung während meiner Tätigkeit am IFK. Weiterhin schulde ich meinen Kollegen und ehemaligen Kollegen von FDS, namentlich die Herren Christoff Deeg, Heiko Dieter, Ju Pyo Kim, Mohammed Anany, Simon Leiser, Alan Matschke, Jens Hetzer, Michael Müller, Olaf Lemp, Dominik Kurz, Navid Ghavami und Claus Nagel großen Dank für die hervorragende Kooperation und die inspirierende Arbeitsatmosphäre. Bei Herrn Dr.-Ing. Timm Heinzel möchte ich mich ganz besonders für die Bereitstellung von Meßdaten und die fachlichen Diskussionen bedanken.

Nicht zuletzt bedanke ich mich sehr herzlich bei meiner Familie für die anhaltende Unterstützung und beinahe unendliche Geduld während der Fertigstellung der Arbeit.

Stuttgart, im September 2011   Syawaluddin Akbar

Contents

List of Symbols

Latin Symbols

Symbol	Unit	Meaning
A	$kg\,s^{-1}$	coefficient in discretised transport equation
A_j	—	the name of species j
A_p	$m^2\,kg_{char}^{-1}$	specific surface area of particle
A_p	m^2	the projected frontal area of the particle (equation 2.59)
c_j	$kmol\,m^{-3}$	molar concentration of species j
c_G	$kmol\,m^{-3}$	total gas concentration
c_p	$J\,kg^{-1}K^{-1}$	specific heat capacity
c_{p0}	$J\,kg^{-1}K^{-1}$	specific heat capacity at the reference temperature, T_0
C	$kg\,m^{-2}\,s^{-1}$	condensation rate
C	—	concentration
C_{Cun}	—	the Cunningham correction
d_p	m	particle diameter
d_t	m	tube diameter
d^+	—	dimensionless particle diameter
D_k	$m^2 s^{-1}$	diffusion coefficient of the species k
E_i	$J\,kmol^{-1}$	activation energy of reaction i
E	—	the Prandtl empirical constant, E = 9.0
f_{Trans}	—	impaction efficiency
f_{stick}	—	sticking probability
f_{melt}	—	melt fraction
F	—	the fraction of the conductivity attributed to the gas (section 3.5)
F_D	N	drag force
F_{ex}	N	sum of all external volume forces
g_i	ms^{-2}	gravity in the ith direction
G_k	$J\,s^{-1}$	production term of turbulent kinetic energy
h	$J\,kg^{-1}$	specific enthalpy
I	$kg\,m^{-2}\,s^{-1}$	impaction rate

Symbol	Unit	Meaning
J_{kj}	$kg_k\,m^{-2}s^{-1}$	molecular mass flux of species k in the jth space coordinate
k	$m^2\,s^{-2}$	turbulent kinetic energy
$k_{0,i}$	*	pre-exponential factor of reaction i
k_c	$m\,s^{-1}$	mass transfer coefficient
k_i	*	rate coefficient of reaction i, e.g. k_1, k_2, k_{bon}, k_{dec}, or k_{eff}
k_{Ersn}	—	erosivity of impacting ash particles (equation 3.61)
K_i	—	equilibrium constant of reaction i
Kn	—	Knudsen number
K	$W\,m^{-1}K^{-1}$	thermal conductivity
K_D	—	a constant depending on material (equation 3.16)
L	m	characteristic length
L_i	m	thickness of layer i
m	kg	mass
$\dot{m}_{C,i}$	$kg\,m^{-2}\,s^{-1}$	mass flux of species i
$m_{p,i}$	kg	mass of single particle of class i
M_{M_i}	$kg\,kmol^{-1}$	molecular weight of a species i
n	—	reaction order
$\dot{n}_{C,i}$	$kmol\,m^{-2}\,s^{-1}$	molar flux of species i
$\dot{n}_{inert}$	$kmol\,m^{-2}\,s^{-1}$	molar flux of an inert gas
N_i	—	the number of particles impacting the surface (Fig. 3.8)
N_C	—	the number of particles towards the surface (Fig. 3.8)
P_{stick}	—	ash sticking probability
p	$N\,m^{-2}$	static pressure
p_i	bar	partial pressure of species i
p_0	$N\,m^{-2}$	reference pressure, $p_0 = 1.01325 \times 10^5\,N\,m^{-2}$
$\overline{p}$	$N\,m^{-2}$	average pressure
p^*	$N\,m^{-2}$	estimated value of pressure
p'	$N\,m^{-2}$	a mass-conserving pressure-correction term
p'_{sm}	$N\,m^{-2}$	a smoothing pressure-correction term
$\bar{p}^*$	$N\,m^{-2}$	a multidimensional averaged pressure in respect to the estimated pressure p^* (see equation 2.32)
Pr	—	Prandtl number
$\dot{q}$	$W\,m^{-2}$	heat flux
Re	—	Reynolds number
Sc	—	Schmidt number

Symbol	Unit	Meaning
Sh	—	Sherwood number
Stk	—	Stokes number
S_ϕ	*	source term per unit volume of any independent variable ϕ
S_h	$J\,m^{-3}\,s^{-1}$	source term of specific enthalpy per unit time and unit volume
S_{Y_k}	$kg_k\,m^{-3}s^{-1}$	source term; rate of production (or consumption) of species k per unit volume
t_E	s	the characteristic eddy life time
t	s	time
T	K	temperature
T_0	K	reference temperature $T_0 = 273.15\,K$
T^*	K	temperature in the fine structure
u	$m\,s^{-1}$	x-component of velocity
$u_{d,turb}$	$m\,s^{-1}$	turbulent deposition velocity
u_j	$m\,s^{-1}$	velocity component in the jth space coordinate
$u_{p,i}$	$m\,s^{-1}$	the instantaneous velocity of single particle of class i
u^+	—	a dimensionless characteristic velocity
$u_{d,turb}^+$	—	a dimensionless turbulent deposition velocity
$u_{d,Th}^+$	—	a dimensionless thermophoretic deposition velocity
u^*	$m\,s^{-1}$	estimated value of the x-component of velocity
u_e	$m\,s^{-1}$	x-component of velocity calculated at the eastern face of the control volume
u'	$m\,s^{-1}$	correction of the x-component of velocity
u_τ	$m\,s^{-1}$	friction velocity
u_T	$m\,s^{-1}$	turbulent velocity parallel to the wall
v	$m\,s^{-1}$	y-component of velocity
v^*	$m\,s^{-1}$	estimated value of the y-component of velocity
v_n	$m\,s^{-1}$	y-component of velocity calculated at the northern face of the control volume
v'	$m\,s^{-1}$	correction of the y-component of velocity
V	m^3	volume
$V_{powdery}^*$	—	the volume fraction of powdery deposit (see section 3.5.1)
$V_{sintered}^*$	—	the volume fraction of sintered deposit (see section 3.5.1)
w	$m\,s^{-1}$	z-component of velocity
w_i	$kmol\,m^{-3}\,s^{-1}$	rate of reaction i, e.g. w_1, w_2, or w_{bon}

Symbol	Unit	Meaning
w_k^*	$kmol\,m^{-3}\,s^{-1}$	chemical reaction rate of the species k in the fine structure
w^*	$m\,s^{-1}$	estimated value of the z-component of velocity
w_t	$m\,s^{-1}$	z-component of velocity calculated at the top face of the control volume
w'	$m\,s^{-1}$	correction of the z-component of velocity
x_i	m	i^{th} space coordinate
y^+	—	dimensionless characteristic length which is used to describe the normal distance measured from the wall surface
Y_k	$kg_k\,kg_{mix}^{-1}$	mass fraction of species k in the solid-gas mixture
Y_k^*	$kg_k\,kg_{mix}^{-1}$	mass fraction of species k in the fine structure

Greek Symbols

Symbol	Unit	Meaning
α	—	absorptivity
χ	—	an exchange factor (section 3.5.2)
δ_{ij}	—	Kronecker delta
δ_ϕ	m	boundary layer thickness with respect to variable ϕ, i.e. δ_ψ, δ_v, or δ_T
Δt	s	time interval
η_p	—	impaction efficiency of the particle (section 3.3.2)
ε	—	emissivity
ε	$m^2\,s^{-3}$	dissipation rate of turbulent kinetic energy
γ	—	a multiplier used for pressure smoothing
γ^*	—	mass fraction occupied by the fine structures
Γ	—	generalized diffusion coefficient
κ	—	von Karman constant, $\kappa = 0.41$
λ	m	wavelength
μ	$kg\,m^{-1}s^{-1}$	dynamic viscosity
μ_{turb}	$kg\,m^{-1}s^{-1}$	turbulent viscosity
ν	$m^2\,s^{-1}$	kinematic viscosity
$\nu_{i,j}$	—	stoichiometric coefficient of species j in reaction i

Symbol	Unit	Meaning
Ω_D	—	a constant for KCl diffusion in N_2, $\Omega_D = 1.016$ (equation 3.16)
ϕ		a general variable used to represent any dependent variable in the transport equations, i.e. h, u_i, Y_k, k or ε
$\overline{\phi}$	*	Reynolds-averaged value of the variable ϕ
$\tilde{\phi}$	*	Favre-averaged value of the variable ϕ
ϕ	—	porosity (section 3.5)
ϕ'	*	fluctuation in the value of variable ϕ if ϕ is Reynolds-averaged
ϕ''	*	fluctuation in the value of variable ϕ if ϕ is Favre-averaged
ψ	—	a correction factor accounting for deviations from Stokes law (equation 3.45)
ψ_i	$kmol/kmol$	mole fraction of species i in the gas
$\Re$	$J\,kmol^{-1}\,K^{-1}$	universal gas constant, $\Re = 8314.472\ J\,kmol^{-1}\,K^{-1}$
σ	$W\,m^{-2}\,K^{-4}$	Stefan-Boltzmann's constant
σ_ϕ	—	Prandtl/Schmidt number of variable ϕ
τ_{ij}	$N\,m^{-2}$	shear stress in the ith space coordinate acting on the plane whose normal is in the jth space coordinate
τ_p	s	particle relaxation time (equation 2.64)
τ_f	s	time scale of the flow field (equation 3.46)
τ_w	$N\,m^{-2}$	wall shear stress
τ	s	residence time
τ^*	s	mean residence time of fluid in the fine structure
τ^+	—	dimensionless particle relaxation time
θ	*	angular position (section 3.3.2)
ϱ	$kg\,m^{-3}$	density
ϱ^*	$kg\,m^{-3}$	density of the fine structures
ϱ'	$kg\,m^{-3}$	Reynolds-averaged density fluctuation

Subscripts

Symbol	Meaning
b	backward
bon	bonding
$char$	characteristic
$cont$	continuous

Symbol	Meaning
C	char
daf	dry and ash free
dec	decomposition
dep	deposition
$discr$	discrete
D	diffusion
e	eastern boundary (face)
ex	external
eff	effective
f	forward
g	gas
kao	kaolinite
mix	mixture
max	maximum
n	northern boundary (face)
nb	neighbouring cells
$ndep$	undeposited
p	particle
P	values of the actual control volume
rad	radiation
$reac$	reaction
s	surface
t	tube
t	top boundary (face)
tot	total
$turb$	turbulent
Th	thermophoresis

Superscripts

Symbol	Meaning
0	initial value
0	surrounding fluid
$\oplus$	positive part with respect to the source term of variable ϕ
$\ominus$	negative part with respect to the source term of variable ϕ

Symbol	Meaning
$*$	fine structures
ch	chemical
D	diffusion
n_{ij}	reaction order of reaction i concerning species j
ph	physical

Abbreviations

Abbreviation	Meaning
AIOLOS	CFD combustion code used for carrying out combustion simulations
AAS	Atom Absorption Spectroscopy
BFC	Body Fitted Coordinates
BM1	Straw 1/Biomass 1 (see Table 4.4)
BM3	Straw 3/Biomass 3 (see Table 4.4)
CFD	Computational Fluid Dynamics
CHEMKIN	CHEMical KINetics package from Sandia National Labs
CVs	Control Volumes
CPU	Central Processing Unit of a computer
daf	Dry and Ash Free
DNS	Direct Numerical Simulation
EBU	Eddy Break Up
EDC	Eddy Dissipation Concept
EEG	Renewable energy ordinance
ELIF	Excimer Laser-Induced Fluorescence
EFCR	Entrained-Flow Combustion Reactor
IFK	Institute of Combustion and Power Plant Technology
FV	Finite Volume
HLRS	High Performance Computing Center
KSVA	The 0.5 MW semi-industrial pulverized-fuel combustion facility
PF	Pulverized Fuel
PSIC	Particle-Source In Cell method
PSR	Perfectly Stirred Reactor
QUICK	Quadratic Upwind Interpolation for Convective Kinematics

Abbreviation	Meaning
RANS	Reynolds Averaged Navier Stokes
RC	Raw Coal
RE	Resistance Equation
RSM	Reynolds Stress Model
SOR	Successive Overrelaxation
SK	A hard coal (see Table 4.4)
SL	Secondary air
SIMPLE	Semi Implicit Method for Pressure-Linked Equations
SIMPLEC	Semi Implicit Method for Pressure-Linked Equations Consistent
SIP	Strongly Implicit Procedure
WEO	World Energy Outlook

Kurzfassung

Die Nutzung von fossilen Brennstoffen zur Energieerzeugung führt zur Emission von Treibhausgasen. Dadurch entstehende Umweltschäden können reduziert werden, indem Kohle als Energieträger im Kraftwerk durch CO_2-neutrale Biomasse ersetzt wird. Der Wirkungsgrad der Energieumwandlung bei der thermischen Nutzung reiner Biomasse ist allerdings noch unzureichend im Vergleich zur Nutzung von Kohle. Eine weitere Alternative stellt die Mitverbrennung von Biomasse in bestehenden Kohlekraftwerken dar. Die Mitverbrennung von Biomasse führt jedoch tendenziell zu vermehrter Bildung von Ascheablagerungen auf den Oberflächen der Wärmeübertrager. Die Ascheablagerungen beeinträchtigen besonders im Bereich der Überhitzer-Heizflächen die Wärmeübertragung vom Rauchgas in den Wasser/Dampf-Kreislauf und schränken dadurch den Wirkungsgrad des Dampferzeugers ein. Um diese negativen Folgen vermindern zu können, ist ein grundlegendes Verständnis der Bildung der Ascheablagerungen erforderlich. Vor allem der hohe Anteil an flüchtigem Kalium, das während der Verbrennung der Biomasse freigesetzt wird, trägt zur Bildung von Ascheablagerungen bei. Das freigesetzte Kalium kann dabei vor oder während des Kondensationsprozesses mit Aschepartikeln reagieren. Dies führt zum Schmelzen von Aschepartikeln und damit letztlich zur Ablagerung an den Oberflächen der Wärmeübertrager. Das freigesetzte Kalium kann ebenfalls auf den gekühlten Rohroberflächen kondensieren und dort eine klebrige Schicht bilden, die die Bildung weiterer Ablagerungen noch beschleunigt.

In den letzten Jahren hat sich die Modellierung von Verbrennungsprozessen in Verbindung mit der numerischen Strömungsmechanik (Computational Fluid Dynamics) als sehr effizientes und zuverlässiges Hilfsmittel dargestellt. Daher wird dieses Tool vielfach angewendet um Strömungsfeld, Temperaturverteilung, Rauchgaszusammensetzung und Partikelbewegung in Brennkammern bei einer hohen örtlichen Auflösung vorherzusagen. Außerdem kann darin der Ascheablagerungsprozess durch die Integration von Depositionsmodellen umfassend untersucht werden. Diese Vorgehensweise ist besonders interessant, da die Durchführung entsprechender Simulationen sowohl eine Zeitersparnis als auch eine Kostenreduktion gegenüber rein experimentellen Untersuchungen ermöglicht.

Das Hauptziel der vorliegenden Arbeit besteht aus der Modellierung der Ablagerungsbildung in kohlegefeuerten Dampferzeugern bei Mitverbrennung von Biomasse. Als Schwerpunkt wurde insbesondere die Freisetzung von alkalischen Bestandteilen und deren Einfluss auf den Aufbau der Ablagerung untersucht. Die entsprechenden Modelle wurden in den 3D

Verbrennungssimulationscode AIOLOS integriert. Die Modelle zur Ablagerungsbildung wurden als Post-Processing-Schritt implementiert. Im ersten Schritt wird dabei eine Basissimulation durchgeführt, die sowohl die Freisetzung der Kaliumverbindungen als auch das Strömungsfeld sowie die Temperatur- und Konzentrationsverteilung beschreibt. Daraufhin wird der Verlauf einer großen Anzahl an Partikeln in der Brennkammer verfolgt bis diese entweder die Wandflächen berühren und haften bleiben oder die Brennkammer mit dem Rauchgas verlassen. Die Daten die in der Basissimulation generiert wurden – wie Konzentration der Feststoffe bzw. Eigenschaften der Gasphase – werden nun als Eingangsdaten für das eigentliche Modell des Ablagerungsmechanismus verwendet.

Sowohl heterogene als auch homogene Reaktionen werden zur Beschreibung der Alkalifreisetzung berücksichtigt. Die heterogenen Reaktionen sind unterteilt in einen ersten Schritt der Alkalifreisetzung und eine darauffolgende Reaktion zwischen den freigesetzten Alkalispezies und den Aluminiumsilikaten der Flugasche. Ein globales Modell von Tomeczek wird zur Beschreibung der Sulfatisierung der freigesetzten Alkalispezies verwendet. Die Validierung der eingesetzten Modelle wurde anhand von Simulationen eines Flugstromreaktors im kleinen Maßstab durchgeführt. Das Modell zur Natriumfreisetzung wurde mit Hilfe von Simulationen mit einer deutschen Steinkohle als Brennstoff evaluiert. Die Simulationsergebnisse stimmen gut mit den Messungen überein – insbesondere bei einer Verweilzeit von weniger als 10 s. Zur Validierung des vorgeschlagenen Modells zur Kaliumfreisetzung wurden Simulationen mit Braunkohle mit niedrigem Aluminiumsilikat-Gehalt und mit Steinkohle als Brennstoff bei kurzer Verweilzeit durchgeführt. Die berechnete Kaliumfreisetzung zeigt eine gute Übereinstimmung mit den experimentellen Daten. Allerdings zeigt sich dabei auch, dass eine Reaktionsrate, die bei einem bestimmten Kohletyp gut passt, nicht auf andere Kohletypen übertragbar ist. Unterschiedliche Aschezusammensetzungen können das Verhalten der Aschebestandteile bzgl. der Kontrolle der Alkalifreisetzung beeinträchtigen.

Was die Bildung der Ablagerungen angeht, so wird sowohl der Einfluss der Alkalispezies auf die Haftwahrscheinlichkeit der Aschepartikel als auch der Beitrag der freigesetzten Alkalispezies zu der Ablagerungsschicht modelliert. Dabei werden zwei wesentliche Ablagerungsmechanismen berücksichtigt. Dies sind das inerte Auftreffen der Kohlenstaubpartikel sowie die Kondensation der freigesetzten Alkaliverbindungen. Damit wurden Simulationen von Biomasse-Mitverbrennung in kohlegefeuerten Dampferzeugern durchgeführt. Die Simulationsergebnisse werden mit Fokus auf die Eigenschaften der eingesetzten Biomasse und den Anteil der Biomasse an der Gesamtleistung diskutiert und mit experimentellen Daten verglichen.

In Bezug auf die Basissimulation zeigt sich, dass das berechnete Temperaturprofil gut mit den Messwerten übereinstimmt. Gewisse Abweichungen sind auf die Unsicherheiten bei der Bestimmung der Drallzahl der Sekundärluft zurückzuführen. Es wurden zwei Kondensationsmodelle eingesetzt und hinsichtlich ihrer Anwendbarkeit zur Vorhersage des Ablagerungsprozesses in kohlegefeuerten Dampferzeugern bei Biomasse-Mitverbrennung

bewertet. Im Allgemeinen ist die Kondensationsrate, die mit einem Modell auf Basis der Filmtheorie berechnet wurde, um fünf Größenordnungen niedriger als die Kondensationsrate, die mit dem Modell nach Goldbrunner berechnet wurde. Mit Goldbrunners Modell besteht die Ablagerung überwiegend aus kondensierbaren Spezies. Dies stimmt allerdings nicht mit den betrachteten realen Testfällen überein. Deshalb wurde das auf der Filmtheorie beruhende Modell verwendet, um die Kondensation von K_2SO_4 zu beschreiben. Darüberhinaus konnte gezeigt werden, dass das Filmtheorie-Modell die Kondensationrate an den Überhitzer-Heizflächen in Dampferzeugern vorhersagen kann. Dennoch wurden Abweichungen zwischen Experiment und Simulation beobachtet. Diese könnten auf den Einfluß der Bildung von Aerosolen zurückzuführen sein, was jedoch in dieser Arbeit nicht berücksichtigt wurde.

Abstract

Due to its CO_2-neutrality, the utilization of biomass as energy resource has become a solution to reduce the environmental damage caused by the greenhouse gas emissions. Biomass may replace coal partially or entirely in power generation plants. However, biomass as a single fuel is still unable to satisfactorily replace coal with respect to energy conversion efficiency. As an option co-firing biomass with coals may be implemented in existing large-scale firing systems. However, co-firing biomass with coals leads to a higher tendency of deposit formation on the heat transfer surfaces. The deposit formation (especially in the superheater section of utility boilers) is a major problem due to a reduction in heat transfer rates from the flue gas to the steam circuit. Therefore, a better understanding of the phenomena is required to solve the problem. The formation of deposit is mainly due to the high amount of volatile potassium in biomass, which is vaporized during combustion. The vaporized potassium may react with ash particles prior to or after the condensation process. This may lead to partly melting of the ash particles which promotes the deposition process on the heat transfer surfaces. Alternatively, the vaporized potassium may condense on cooled tube surfaces, afterwards creating sticky surfaces that accelerate deposit build-up.

In the recent years, numerical modelling of combustion processes in conjunction with Computational Fluid Dynamics (CFD) has become a very efficient tool and is hence widely applied in predicting flow field, temperature, flue gas composition, and particle aerodynamics inside furnaces achieving a high local resolution and reliability. Furthermore, a comprehensive investigation of the deposition process can be performed by incorporating deposition models into the CFD codes. This approach is especially attractive because it may produce a reliable prediction with reduction in cost and time compared to a purely experimental approach.

The main objective of the present work is the modelling of deposit formation for coal-fired boilers with biomass co-combustion. In particular, the focus has been on the release of alkali and its effect on the deposit build-up. The models were integrated into the 3D combustion simulation code AIOLOS. The deposit formation models were implemented in a post-processing step. First, a basic simulation run involving the release of potassium species has to be performed, supplying flow, temperature, and the species concentration fields. Then, large numbers of particles are tracked through the furnace until they touch and eventually stick to the surface, or they simply leave the furnace through an outlet. Data calculated in the preceding basic

simulation, e.g., concentrations of solids and gas phase properties are used as input data for actual deposition mechanism models.

Concerning the alkali release, the heterogeneous reactions as well as the homogeneous reactions are considered in the present work. The heterogeneous reactions are divided into the primary step of alkali release and the secondary reaction between the released alkali and the aluminosilicate in the fly ash. A global model proposed by Tomeczek is used to describe the sulfation of the released alkali. Evaluation of the model has been performed by running the simulations on a small-scale entrained flow reactor. The model for sodium release was evaluated by running simulations for the combustion of a German bituminous coal. The simulation results correspond well with the measurements especially at a residence time below $10\ s$. In order to evaluate the proposed model of potassium release, simulation runs were performed for the combustion of a lignite coal with a low content of aluminosilicate and a hard coal at a low residence time. The calculated potassium release from those cases was found to be in good agreement with the measured values. However, it seems that the reaction rate which is appropriate for a specific type of coal may not be applicable for another type of coal. A difference in ash composition may affect the behaviour of ash elements in controlling the alkali release.

In terms of deposit formation, the effect of alkali on the sticking probability of the arriving ash particles and the contribution of the released alkali to the deposit layer are modelled. Two major deposition mechanisms are taken into account in the model, i.e. inertial impaction for the pulverized fuel particle and condensation for the released alkali. Simulations of deposit formation for coal-fired boilers with biomass co-combustion have been performed. Various simulation results with respect to the co-fired biomass type and the biomass thermal share were discussed and evaluated against the experimental data.

In terms of the basic simulation, the temperature profile along the axis is found to be in agreement with the experimental data. The major discrepancy is most remarkable at the peak temperature due to a difficulty to determine the swirling factor of the injected secondary air. Two condensation models have been compared and discussed in terms of their applicability to the prediction of fouling phenomena in coal-fired utility boilers with biomass co-combustion. In general, the condensation rate calculated by a model based on the film theory is five orders of magnitude lower than that calculated by Goldbrunner's model. By using Goldbrunner's model, the deposit composition is dominated by the condensible species which is far from reality based on the investigated cases. Hence, the film theory model was utilized to describe the condensation of K_2SO_4 on the deposition probe. Furthermore, it was shown that the film theory model is able to predict the condensation rate in the superheater section of utility boilers. However, some deviations between experiment and predictions have been found. This is attributed to the presumably significant effect of aerosol formation which is not considered in the current work.

1 Introduction

1.1 Motivation

Currently, the world's energy demands are still expected to increase due to economical growth. Special attention has to be paid to this situation due to increasing energy prices in the future and the requirement for sustainable energy supplies. In addition, global warming related to CO_2 emissions is also an important issue in the development of new energy solutions. Coal together with other fossil fuels such as gas and oil are currently, and will remain for sometime, the main source to meet increasing worldwide energy demands. However, a major disadvantage of using fossil fuels as an energy resource is the emissions of species such as NO_x, SO_2, CO_2, etc. The combustion of fossil fuels inevitably produces large amounts of carbon dioxide. Based on the 2006 WEO Reference Scenario, energy-related CO_2 emissions will rise by 98% above 1990 levels by 2030 [53]. On the other hand, emission regulations are getting more stringent. The problem can be solved by an efficient use of the fossil fuels for energy generation that will lead to the reduction of emissions from global warming gases and a higher efficiency of power generation.

As an alternative, biomass may replace coal partly or entirely in power generation plants. Biomass is gaining increasing interest as a renewable energy resource for two main reasons: 1) biomass is an attractive fuel due to its CO_2-neutrality, which may lead to reduced environmental damage, 2) utilization of biomass may save valuable energy resources. Also, another reason is that there is a great surplus of agriculture production due to a process-intensive plantation technique in some European countries. For example, in Denmark there is a fairly large surplus of straw, and it has been used for power generation in utility boilers as well as for heat production in small scale furnaces, e.g. at individual farms. On the other hand, Germany is one of the countries which makes great efforts to encourage biomass utilization: a new renewable energy ordinance (EEG) is sanctioned which obliges electricity distributors to buy electricity from renewable energy sources at an increased reimbursement. Even demolition wood is regarded as biomass in this ordinance. This ordinance shall make firing biomass profitable, so that the large potential of available biomass can actually be explored [29].

Though the use of biomass for power generation has been practiced for a number of years, there is far too little biomass to replace coal globally. In terms of energy conversion efficiency,

biomass as a single fuel is still unable to satisfactorily replace coal as an energy resource. As an option co-firing biomass with coals may be implemented in existing large-scale firing systems. Some power plants in Denmark, Holland and Austria utilize biomass co-combustion with coal for electricity production. In existing pulverized coal fired boilers, this technology offers several environmental benefits such as reducing SO_2 and CO_2 emissions. In addition, co-combustion of biomass such as wood, straw, and energy crops with coal in full scale boilers for power generation is a means of high energy-efficient utilization at comparatively low investment costs.
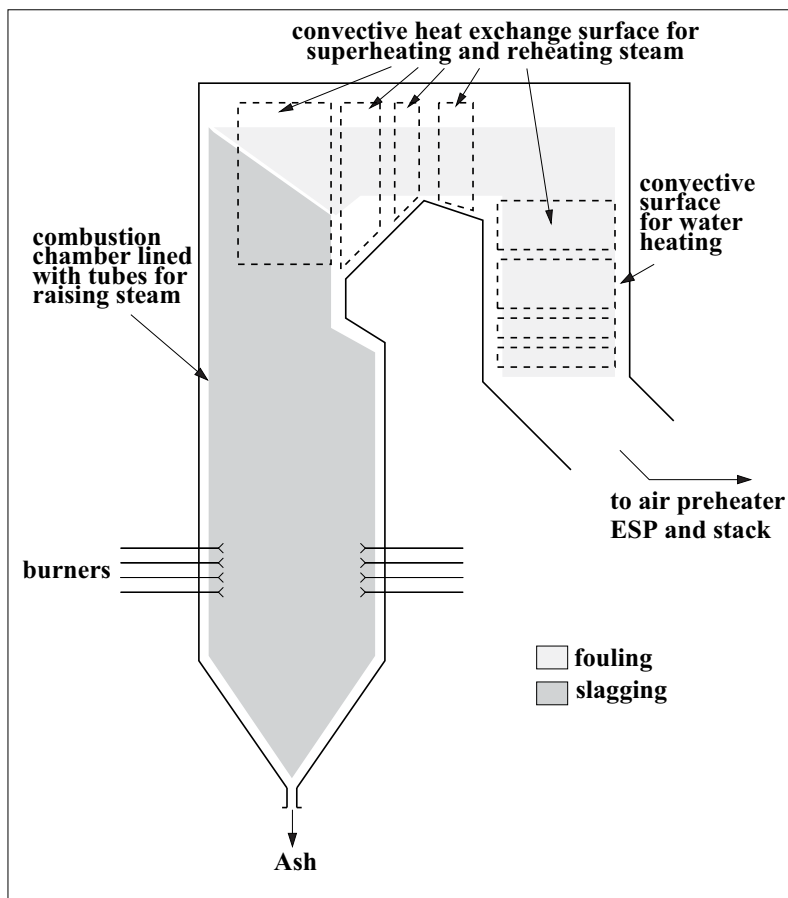
Figure 1.1: Schematic illustration of slagging and fouling regions in typical pulverized fuel boilers [16].

However, co-firing biomass with coals will lead to a higher tendency of deposit formation on the heat transfer surfaces. Uncontrolled deposits causes some operational problems including corrosion as well as slagging and fouling. Fig. 1.1 shows schematically conventional pulverized fuel (pf) fired boiler configuration with regions of slagging and fouling. It can be seen from the figure that slagging represents the deposit formation within the furnace where the heat transfer process is dominated by radiation, whereas fouling refers to the deposit formation in the convective passes of the boiler. These problems cause a reduction in heat transfer rates

from the flue gas to the steam circuit causing a decrease in plant efficiency. Unscheduled plant shutdowns are necessary due to unmanageable forms of detrimental deposits causing a deterioration in plant availability. The operational problems are mainly due to the high amount of volatile potassium in biomass, which is vaporized during combustion. The vaporized potassium may react with ash particles prior to or after the condensation process. This may lead to partly melting of the ash particles which promotes the deposition process on the heat transfer surfaces. Alternatively, the vaporized potassium may condense on cooled tube surfaces, afterwards creating sticky surfaces that accelerate deposit build-up. A typical view of deposit formation on superheaters in a coal-fired furnace is shown in Fig. 1.2. The shape of deposits may be similar to that found in a co-firing system. An illustration of a deposit shape with biomass co-combustion in a 0.5 MW semi-industrial pulverized-fuel combustion facility can be found in [29]. In order to prevent or at least to reduce such problems, there have been
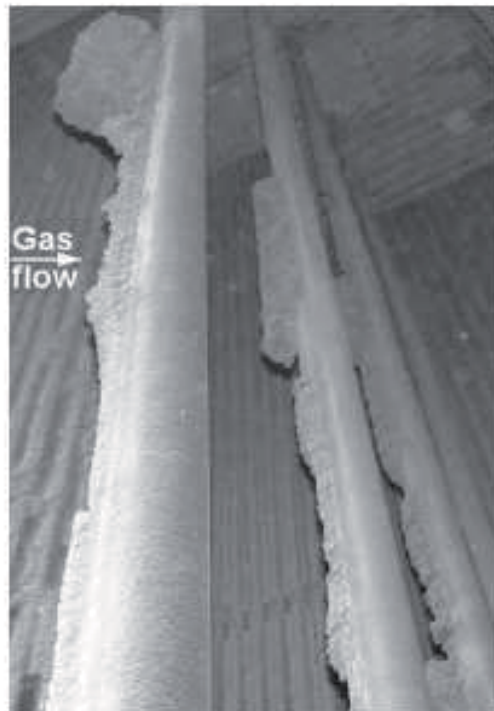

Figure 1.2: View of deposit on superheaters [111].

continuous efforts in both industrial and academic areas in order to predict slagging and fouling tendency. For that purpose, there have been several methods ranging from the most simple indices, based on traditional coal analysis, to advanced models dealing with the fundamental deposition mechanisms [56, 84]. The first methods are the empirical approaches and only valid in a very narrow band of coal rank and they cannot, with any confidence, be utilized for co-firing biomass with coals. The latter ones which consider the physical and chemical processes taking place are much more suitable for general applications.

To predict heat transfer degradation from the flue gas to the steam circuit, it is required to consider the most important processes concerning the mineral transformation and subsequent ash deposition as well as heat transfer through the deposit. For this purpose, the mechanistic approaches of deposit formation in coal fired boilers have been developed [82]. Even though the mechanisms were developed for coal, they are also applicable for biomass fired boilers [6]. Also, the mechanistic descriptions can be applied to a co-firing system, which is different in the relative importance of the mechanisms.

In the recent years, numerical modelling of combustion processes in conjunction with Computational Fluid Dynamics (CFD) has become a very efficient tool and is hence widely applied in predicting flow field, temperature, flue gas composition, and particle aerodynamics inside furnaces achieving a high local resolution and reliability. Furthermore, a comprehensive investigation of the deposition process can be performed by incorporating deposition models into the CFD codes. This approach is especially attractive because it may produce a reliable prediction with reduction in cost and time compared to a purely experimental approach. Based on this situation, the 3D-combustion simulation code AIOLOS has been developed at the Institute of Combustion and Power Plant Technology (IFK) at University of Stuttgart since the late 1970s, which mainly deals with pulverized-fuel combustion processes. More detailed information about the simulation code is available in [60, 98].

1.2 Objectives and Arrangement of the Current Work

Biomass contains a relatively high amount of potassium which significantly affects the deposition process in case of the co-firing technology. In order to predict such effects, this work focuses on two important processes, one is the release of alkali during combustion, and the other is the effect of the released alkali on the deposit build-up. A relatively detailed model is proposed in this work in terms of the alkali release. To the best of the author's knowledge this may be the first time that the detailed model is involved in the prediction of deposit build-up in case of the co-firing system. Models for these processes are developed and integrated into AIOLOS. In these models, the released alkali contributes to the formation of deposit layer via condensation process, and the condensible alkali has effect on the sticking probability of ash particles on the deposit surface. The deposition mechanisms for ash particles depending on the particle sizes and geometry as well as a heat transfer model are utilized in order to build a comprehensive deposition model in the furnaces [90]. For validation purposes, two experimental results are used in this work. One is the experiments which were performed on an atmospheric-pressure drop tube reactor by Reichelt [85], and the other is the experiments which were performed on the 0.5 MW semi-industrial pulverized-fuel combustion facility by Heinzel [42].

Chapter 2 deals with the general aspect of CFD simulation of reacting flow, and the relevant features of solid combustion modelling compared to the deposition models are briefly summarized. A fully coupled Eulerian/Lagrangian approach as an alternative to Eulerian framework in order to model the behaviour of a two-phase flow involving flue gas and particles is described.

In Chapter 3 alkali metals behaviour in coal as well as in biomass are presented and discussed. The heterogeneous and homogeneous reactions for the alkali species are described. Transport and deposition mechanisms of the released alkali and that of ash particles are addressed. A brief discussion about sticking probability especially with the inclusion of the effect of the condensible species as well as the models of heat transfer through the deposit is presented. Strategies for implementation of the models into the 3D-combustion simulation code AIOLOS are discussed.

Evaluations of all models are presented in chapter 4. Simulation results concerning the alkali release and subsequent deposition process are presented and discussed by comparing them with the experimental ones. The results regarding the deposition process are presented, both for a case with 100% biomass and for several co-firing cases with low thermal shares of biomass.

Chapter 5 presents conclusions of the work and recommendations for future work.

2 CFD Simulation of Turbulent Reactive Flows

2.1 Basic Equations

In this section, the basic equations and the theoretical basis of the reactive flow simulation for solid fuel combustion process are described briefly. Therefore, the behaviour of a two-phase flow consisting of flue gas and particles has to be described. The flow and temperature fields as well as the concentration distributions obtained from the simulation will provide the input data for the deposition model in the next chapter. The basic equations consist of the conservation of mass, momentum, species concentration and enthalpy which can be expressed in Cartesian tensor form as follows [53]:

Conservation of Mass:

$$\frac{\partial \varrho}{\partial t} + \frac{\partial \varrho u_j}{\partial x_j} = 0, \tag{2.1}$$

where ϱ, u_j and x_j are the mixture density, the velocity in j direction and the space coordinate in j direction. The subscript j can take the values $1, 2, 3$.

Conservation of Momentum:

$$\frac{\partial \varrho u_i}{\partial t} + \frac{\partial \varrho u_j u_i}{\partial x_j} = -\frac{\partial p}{\partial x_i} + \frac{\partial \tau_{ij}}{\partial x_j} + \varrho g_i \tag{2.2}$$

in this equation p denotes the pressure, g_i denotes the gravitational acceleration in the i direction, and τ_{ij} denotes the shear stress in the i direction on a surface normal to the j direction. With an assumption that the fluid is Newtonian, the shear stress can be expressed as:

$$\tau_{ij} = \mu \left(\frac{\partial u_i}{\partial x_j} + \frac{\partial u_j}{\partial x_i} - \frac{2}{3} \frac{\partial u_k}{\partial x_k} \delta_{ij} \right), \tag{2.3}$$

where μ is the molecular viscosity of the fluid. The bulk viscosity is neglected in the equation because it plays an insignificant role in many flows of practical interest.

Conservation of Mass Fractions of Species: In a multi-component system, the transport equations of species are expressed in terms of the mass fractions of the species. Furthermore, the mass fractions of the species k, Y_k, are expressed in the following equation:

$$\frac{\partial \varrho Y_k}{\partial t} + \frac{\partial \varrho u_j Y_k}{\partial x_j} = -\frac{\partial J_{kj}}{\partial x_j} + S_{Y_k}, \tag{2.4}$$

where J_{kj} represents the mass molecular flux of species k in the j direction and S_{Y_k} represents a source term or a sink term due to formation or consumption of species k by chemical reactions. The mass fraction of the last species can be obtained by the mass constraint:

$$\sum_{k=1}^{N} Y_k = 1. \tag{2.5}$$

The molecular transport processes in multi-component mixtures are quite complex. However, the main properties in terms of turbulent reactive flows modelling are mostly associated with the large turbulent scales, and molecular transport is of secondary importance. Due to this consideration, the expression of mass molecular flux can be simplified based on Fick's law [53]:

$$J_{kj} = -\varrho D_k \frac{\partial Y_k}{\partial x_j}, \tag{2.6}$$

where D_k is the binary diffusion coefficient, or mass diffusivity, of species k with respect to an abundant species, for instance N_2.

By inserting Equation 2.6 into Equation 2.4, the transport equation of species k can be written as:

$$\frac{\partial \varrho Y_k}{\partial t} + \frac{\partial \varrho u_j Y_k}{\partial x_j} = -\frac{\partial}{\partial x_j}\left(\frac{\mu}{Sc_k}\frac{\partial Y_k}{\partial x_j}\right) + S_{Y_k}, \tag{2.7}$$

where Sc_k is the Schmidt number of the species k, defined as:

$$Sc_k = \frac{\mu}{\varrho D_k}. \tag{2.8}$$

Conservation of Energy: The conservation of energy can be expressed by several formulations. For a low-velocity flow with negligible viscous dissipation, the first law of thermodynamics can be written as:

$$\frac{\partial \varrho h}{\partial t} + \frac{\partial \varrho u_j h}{\partial x_j} = \frac{\partial}{\partial x_j}\left(\frac{\mu}{Pr}\frac{\partial h}{\partial x_j}\right) + S_h \tag{2.9}$$

where h is the specific enthalpy representing the internal energy of the fluid, Pr is the Prandtl number, and S_h is the heat source term. The two terms on the left hand side of the equation are associated with the temporal change of energy and the heat transfer by convection, respectively.

The first term on the right hand side represents the conductive heat transfer. Furthermore, the heat in the source term is generated by the energy release during homogeneous reactions, $S_{h,reac}$, the radiative heat transfer, $S_{h,rad}$, and the heat transferred by convection and mass transfer between the two phases, $S_{h,p}$:

$$S_h = S_{h,reac} + S_{h,rad} + S_{h,p}. \tag{2.10}$$

Some thermodynamic properties are required in order to solve the conservation equations described previously. In the present work, the gases are assumed to be ideal, then the mixture density, ϱ, the temperature, T, and the pressure, p, are related by the following expression:

$$\varrho = \frac{p \cdot M_{M_{mix}}}{\Re \cdot T}, \tag{2.11}$$

where $\Re$ is the universal gas constant and has the value $8314.372 \ J \, kmol^{-1} \, K^{-1}$. The average molecular mass of the mixture, $M_{M_{mix}}$, can be expressed in terms of the mass fractions of species, Y_k, the species molecular weight, M_{M_k}, and the number of species, N:

$$\frac{1}{M_{M_{mix}}} = \sum_{k=1}^{N} \frac{Y_k}{M_{M_k}}. \tag{2.12}$$

In this work, density variations due to pressure fluctuations are neglected. Hence, the actual pressure is set equal to a reference pressure, $p = p_0$. Based on this assumption, Equation 2.11 can be rewritten as:

$$\varrho = \frac{p_0 \cdot M_{M_{mix}}}{\Re \cdot T}, \tag{2.13}$$

where the temperature, T, is written as the function of the specific enthalpy, h, and the specific heat capacity at constant pressure, c_p [96]:

$$T = \frac{h - c_{p0} \, T_0}{c_p}, \tag{2.14}$$

where c_{p0} represents the specific heat enthalpy at the reference temperature, T_0.

Since chemical reactions occur during combustion processes, conservation equations for each participating component in the reactions have to be considered. The calculation of chemical reactions is connected to the chemical source term. Generally, a chemical reaction i can be expressed in terms of stoichiometric relations as follows:

$$\sum_{j=1}^{J} \nu_{i,j} \cdot A_j = 0 \qquad j = 1, 2, ..., J \tag{2.15}$$

where $\nu_{i,j}$ and A_j represent the stoichiometric reaction i of species j, and the name of species j, respectively. The reaction rate, w_i, quantifies the speed of the reaction and can be related to the temperature and the molar concentrations by:

$$w_i = \frac{1}{\nu_{i,j}} \left(\frac{dc_j}{dt} \right)_i = k_i \cdot \prod_{j=1}^{J} c_j^{n_{ij}} \tag{2.16}$$

where k_i is the rate coefficient of reaction i, and $n_{i,j}$ is the reaction order of reaction i concerning species j. For elementary reactions, the reaction order n and the activation energy E can usually be determined theoretically [120]. For global reactions, they must be derived by fitting experimental data. In order to gain more clarity, an example with regard to the attack of hydrogen atoms on oxygen molecules to form OH radicals and oxygen atoms is given as follows:

$$H + O_2 \rightleftharpoons OH + O. \tag{2.17}$$

As a result of the forward reaction path, concentrations of species H and O_2 will decrease and the concentrations of OH and O will increase in time. The number of reacting molecules depends on the concentrations of species H and O_2. The forward reaction rate, w_f, is defined by:

$$w_f = k_f \, c_H \, c_{O_2}, \tag{2.18}$$

where c_j denotes concentration of a species in moles per unit volume, and k_f the elementary reaction rate coefficient. The index f indicates that the forward reaction is considered. For a homogeneous system, the concentrations of the species considered here change in time due to this reaction according to:

$$w_f = \frac{dc_{OH}}{dt} = \frac{dc_O}{dt} = -\frac{dc_H}{dt} = -\frac{dc_{O_2}}{dt}. \tag{2.19}$$

The elementary reaction rate coefficient is usually written in a so-called Arrhenius form:

$$k_f = k_{0,f} \, T^b \, exp \left(-\frac{E_f}{\Re T} \right), \tag{2.20}$$

where $k_{0,f}$ and b are the reaction constants, and E_f is the activation energy. The reaction rate of the backward reaction is given by w_b, and the net reaction rate of reaction (2.17) is given by w_i:

$$w_i = w_f - w_b = k_f \, c_H \, c_{O_2} - k_b \, c_{OH} \, c_O. \tag{2.21}$$

If the reaction is in chemical equilibrium the reaction rate, w_i, is zero, so that:

$$\frac{c_{OH} \, c_O}{c_H \, c_{O_2}} = \frac{k_f}{k_b} = K_i, \tag{2.22}$$

where K_i is the equilibrium constant of the reaction. The equilibrium constant can be derived from the thermodynamic properties of the species OH, O, O_2, and H. To calculate the equilibrium constant, the CHEMKIN package [52] can be used.

2.2 The General Transport Equation

The conservation equations of mass, velocity, mass fractions of species and enthalpy have a general form which can expressed by the following equation:

$$\frac{\partial (\varrho\phi)}{\partial t} + \frac{\partial (\varrho u_j \phi)}{\partial x_j} = \frac{\partial}{\partial x_j}\left(\Gamma\frac{\partial\phi}{\partial x_j}\right) + S_\phi, \tag{2.23}$$

where ϕ denotes the dependent variables and Γ is the diffusion coefficient. The equation balances the temporal change, the convective and diffusive transport and the sources and sinks of a generalized variable ϕ. In the current work, all simulations are performed at steady state conditions, so the first term on the left hand side is neglected when the numerical schemes applied for the solution of the general equation are discussed in the following section.

2.3 Numerical Method

The general transport equation (2.23) is a non-linear partial differential equation. It is impossible to solve the differential equation analytically. Hence, a numerical method will be used for that purpose. With the numerical approach, the differential equations are replaced by a set of algebraic equations which can be solved with relative ease.

The numerical method of choice for the solution of the transport equations is the Finite Volume (FV) method. Using this method, the calculation domain has to be subdivided into a number of cells which are commonly called control volumes (CVs). For stationary cases, the governing transport equation can be transformed into a system equation as follows:

$$A_P \cdot \phi_P = \sum_{nb} (A_{nb} \cdot \phi_{nb}) + S_\phi \cdot V \qquad where \qquad A_P = \sum_{nb} A_{nb}. \tag{2.24}$$

where P denotes values of the actual control volume which has six neighbouring cells ($nb = 1, 2, ..., 6$). A structured non-staggered grid system is applied in the present work. The coefficients A_{nb} are determined from the convective and diffusive parts. The source term $S_\phi \cdot V$ incorporates real sources/sinks and additional terms caused by higher discretization schemes. There are a number of discretization schemes to determine the values on the cell faces. The value associated with the diffusion term is interpolated by central differencing scheme [79], whereas one of several available discretization schemes, e.g. central differencing, upwind [79], monotonized linear upwind [74], QUICK [61] can be applied for the convective term.

For a stable iterative solution of equation (2.24), the procedure usually requires relaxation. Furthermore, considering that the source term S_ϕ is frequently a function of the variable ϕ, it is linearised in the following way for numerical stability:

$$S_\phi = S_\phi^\oplus + S_\phi^\ominus \cdot \phi_P, \tag{2.25}$$

where $S_\phi^\oplus$ and $S_\phi^\ominus$ are the positive part and the negative part of the source term, respectively. The balance equation for the cell P obtains then the following form:

$$\left(A_P - S_\phi^\ominus \cdot V\right) \phi_P = \sum_{nb} \left(A_{nb} \cdot \phi_{nb}\right) + S_\phi^\oplus \cdot V. \tag{2.26}$$

The linear equation system is solved by iterative approaches like Successive Overrelaxation (SOR) and Strongly Implicit Procedure (SIP) [106]. Different discretization schemes and solution procedures have been summarised and compared by Schneider [96].

2.4 Pressure Correction Equations

For solving the general transport equation for ϕ, a flow field is required as the convective coefficients are the function of the velocity components. The flow field is specified by solving the momentum equations (see equation 2.2). However, the calculation of the velocity field is not an easy task due to the unknown pressure field. For compressible flows, the continuity equation can be used directly as a transport equation to obtain a density field, then the pressure is accordingly calculated from the equation of state. This approach is not applicable if low speed flows where Mach numbers approach the zero limit are considered. In this case, the density is dependent on pressure, and to handle this situation, it is needed to change the orientation of view in which the velocity field is affected by the pressure field, not by density. Thus, in order to satisfy continuity, the conservation of mass is written in terms of pressure correction terms. The pressure correction terms are solved indirectly and are used to correct the pressure gradients present in the momentum equations.

To deal with such pressure correction terms, a method has been developed by Patankar [79] known as Semi-Implicit Method for Pressure Linked Equations (SIMPLE). This method is reviewed briefly in this work for both staggered grid and non staggered grid arrangements. As an alternative, another method known as SIMPLE-Consistent (SIMPLEC) can be used for that purpose. The implementation of the SIMPLEC method on non-staggered grids is discussed in the work of Anany [4].

2.4.1 SIMPLE Method on Staggered Grid

The staggered grid arrangements were proposed by Harlow and Welsh [40] to prevent the pressure-velocity decoupling causing zig-zag on non-staggered grid arrangements, which is also called 'checker-board' pressure distributions as discussed by Patankar [79]. In the staggered grid arrangements, all variables, except velocity components, are stored at the control volume centres, whereas the velocity components are calculated at the cell faces. Based on the SIMPLE Method, the pressure-correction equation is written as follows:

$$\frac{\partial}{\partial x}\left(\frac{\rho V}{A_e^u}\frac{\partial p'}{\partial x}\right) + \frac{\partial}{\partial y}\left(\frac{\rho V}{A_n^v}\frac{\partial p'}{\partial y}\right) + \frac{\partial}{\partial z}\left(\frac{\rho V}{A_t^w}\frac{\partial p'}{\partial z}\right) \\ = \frac{\partial \rho u_e^*}{\partial x} + \frac{\partial \rho v_n^*}{\partial y} + \frac{\partial \rho w_t^*}{\partial z} \tag{2.27}$$

After solving equation 2.27, the velocity corrections can be obtained by using the following velocity-pressure correction relationships:

$$u_e' = -\frac{V}{A_e^u}\frac{\partial p'}{\partial x} \quad ; \quad v_n' = -\frac{V}{A_n^v}\frac{\partial p'}{\partial y} \quad ; \quad w_t' = -\frac{V}{A_t^w}\frac{\partial p'}{\partial z} \tag{2.28}$$

Then, the correct pressure p is given by:

$$p = p^* + p' \tag{2.29}$$

where p' is the mass-conserving pressure correction, and the improvement of the pressure estimation leads to better results of the velocity components. The correct velocity components can be written also in terms of the velocity corrections as follows:

$$u = u^* + u' \quad v = v^* + v' \quad w = w^* + w' \tag{2.30}$$

2.4.2 SIMPLE Method on Non-Staggered Grids

Various methods have been proposed in order to maintain the use of SIMPLE algorithms on non-staggered grids. These are, e.g., Rhie and Chow method [88], Wijngaart method [125], Majumdar Method [68], and Aksoy and Chen method [3]. The approach discussed here is the one proposed by Date [18] which is based on the smoothing pressure correction in order to solve the checker-board pressure distributions.
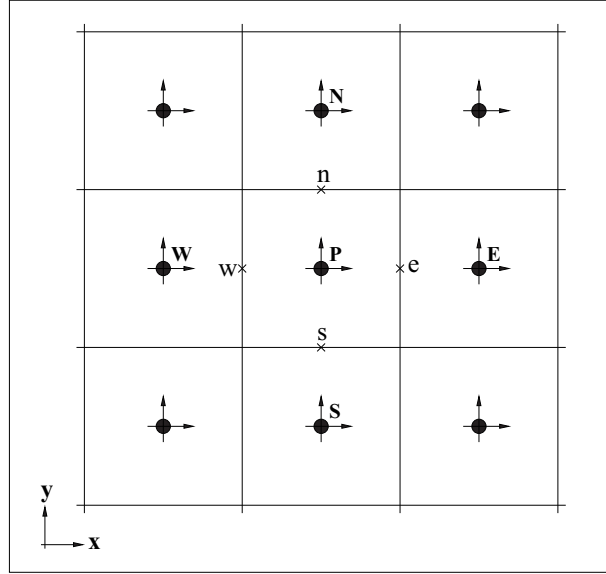
Figure 2.1: The non-staggered grid arrangement where all variables are calculated at the cell-centres.

The pressure-correction equation proposed by Date [18] is as follows:

$$
\begin{aligned}
\frac{\partial}{\partial x}\left(\frac{\rho V}{A_P^u}\frac{\partial p'}{\partial x}\right) + \frac{\partial}{\partial y}&\left(\frac{\rho V}{A_P^v}\frac{\partial p'}{\partial y}\right) + \frac{\partial}{\partial z}\left(\frac{\rho V}{A_P^w}\frac{\partial p'}{\partial z}\right) \\
&= \frac{\partial \rho u^*}{\partial x} - \frac{\partial}{\partial x}\left(\frac{\rho V}{A_P^u}\frac{\partial p'_{sm}}{\partial x}\right) + \frac{\partial \rho v^*}{\partial y} - \frac{\partial}{\partial y}\left(\frac{\rho V}{A_P^v}\frac{\partial p'_{sm}}{\partial y}\right) \\
&\qquad + \frac{\partial \rho w^*}{\partial z} - \frac{\partial}{\partial z}\left(\frac{\rho V}{A_P^w}\frac{\partial p'_{sm}}{\partial z}\right)
\end{aligned}
\tag{2.31}
$$

where p' and p'_{sm} denote the pressure correction and the smoothing pressure corrections, respectively. The smoothing pressure correction is defined as:

$$
p'_{sm} = \gamma \left[p^* - \bar{p}^*\right]
\tag{2.32}
$$

where $\bar{p}^*$ is a multidimensional averaged pressure in respect to the estimated pressure p^*. More details about the averaged pressure can be found in [4]. After calculating the pressure correction using equation 2.31, the component velocity corrections can be computed based on the following equations:

$$
u'_P = -\frac{V}{A_P^u}\frac{\partial p'}{\partial x} \quad ; \quad v'_P = -\frac{V}{A_P^v}\frac{\partial p'}{\partial y} \quad ; \quad w'_P = -\frac{V}{A_P^w}\frac{\partial p'}{\partial z}
\tag{2.33}
$$

Then, the pressure and velocity fields are corrected based on equation 2.29 and 2.30.

2.5 Turbulence Model

Combustion processes often take place within a turbulent rather than in a laminar flow field. A difficulty arises from balancing the instantaneous value of the variable ϕ. At a given location in the flame, ϕ does not behave deterministically, but rather stochastically. Since the smallest length scales in turbulent fluids are in the order of magnitude of some millimetres, a very fine resolution of the numerical grid would be required, leading to a huge number of grid points. Such a procedure called "Direct Numerical Simulation" (DNS) leads to prohibitively an extremely dense grid and excessive computer CPU time. Therefore, the implementation of this method to resolve a turbulent flow field of an industrial utility boiler is not feasible, at least considering the computer resources available today.

In most engineering applications the Reynolds Averaged Navier Stokes equation (RANS) are usually solved. This approach solves the governing equations by modelling both the large and the small eddies, taking a time-average of variables. The information supplied by these models is the time-average of the variables. The fluctuating parts are not represented directly by the numerical simulation and are included only by means of a turbulence model. The main advantage is the relatively low computational effort involved compared to DNS. The RANS approach will be described in the following section.

2.5.1 Reynolds and Favre Averaging

In turbulent flows, the concept of time averaging (so-called Reynolds averaging) can be introduced for each instantaneous variable of the system (e.g. ϕ). Using this concept, the variable ϕ is determined from its mean part $\overline{\phi}$ and its fluctuation ϕ':

$$\phi = \overline{\phi} + \phi',\tag{2.34}$$

where ϕ is a component of the velocity vector or any scalar. Inserting equation 2.34 with the appropriate variable into a conservation equation will lead to the well-known Reynolds averaged Navier-Stokes equations. More details about the Reynolds averaging are derived in [53].

Since the heat release due to chemical reactions causes strong density variations, reacting flows have to be considered as compressible flows even if the Mach number is low. As a consequence, the classical approach to model turbulent flows with time averaging techniques is formally extended to include non-constant density effects by introducing the Favre-averaging method. This method decomposes the local variable ϕ into its Favre-averaged value $\tilde{\phi}$ and its fluctuation ϕ'':

$$\phi = \tilde{\phi} + \phi'',\tag{2.35}$$

Furthermore, the Favre-averaged mean value is defined by the following expression:

$$\tilde{\phi} = \frac{\overline{\varrho\phi}}{\overline{\varrho}}, \tag{2.36}$$

A Favre-averaged and a time-averaged quantity are related to each other by:

$$\tilde{\phi} = \overline{\phi} + \frac{\overline{\varrho'\phi'}}{\overline{\varrho}}. \tag{2.37}$$

From equation 2.37, it is clear that if the density fluctuations are negligible, a Favre and a Reynolds-averaged quantity are identical. This may occur in specific cases such as an incompressible flow. Furthermore, the conservation of momentum (Equation 2.2) using the Favre-averaging method can be formulated by the following expression:

$$\frac{\partial}{\partial t}\left(\overline{\varrho}\tilde{u}_i\right) + \frac{\partial}{\partial x_j}\left(\overline{\varrho}\tilde{u}_i\tilde{u}_j + \widetilde{\overline{\varrho u_i'' u_j''}}\right) = -\frac{\partial \overline{p}}{\partial x_i} + \frac{\partial \overline{\tau_{ij}}}{\partial x_j} + \overline{\varrho}g_i, \tag{2.38}$$

where $\widetilde{\overline{\varrho u_i'' u_j''}}$ are the Reynolds stresses. On the other hand, the conservation equation of the scalar quantity ϕ is written as:

$$\frac{\partial}{\partial t}\left(\overline{\varrho}\tilde{\phi}\right) + \frac{\partial}{\partial x_j}\left(\overline{\varrho}\tilde{u}_j\tilde{\phi} + \widetilde{\overline{\varrho u_j'' \phi''}}\right) = \frac{\partial}{\partial x_j}\left(\Gamma_\phi \frac{\partial \tilde{\phi}}{\partial x_j}\right) + \overline{S_\phi}, \tag{2.39}$$

where $\widetilde{\overline{\varrho u_j'' \phi''}}$ are known as the turbulent scalar fluxes. A detailed description of the Favre-averaging method can be found elsewhere [115].

2.5.2 The $k - \varepsilon$ Model

Due to the introduction of the Reynolds stresses and the turbulent scalar fluxes, the averaged transport equations have to be closed. The simple $k - \varepsilon$ model is very common and widely applied for many applications [59]. According to the $k - \varepsilon$ turbulence model, the Reynolds stress is related linearly to the strain rate:

$$\widetilde{\overline{\varrho u_i'' u_j''}} = -\mu_{turb}\left(\frac{\partial \tilde{u}_i}{\partial x_j} + \frac{\partial \tilde{u}_j}{\partial x_i} - \frac{2}{3}\delta_{ij}\frac{\partial \tilde{u}_k}{\partial x_k}\right) + \frac{2}{3}\delta_{ij}\varrho k. \tag{2.40}$$

where the turbulent kinetic energy k is given by:

$$k = \frac{1}{2}\frac{\overline{\varrho u_i'' u_j''}}{\overline{\varrho}} \tag{2.41}$$

Here, the turbulent viscosity μ_{turb} is defined as:

$$\mu_{turb} = C_\mu \overline{\varrho} \frac{\tilde{k}^2}{\tilde{\varepsilon}}, \tag{2.42}$$

where the dissipation rate of the kinetic energy is defined by:

$$\tilde{\varepsilon} = \frac{\mu}{\varrho} \left(\overline{\frac{\partial u_i''}{\partial x_j} \frac{\partial u_i''}{\partial x_j}} \right). \tag{2.43}$$

The turbulent scalar fluxes in equation 2.39 are given through the gradient-diffusion hypothesis by:

$$\overline{\varrho \widetilde{u_j'' \phi''}} = -\frac{\mu_{turb}}{\sigma_\phi} \frac{\partial \tilde{\phi}}{\partial x_j}, \tag{2.44}$$

with σ_ϕ denotes the turbulent Prandtl/Schmidt number for ϕ.

Two transport equations are solved in the $k - \varepsilon$ model, one for the turbulent kinetic energy, and the other for the dissipation rate. The equations are derived in a semi-empirical way and written as:

$$\frac{\partial \overline{\varrho} \tilde{k}}{\partial t} + \frac{\partial \overline{\varrho} \tilde{u}_j \tilde{k}}{\partial x_j} = \frac{\partial}{\partial x_j} \left(\Gamma_k \frac{\partial \tilde{k}}{\partial x_j} \right) + G_k - \overline{\varrho} \tilde{\varepsilon}, \tag{2.45}$$

$$\frac{\partial \overline{\varrho} \tilde{\varepsilon}}{\partial t} + \frac{\partial \overline{\varrho} \tilde{u}_j \tilde{\varepsilon}}{\partial x_j} = \frac{\partial}{\partial x_j} \left(\Gamma_\varepsilon \frac{\partial \tilde{\varepsilon}}{\partial x_j} \right) + \frac{\tilde{\varepsilon}}{\tilde{k}} \left(C_{\varepsilon 1} G_k - C_{\varepsilon 2} \overline{\varrho} \tilde{\varepsilon} \right). \tag{2.46}$$

Here, the production term G_k for the turbulent kinetic energy is expressed as:

$$G_k = \mu_{turb} \left[\frac{1}{2} \left(\frac{\partial \tilde{u}_i}{\partial x_j} + \frac{\partial \tilde{u}_j}{\partial x_i} \right)^2 - \frac{2}{3} \left(\frac{\partial \tilde{u}_k}{\partial x_k} \right)^2 \right], \tag{2.47}$$

and the diffusion coefficients Γ_k and Γ_ε are given by:

$$\Gamma_k = \mu + \frac{\mu_{turb}}{\sigma_k}, \quad \Gamma_\varepsilon = \mu + \frac{\mu_{turb}}{\sigma_\varepsilon}. \tag{2.48}$$

The constants of the standard $k - \epsilon$ model have been experimentally determined, given as: $C_\mu = 0.09$; $C_{\varepsilon 1} = 1.44$; $C_{\varepsilon 2} = 1.92$; $\sigma_k = 1.0$; $\sigma_\varepsilon = 1.3$ [96].

As an option, the differential Reynolds stress model (RSM) can be applied especially to obtain a better predictive quality to the flow with strong streamline curvature, as, e.g. in the near burner area of swirl burners. A comparative study between the $k - \epsilon$ model and the RSM model has been made by Schneider [96].

2.6 Boundary Conditions

A further problem regarding the solution of Navier Stokes equation as well as the other transport equations is the requirement to set the values on the boundary of the calculation domain. Two types of boundary conditions may be utilized for this purpose, one is the Dirichlet boundary condition and the other is the Neumann boundary condition. The first type specifies the values of dependent variable as a constant on the boundary, whereas the second type specifies that the gradient of a solution has to be taken on the boundary of the domain. All boundary values except pressure at inlets and wall cells can be set based on the Dirichlet boundary conditions, for example, the velocity is zero on the wall (non-slip condition). On the other hand, the boundary values at outlets or on the symmetry axis and periodical boundaries are set based on the Neumann boundary conditions. Near to the wall cells, velocity fluctuations and thus the Reynolds stresses are damped. This effect is taken into account by implementation of a simple model to solve the Navier Stokes equation and the transport equations of the turbulence model. As illustrated in Fig. 2.2, the region near to the wall is divided into the laminar and inertial sublayers. The velocity in the boundary layer is defined as:
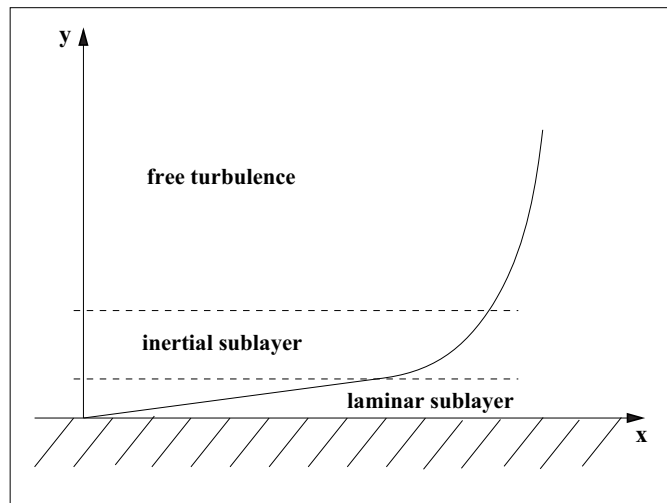

Figure 2.2: Schematic illustration of the region near to the wall [90].

$$u^+ = \frac{u_{turb}}{u_\tau} \tag{2.49}$$

where u^+ represents a characteristic dimensionless velocity and u_τ is the friction velocity, defined as:

$$u_\tau = \sqrt{\frac{\tau_w}{\varrho}} \tag{2.50}$$

where τ_w is the wall shear stress and ϱ is the gas density. Afterwards, the dimensionless characteristic length, y^+ can be related to those variables as:

$$y^+ = \frac{y\,u_\tau}{\nu} \tag{2.51}$$

Here, y denotes the distance of the center point of a near-to-wall cell to the wall. Furthermore, the dimensionless characteristic length, y^+ together with the friction velocity, u_τ are the factors affecting the value of the turbulence velocity parallel to the wall, u_T. In the laminar sublayer, the characteristic dimensionless velocity and the dimensionless length characteristic are identical, and mathematically this is expressed as:

$$u^+ = y^+ \quad , where\ y^+ < 11.26 \tag{2.52}$$

whereas in the inertial sublayer, the characteristic dimensionless velocity is related to the dimensionless length characteristic based on a logarithmic function:

$$u^+ = \frac{1}{\kappa} ln\left(E\,y^+\right) \quad , where\ 11.26 < y^+ < y_0^+\ ;\ 60 \le y_0^+ \le 500 \tag{2.53}$$

In this relation, κ refers to the Von Karman constant which has the value of 0.41, and E is the Prandtl empirical constant which has the value of 9.0. Beyond those layers, the flow behaviour is not affected by the existence of the wall.

To solve the momentum balance, a special treatment is made to calculate the source term in the cell near to the wall. This is accommodated by the calculation of the wall shear stress in the cells. In case that the wall cells are in the laminar sublayer, the wall shear stress is formulated as follows:

$$\tau_w = \frac{\mu\,u_{turb}}{y} \quad , where\ y^+ < 11.26 \tag{2.54}$$

If the center point of a cell near to the wall is in the inertial sublayer, the friction velocity is defined as:

$$u_\tau = C_\mu^{0.25}\sqrt{k} \tag{2.55}$$

where C_μ is a constant in the $k - \varepsilon$ model ($C_\mu = 0.09$). In the inertial sublayer, the wall shear stress is expressed by the following equation:

$$\tau_w = \frac{\kappa\,C_\mu^{0.25}\varrho\,\sqrt{k}\,u_{turb}}{ln\left(\frac{E\,C_\mu^{0.25}\varrho\sqrt{k}\,y}{\mu}\right)} \quad , where\ 11.26 \leqslant y^+ \leqslant y_0^+ \tag{2.56}$$

In addition, the turbulent kinetic energy and the dissipation rate in the cells near to the wall are calculated as follows:

$$k = \frac{\tau_w}{\sqrt{C_\mu}\,\varrho} \;\; ; \;\; \varepsilon = \frac{C_\mu^{0.75}\,k^{1.5}}{\kappa\,y} \tag{2.57}$$

The formulation of the wall shear stress, the friction velocity and the variables for the turbulence model (the turbulent kinetic energy and the dissipation rate) are derived under the assumption that production term and dissipation term are locally in equilibrium [90].

2.7 Modelling of Two-Phase Flow

In pulverized coal combustion, the behaviour of a two-phase flow involving flue gas and particles has to be described. From a practical point of view, a continuous phase assumption can be used in case that low particle loading prevails in many areas of the combustion unit. This approach offers the most important advantage, e.g. reducing mathematical and numerical complexity. Furthermore, the transport equations of all species including the coal particles are written in a Eulerian framework. However, the modelling assumption is not always valid in coal-fired boilers where the interaction between the mean velocity and turbulent fluctuations of gas phase and of particles can not be neglected. This occurs especially in the burner near field.

As an alternative, a fully coupled Eulerian/Lagrangian two-phase flow method has recently been developed and applied [55]. In this approach, the differential equations of momentum, mass and enthalpy for the fluid phase are still formulated and solved with the Eulerian approach, whereas the Lagrangian approach is used for particles. The Lagrangian approach treats the particulate phase as a single particle and predicts the particle trajectories in the fluid phase. The interaction between the fluid phase and the particle phase is handled by the PSIC (particle-source in cell) method [17]. According to the PSIC method, the repercussions of the particle motion and of the mass and heat transfer on the gas phase, as a result of the preceding particle combustion, are included as contributions to the source terms in the respective transport equation of the gas phase quantity. Based on the modelling experience, the Lagrangian method requires sufficient trajectories and a slower iteration progress to obtain smooth-gradient information and to ensure a converged numerical solution [54, 90].

The Lagrangian approach for modelling the particle phase is also implemented to the deposition model described in the next chapter. In the following, the main governing equations for the Lagrangian treatment are introduced. More details about this approach can be drawn from [17, 54].

The description of the Lagrangian approach is started from the momentum equation of a single particle of class i:

$$\frac{d\,(m_{p,i}\,u_{p,i})}{dt} = F_D + F_{ex} \tag{2.58}$$

where m_p denotes the particle mass, u_p represents the instantaneous velocity of the particle, F_{ex} is the sum of all external volume forces and F_D is the drag force between the particle and fluid. In case that $\varrho_g/\varrho_p \leq 10^{-3}$, the gravitational force can be considered as the only external force acting on the particles [55]. Thus, the drag force (F_D) and the external force (F_{ex}) are defined as follows:

$$F_D = C_D \frac{\mu}{d_p} \frac{Re_p}{2} A_p \left(u_g - u_{p,i}\right) \tag{2.59}$$

$$F_{ex} = m_p\, g \left(1 - \frac{\varrho_g}{\varrho_p}\right) \tag{2.60}$$

Here, the subscripts g and p represent gas and particle, respectively, μ is the molecular viscosity, u is the instantaneous velocity and C_D is the drag coefficient, described by:

$$C_D = \frac{24}{Re_p} \left(1 + 0.15 Re_p^{0.687}\right) \tag{2.61}$$

Assuming spherical particles, the particle Reynolds number, Re_p, is related to the particle diameter, d_p, the dynamic viscosity, μ and the density of the gas phase, ϱ_g as well as the gas phase and particle phase velocities:

$$Re_p = \frac{|u_p - u_g|\, d_p \varrho_g}{\mu} \tag{2.62}$$

Assuming that the fluid velocity and the particle mass remain constant during a short time interval Δt, the instantaneous value of the particle velocity can be obtained by solving Equation 2.58 analytically:

$$u_p = u_g + \left(u_p^0 - u_g\right) exp\left(-\frac{\Delta t}{\tau_p}\right) + \tau_p\, g \left(1 - \frac{\varrho_g}{\varrho_p}\right) \left[1 - exp\left(-\frac{\Delta t}{\tau_p}\right)\right] \tag{2.63}$$

where u_p^0 is the initial particle velocity at the beginning of the time interval Δt. The particle relaxation time is a measure for the time required until the particle has adjusted to the gas phase velocity which is defined by:

$$\tau_p = \frac{4}{3} \frac{\varrho_p d_p^2}{\mu C_D Re_p} \tag{2.64}$$

In order to obtain a reasonable result with respect to the particle-tracking, the time step Δt should be determined properly. Firstly, the particle is not allowed to pass through the calculated cell within one time step. In addition, it must be smaller than the particle relaxation time and the eddy life time. Based on the $k - \varepsilon$ turbulence model [102], the characteristic eddy life time is expressed by:

$$t_E = \frac{C_\mu^{0.75}}{\sqrt{2/3}} \frac{k}{\varepsilon} \tag{2.65}$$

The new position of the particle at the end of the time interval, Δt, is:

$$x = x^0 + \Delta t \frac{u_p^0 + u_p}{2} \tag{2.66}$$

where x^0 is the initial position at the beginning of the time interval.

In order to quantify the influence of the turbulent fluid flow on the particle motion, a Monte Carlo-type approach is used. With this method, the instantaneous gas velocity is calculated as summation of two components, one is the mean gas velocity, $\bar{u}$ obtained from the Eulerian approach and the other is the fluctuating gas velocity, u':

$$u_g = \bar{u} + u' \tag{2.67}$$

The fluctuating gas velocity, u', is computed from the variables of the turbulence model. Using the $k - \varepsilon$ turbulence model and assuming an isotropic turbulence, the velocity fluctuation is calculated as the function of the mean velocity fluctuations and a random vector r_Z normally distributed in the interval [-1,1]:

$$u' = \sqrt{\frac{2}{3}k} \cdot r_Z, \quad where -1 \leq r_Z \leq 1 \tag{2.68}$$

2.8 Modelling of Combustion

In terms of combustion modelling, the conversion of coal/biomass in general is assumed to follow the main reaction steps: pyrolysis, volatiles combustion and char burnout. In addition to biomass combustion, a drying process is considered before those processes take place. The drying process is modelled as a heat transfer controlled process between the particle and the surrounding gas. A more detailed description of this process can be extracted from Deeg [22]. Once the biomass particle is dried, it is considered similar to a lignite coal particle during combustion. In the present work, combustion modelling is described by a global model involving two heterogeneous reactions: devolatilization and char combustion, and two homogeneous reactions: the oxidation of hydrocarbons and that of carbon monoxide. A short description of the global model will be given in the following sections whereas more details about the model can be found elsewhere [27].

2.8.1 The Heterogeneous Reactions

The pyrolysis is described by a single reaction of dry-and-ash-free coal (RC_{daf}) decomposing into volatiles, i.e. hydrocarbons (C_xH_y), carbon monoxide (CO) and water vapor (H_2O), and leaving char (C):

$$|\nu_{1,RC}|\, RC_{daf} \longrightarrow \nu_{1,C}C + \nu_{1,C_xH_y}\, C_xH_y + \nu_{1,CO}\, CO + \nu_{1,H_2O}\, H_2O \qquad (2.69)$$
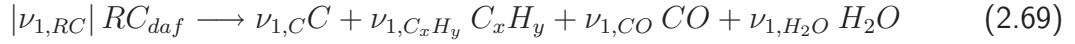
In this reaction, the water content of the coal is assumed to be evaporated when entering the furnace, and the ash is considered as inert. The stoichiometric coefficients of the reaction are predicted by the elementary analysis of the coal and the hydrocarbons. The rate of pyrolysis is modelled according to the Arrhenius expression which is written as:

$$\frac{dm_{RC}}{dt} = -m_{RC} \cdot k_{0,1} \cdot exp\left(-\frac{E_1}{\Re\, T_p}\right) \qquad (2.70)$$

where $k_{0,1}$ and E_1 are the frequency factor and the activation energy of the first reaction, respectively, which are coal-type dependent. This work utilizes average values of $E_1 = 74 \cdot 10^9\,(J/kmol)$, $k_{0,1} = 1.5 \cdot 10^5\,(1/s)$ for bituminous coal and $k_{0,1} = 3.15 \cdot 10^5\,(1/s)$ for lignite coal. The residual solid after pyrolysis (char) is further oxidized yielding carbon monoxide and carbon dioxide. In the present work, the formation of CO_2 is assumed to be negligible at temperatures prevailing in char combustion:

$$\nu_{2,C}C + \nu_{2,O_2}O_2 \longrightarrow \nu_{2,CO}CO \qquad (2.71)$$

The carbon oxidation rate is proportional to the specific surface area of the particles, A_p, and to the partial pressure of oxygen, p_{O_2}:

$$\frac{dm_C}{dt} = -m_C \cdot A_p \cdot p_{O_2} \cdot \frac{k_2^{ch}\, k_2^{ph}}{k_2^{ch} + k_2^{ph}} \qquad (2.72)$$

The reaction is limited on one hand by the diffusive transport both of oxygen to the particle and of CO from the particles (k_2^{ph}), and on the other hand by the chemical reaction (k_2^{ch}). The mass transfer coefficient is obtained as follows:

$$k_2^{ph} = \frac{48 \cdot 10^5\, D_{O_2}}{d_p\, \Re\, T_p} \qquad (2.73)$$

Here, D_{O_2} represents the diffusion coefficient of O_2, d_p is the particle diameter, $\Re$ is the universal gas constant and T_p is the particle temperature. Furthermore, the chemical reaction is described based on an Arrhenius equation:

$$k_2^{ch} = k_{0,2}\, exp\left(-\frac{E_2}{\Re\, T}\right) \qquad (2.74)$$

where the frequency factor, $k_{0,2}$, and the activation energy, E_2, of the carbon oxidation are $208 \times 10^{-5} \, kg/\left(m^2 \cdot s \cdot Pa\right)$ and $80 \times 10^9 \, J/kmol$, respectively. These are the average values to be representative for all coals. The diffusion coefficient D_{O_2} of oxygen is calculated by:

$$D_{O_2} = 3.49 \times 10^{-4} \left(\frac{T}{1600}\right)^{1.75} \tag{2.75}$$

where D_{O_2} is in $m^2 s^{-1}$, and T is in K.

2.8.2 The Homogeneous Reactions

The volatiles combustion mechanism concerning the hydrocarbons and carbon monoxide oxidation are summarized by the following global reactions:

$$\nu_{3,C_xH_y}C_xH_y + \nu_{3,O_2}O_2 \longrightarrow \nu_{3,CO}CO + \nu_{3,H_2O}H_2O \tag{2.76}$$

$$\nu_{4,CO}CO + \nu_{4,O_2}O_2 \longrightarrow \nu_{4,CO_2}CO_2 \tag{2.77}$$

In this work the hydrocarbon as the major combustible species in the coal volatiles is represented by CH$_4$ [53]. The kinetics of the reactions are given as follows:

$$\frac{dc_{CH_4}}{dt} = -k_{0,3} \cdot T^{0.5} \cdot exp\left(-\frac{E_3}{\Re T}\right) \cdot c_{CH_4} \cdot c_{O_2} \quad \left[\frac{kmol}{m^3 \cdot s}\right] \tag{2.78}$$

$$\frac{dc_{CO}}{dt} = -k_{0,3} \cdot exp\left(-\frac{E_4}{\Re T}\right) \cdot c_{CO} \cdot c_{O_2}^{0.5} \cdot c_{H_2O}^{0.5} \quad \left[\frac{kmol}{m^3 \cdot s}\right] \tag{2.79}$$

The reactions are modelled by first order Arrhenius equation with parameters: $k_{0,3} = 2.33 \times 10^{11} \, m^3/\left(kmol \cdot s \cdot T^{0.5}\right)$, $E_3/\Re = 20131 \, K$, $k_{0,4} = 1.3 \times 10^{11} \, m^3/\left(kmol \cdot s\right)$, $E_4/\Re = 15098 \, K$. As a consequence of working with mass fractions, the reaction rates w_i are required to be expressed as mass fraction which can be written as follows:

$$w_i = \varrho \cdot \frac{1}{\nu_{i,j}} \cdot \frac{dY_j}{dt} \tag{2.80}$$

Here, ϱ denotes the mixture density, $v_{i,j}$ is the stoichiometric coefficient and Y_j is the mass fraction. Subscript i and j refer to the reaction number and the considered species, respectively. The mass fraction and the molar concentration can be related to each other by the following expression:

$$Y_j = \frac{M_{M_j} \cdot c_j}{\varrho} \tag{2.81}$$

where c_j is the molar concentration of species j and M_{M_j} is the molar mass of species j. Inserting equation 2.81 into equation 2.80 yields:

$$w_i = \frac{M_{M_j}}{\nu_{i,j}} \cdot \frac{dc_j}{dt} \tag{2.82}$$

Based on equation 2.82 and equation 2.81, the reaction kinetics given in equations 2.78 and 2.79 can be utilized to obtain the reaction rate of the homogeneous reactions in terms of mass fractions:

$$w_3 = \frac{1}{-\nu_{3,CH_4}} \cdot k_{0,3} \cdot T^{0.5} \cdot exp\left(-\frac{E_3}{\Re T}\right) \cdot \frac{\varrho^2}{M_{M_{O_2}}} \cdot Y_{CH_4} \cdot Y_{O_2} \tag{2.83}$$

$$w_4 = \frac{1}{-\nu_{4,CO}} \cdot \frac{k_{0,4} \cdot exp\left(-\frac{E_4}{\Re T}\right) \cdot \varrho^2}{\sqrt{M_{M_{O_2}} \cdot M_{M_{H_2O}}}} \cdot Y_{CO} \cdot Y_{O_2}^{0.5} \cdot Y_{H_2O}^{0.5} \tag{2.84}$$

Furthermore, those reaction rates will have contribution to the source term of the species mass balance equation. A detailed description can be found in [96].

2.9 Turbulence-Chemistry Interaction Model

In terms of turbulence-chemistry interaction, chemistry affects turbulent flow via heat release causing density variation (see section 2.5.1). On the contrary, the fluctuations of species concentrations and of the temperature as well as the micro-mixing may affect the reaction rate of the homogeneous reactions. Several models have been proposed for modelling the influence
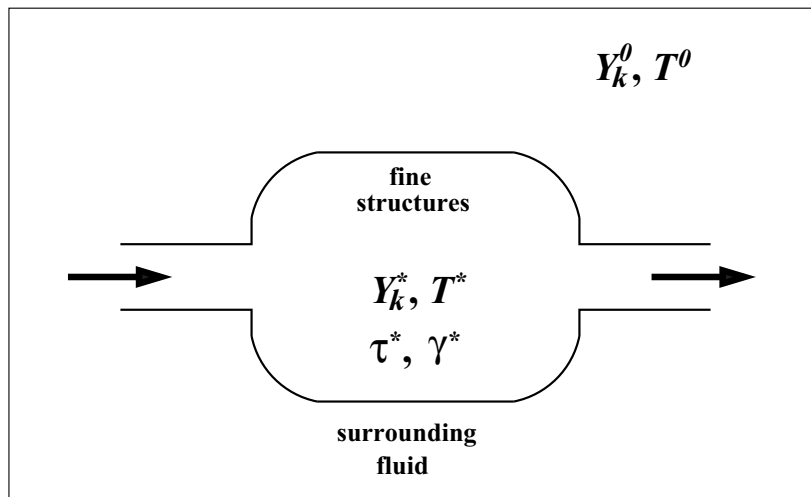
Figure 2.3: Schematic illustration of the EDC Model [27].

of turbulence on the mean reaction rates of species. These are, e.g., the Eddy-Break-Up (EBU) model, the Eddy Dissipation Concept (EDC) model, PDF methods and Flamelet models. A

brief description of the models can be found in [53]. In this work, the EDC model is used for the gas phase reactions, both for the combustion model and for the alkali release model described in the following chapter. In the EDC model, the turbulent flame space is subdivided into a reaction space, the *fine structures*, and the *surrounding fluid*. All homogeneous reactions having more than one reactant are assumed to take place only in the fine structures which are locally treated as a perfectly-stirred reactor (PSR) transferring mass and energy only to the surrounding fluid. A schematic illustration of the EDC is represented in Fig. 2.3. Superscript $*$ and 0 refer to the fine structures and surrounding fluid, respectively. The reaction rate of a species is calculated from the species conservation equation for the fine structures (PSR):

$$\frac{\varrho^*}{\tau^* \cdot (1 - \gamma^*)} \cdot \left(Y_k^* - \widetilde{Y}_k \right) \quad = \quad \Upsilon \cdot \left(Y_k^* - \widetilde{Y}_k \right) \quad = \quad M_{M_k} \cdot w_k^*, \tag{2.85}$$

where Y_k represents the mass fraction of the species k, w_k^* is the chemical reaction rate of the species k, ρ is the density, and $\Upsilon = \rho^* / (\tau^* \cdot (1 - \gamma^*))$. In order to solve the mass balance, the mean residence time and the mass fraction of the fine structures, represented by τ^* and ρ^*, have to be determined. The mean residence time is related to the dissipation of turbulent kinetic energy, ε, and the kinematic viscosity, ν as:

$$\tau^* \quad = \quad 0.41 \cdot \sqrt{\frac{\nu}{\varepsilon}} \tag{2.86}$$

The mass fraction of the fine structures is given in [65] by:

$$\gamma^* \quad = \quad \left[2.13 \cdot \left(\frac{\nu \cdot \varepsilon}{k^2} \right)^{0.25} \right]^{\kappa} \tag{2.87}$$

where k is the turbulent kinetic energy and κ is a constant ranging from 2 to 3. In this work, κ is taken as 2.

2.10 The 3D CFD-Code AIOLOS

AIOLOS is a program code for comprehensive modelling and simulation of pulverized coal and gas combustion processes. The application of AIOLOS ranges from the simulation of decentralized small-scale furnaces to that of large-scale power plant furnaces. The program covers the numerical modelling of fluid flow, heat transfer and combustion processes as well as the interactions between those models. A schematic illustration of such interactions is shown in Fig. 2.4. In addition, it has been extensively validated against experimental data and has been utilized in the past to optimize a variety of power plants covering a wide range of firing systems and fuels [92].
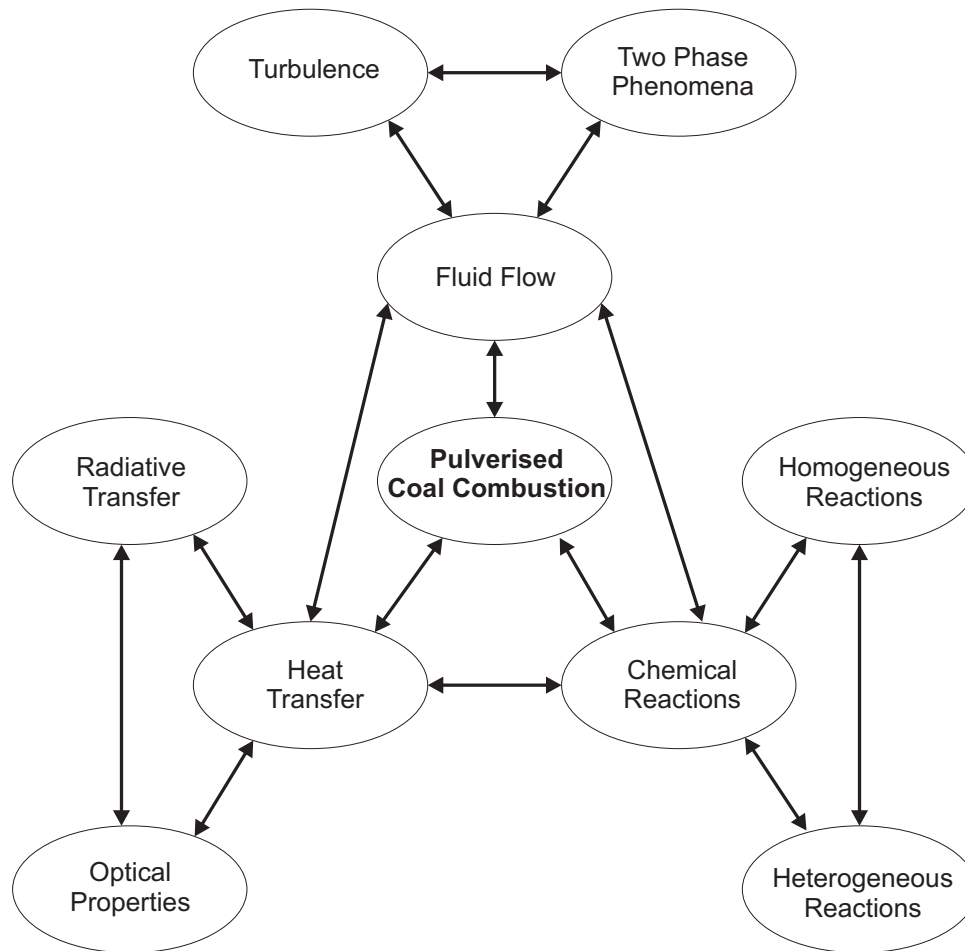
Figure 2.4: Interactions of pulverised coal combustion [98].

All simulations with AIOLOS are performed on node-centered non-staggered arrangements of grids. Different grid systems such as Cartesian, cylindrical, as well as Body Fitted Coordinates (BFC) can be applied for the discretization of the calculation domain. Velocity-pressure coupling is handled by using the SIMPLE method. As an alternative, the SIMPLEC method is also available for that purpose. The pressure interpolation from Date [18] is used to prevent decoupling of pressure and velocities on the non-staggered grid. Turbulence is calculated either by using a standard $k-\varepsilon$ model or differential Reynolds Stress model. By default, radiative heat transfer is modeled by a Discrete-Ordinates Method based on the implementation of Stroehle [108]. To determine the radiation properties of the particle-loaden gases, different models have been implemented [38]. The convective fluxes are calculated with the UPWIND scheme [96]. The behaviour of a two phase flow consisting of flue gas and particles is considered in a Eulerian frame. The combined Euler-Lagrange approach has been also implemented into AIOLOS. Regarding the combustion processes, the overall scheme proposed by Foertsch [27] is utilized to calculate the main processes of coal combustion. For biomass combustion, a model

for the drying process has been introduced as the initial step in addition to the combustion processes [22].

Furthermore, a domain decomposition method allows a local optimization of the discretization. Using this method, it is possible to couple a cylindrical coordinate system for the burner geometry with the furnace grids, i.e. with either one or more additional grids with different grid sizes. The implementation of the method together with parallelization and vectorization of the program code enables the code to handle large scale furnaces with complex geometries, firing concepts and burner layouts with up to several million cells by using modern supercomputers [62, 107].

3 On the Effect of Alkali Compounds on the Deposition Mechanisms

3.1 Occurrence of Alkali Metals, Si, Cl and S in Fuels

For a better understanding of the release of the alkali compounds in the gas phase and their effect on the deposition mechanism, the way how the particular elements are bound in the fuel matrix should be investigated. Coal and biomasses, especially biomass with high content of alkali differ substantially.
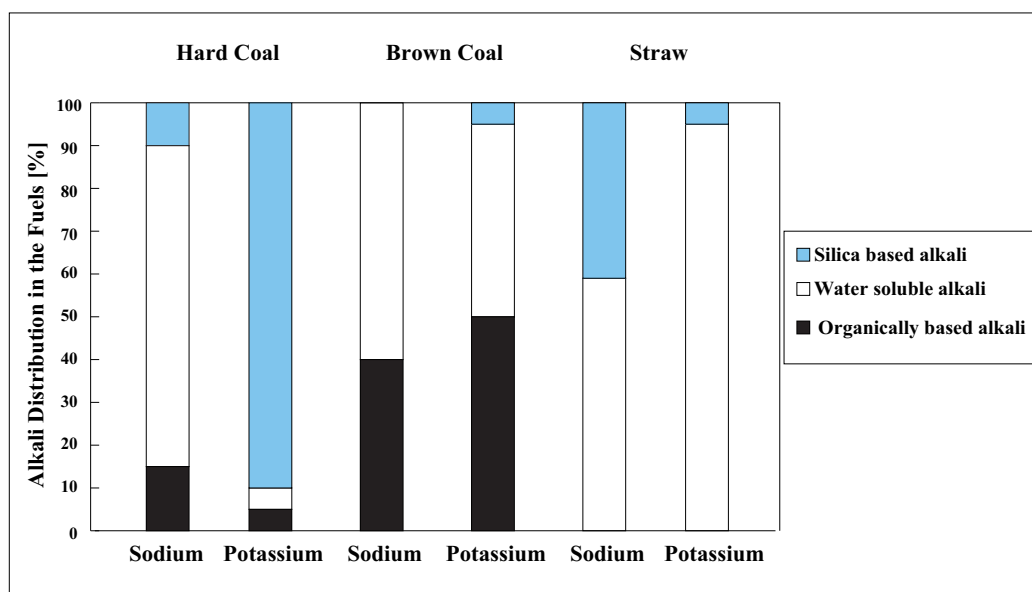
Figure 3.1: The typical distribution of organically based alkali, water soluble alkali and silica based alkali in straw and German coals [51, 104].

The alkali metals in a coal are believed to be bound as organically based alkali, silica based alkali and water soluble alkali. The distribution of the alkali forms in the coal may vary depending on the degree of coalification. Fig. 3.1 shows the distribution of the alkali forms for sodium and potassium in typical German hard and brown coals. It is common in the literature [85, 104, 105] that most of the potassium content in brown coal may be in organic and water soluble form. The fuel matrix of brown coals is highly porous and a large quantity of sodium is in the form of

exchangeable ions. In high rank coal, sodium occurs predominantly as NaCl which is soluble in water. Sodium in silica based minerals as illit may still be found in a small extent. Unlike sodium, most of potassium in this type of coal is in the silica based form. Up to 90% of potassium may occur in the form of aluminosilicates as $K_2O.[Al_2O_3]_3.[SiO_2]_6.[H_2O]$ and $K_2O.Al_2O_2.[SiO_2]_6$ [46, 84]. Those species are not easily released during the combustion process [31].

The sodium content of biofuels like straw is comparable with that of coal, whereas straw may contain about ten times more potassium than coal. Potassium in biomass plays an important role related to plant metabolism and the osmotic processes inside plant cells [31, 126]. Chemical fractionation experiments have been performed by a number of investigators to assess the mode of occurrence of alkali in fuels [8]. In these experiments, the fuel is leached in progressively more aggressive solvents; water, AAc (ammonium acetate), and HCl. The chemical fractionation test shows that over 90 % of potassium in straw is available as water soluble and ion exchangeable material which is easily to vaporize during combustion (see Fig. 3.1). The predominant form of potassium varies depending on agricultural factors such as the type of plant, the soil properties, the extent of fertilization and the amount of rain to which the plant has been exposed [37]. According to the work of Wornat [127], pine (wood) and switchgrass contain alkali metals which are bound with the oxygen containing functional groups within the organic matrix because of the high content of oxygen in the biomass. The vaporization behaviour of these alkali metals under combustion conditions is similar to that of low-rank coals.

According to Glazer [31], sulfur and chlorine are present in anionic forms as plant nutrient in biomass. Both biomass and coal contain relatively high amounts of silica. Silica appears essentially in the form of aluminosilicates in coal. The sulfur content in the coal can be found in organic and inorganic forms. Organic sulfur appears in the coal structure, either in aromatic rings or aliphatic functional groups, whereas the inorganic sulfur present essentially in form of pyrite (FeS_2) appears in coal as dispersed particles [38]. Chlorine in the coal structure exists in the form of NaCl as discrete mineral particles or in ionic form [84].

3.2 Alkali Metals Behaviour

3.2.1 Release of Alkali in Coal

During the combustion of coal, part of the alkalis in coal is released into the gas phase. Parallel to the alkalis release, bonding of the alkalis by the mineral species occurs affecting the formation of alkali compounds in the gas phase [85]. On the contrary to the potassium content, most of the sodium content is in the form of water soluble material which is easy to vaporize during coal combustion. Sodium is frequently found in the fouling-type boiler deposits [78, 103]. A number of investigations have been performed to study the behaviour of alkali release under coal combustion conditions. In this subsection, the scope of the discussion will be limited to

the alkali release behaviour of hard coal. Some extensive studies concerning the release of alkali for brown coal can be found in [24, 85].

Release of sodium has been investigated in the work of Wen [122]. He measured the alkali release of an American hard coal during pyrolysis in the temperature range of 1000 $°C$ to 2000 $°C$. The measurements were done in-situ in a slagging combustor by using atom absorption spectroscopy (AAS) technique. The coals, one which is first cleaned with hot water and the other which is untreated were observed and the results are presented in Fig. 3.2. From the figure, it can be seen that the release of alkali during pyrolysis for the untreated coal began at a temperature of about 1100 $°C$ and increases with the increase of temperature. At the temperature of 1400 $°C$ to 1600 $°C$, no alkali release was observed then, above the temperature of 1600 $°C$, the rest of alkali is further released into the gas phase. On the other hand, release of the alkali for the cleaned coal occurred in one step starting from the temperature of 1300 $°C$.
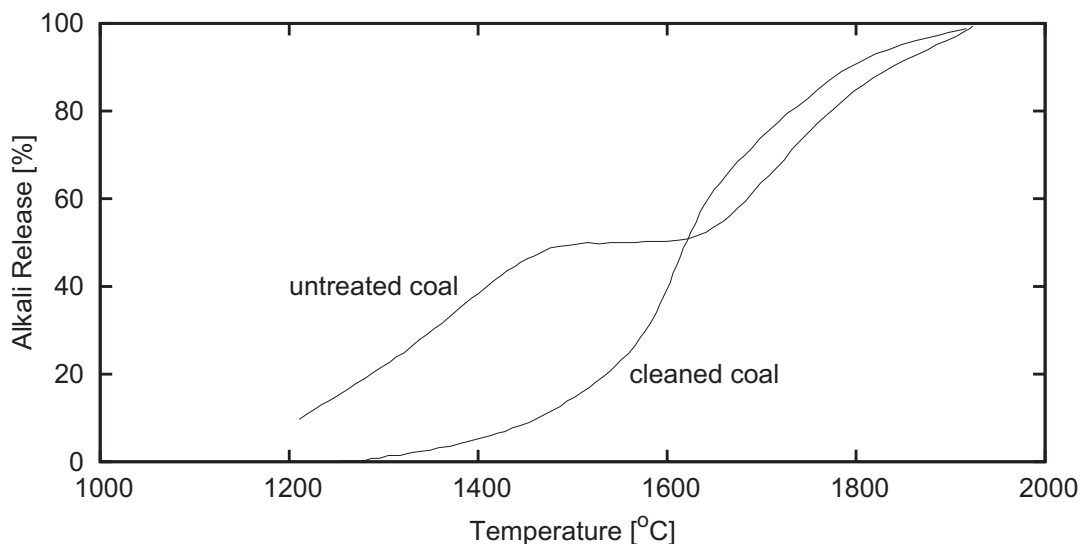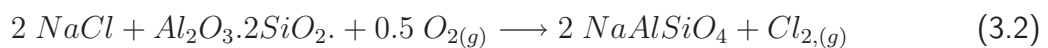

Figure 3.2: The release of alkali from an American hard coal as function of temperature for untreated coal and cleaned coal. Adapted from [122].

It can be concluded that the released alkali in the range of the investigated temperature comes from two sources related to the occurrence of sodium in the hard coal. One is the sodium which exists as chloride in water soluble form and the other is the sodium in silica based form. The water soluble sodium vaporizes below 1500 $°C$, whereas the silica based sodium vaporizes at the temperature starting from 1600 $°C$. In general, only the sodium in water soluble form is considered as the alkali which is released into the gas phase related to the deposition mechanisms during the combustion process of hard coal [45, 83].

Another investigation on the alkali release behaviour of hard and brown coals has been done by Neville and Sarofim [72]. This work aimed to study on one hand the alkali release mechanism and on the other hand the alkali bonding by Quartz particles. The reaction between sodium and Quartz will form sodiumsilica (Na_2SiO_3). From this investigation, it was found that the alkali release can be modelled as a physical vaporization process. Furthermore, it was observed that both processes - release of alkali and bonding of alkali - depend on the temperature. A positive correlation was found between temperature and those processes. From the experimental results, it can also be concluded that the vaporized alkali increases with the increase of chlorine content in the coal. In contrast, the measured alkali in the gas phase is lower with the higher silica content in the coal.

In contrast to the experimental results of Wen, the release of silica based alkali at the temperature above 1600 $°C$ was not observed in the work of Neville. Wen performed the experiments in an inert gas environment so there was no bonding reaction occurring during the experiment, whereas Neville performed his experiments in an O_2 atmosphere that may promote the bonding of alkali by SiO_2. It has also been reported that the increase of the water vapor content favors binding of sodium into the coal minerals [85, 101].

The alkali bonding by metakaolinite has been investigated by Steffin [104] in an inert and in an oxidizing O_2/H_2O atmosphere. The experiments were performed by using silica particles impregnated with NaCl. The reaction between sodium chloride and metakaolinite (Reaction 3.1) was not observed in an inert atmosphere, whereas bonding reactions occur in an oxidizing O_2/H_2O atmosphere according to Reaction 3.2 and 3.3.

$$NaCl + Al_2O_3.2SiO_2 \xrightarrow{N_2, CO_2, CO} NaCl_{(g)} + Al_2O_3.2SiO_2 \tag{3.1}$$

$$2\,NaCl + Al_2O_3.2SiO_2. + 0.5\,O_{2(g)} \longrightarrow 2\,NaAlSiO_4 + Cl_{2,(g)} \tag{3.2}$$

$$2\,NaCl + Al_2O_3.2SiO_2. + H_2O_{(g)} \longrightarrow 2\,NaAlSiO_4 + 2\,HCl_{(g)} \tag{3.3}$$
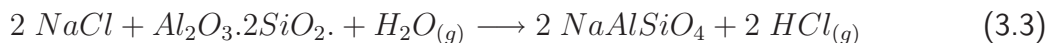
3.2.2 Release of Alkali in Biomass

Potassium release during biomass combustion plays a significant role in terms of ash deposit formation and high temperature corrosion of the superheater tubes. The sodium content in biomass is relatively low so the effect of sodium on the deposition is not very likely. Potassium may be released in a significant amount during devolatilization of the biomass. This was suggested based on the works of Olsson et al. [77] and Davidsson et al. [20]. Olsson studied the alkali release of wheat straw, whereas Davidsson studied the alkali release of birchwood material and wheat straw. From the studies it was found that increasing of temperature causes

an increasing amount of alkali released. It has been suggested in the work of Davidsson that there are two types of alkalis, one is the "pyrolysis alkalis" which is bound in organic form in the biomass structure and the other is the ash alkalis which is emitted in the higher temperature range. Moreover Davidsson [21] found that the smaller particles release more alkali per unit initial particles mass during rapid pyrolysis of birchwood particles. In the investigation of Jensen [49], chlorine is released primarily as HCl during pyrolysis at relatively low heating rates. Afterwards, KCl and KOH are released during char combustion. Bonding of alkali may also occur in parallel with alkali release during biomass combustion. Because of the high content of silica in biomass, the alkali metals are most likely incorporated into the biomass silica structure. It has been investigated by Hald [37] that the gaseous alkali content increases with:

- increasing temperature
- decreasing pressure
- increasing chlorine content in the fuel
- decreasing sulfur content in the fuel if the conditions are oxidizing.

In contrast to the work of Davidsson [19–21], the work of Jensen [49] shows that the amount of potassium released into the gas phase is not significant below 700 $^\circ C$. In the temperature range of 700-830 $^\circ C$, evaporation of potassium as KCl and bonding of potassium take place in parallel. In this temperature range, potassium is bound either to the silica structure or to the organic matrix. In the higher temperature range of 830-1000 $^\circ C$, decomposition of K_2CO_3 occurred and potassium was released as KOH or atomic K. Above the temperature range, potassium in the silica based form is supposed to be released into the gas phase.

In the case of coal and straw co-combustion, secondary reactions between the released alkali and the aluminosilicate in the coal structure may take place. Such reactions are more likely for higher thermal shares of the coal. It was suggested in the work of Wei [121] that above 1000 K, potassium is combined with aluminosilicates from the coal to form $KAlSi_2O_6$ in the solid mineral. In general, straw contains low amount of aluminum, but high amount of silicon. Furthermore, by increasing the thermal share of straw, potassium is more likely to react with the silica instead of the aluminosilica to form $K_2Si_4O_{9[liq]}$. This indicates that the formation of $K_2Si_4O_9$ in liquid mineral may have contribution to the formation of slagging ash.

3.2.3 Alkali Compounds in the Flue Gas

After vaporization, alkali encounters the complex chemical environment that affects the conversion of the alkali in the gas phase [103]. Thus, alkali may exist in the gas phase in the form of sulfate (Na_2SO_4, K_2SO_4), hydroxide (NaOH, KOH) or chloride (NaCl, KCl) [42]. Srinivasachar [103] has developed the homogeneous reactions of alkali in a chlorine containing environment. Chlorine in the coal matrix is rapidly released as HCl into the gas phase prior to the release

of sodium. This behaviour has been observed in other works [23, 100]. These works reported that release of HCl from coal as well as biomass starts at about 200 $°C$ with a significant amount observed between 300 $°C$ and 400 $°C$ and is terminated at about 600 $°C$. Several pathways exist for the formation of NaCl from reactions of Na, NaO, and NaOH. NaO$_2$ may react with atomic chlorine to also form NaCl. Schematically, a variety of chemical reactions concerning the formation of NaCl is shown in Fig. 3.3. The important reactions and their reaction rate coefficients governing the formation and destruction of sodium chloride can be found in Table A.1. Furthermore, Srinivasachar has investigated the effect of chlorine content on the predominant species which is formed in the gas phase. According to the investigation, most of the sodium compounds at a low chlorine to sodium content is in the form of hydroxide, whereas at a high chlorine to sodium content, chlorination of sodium is favored and NaCl dominates the vapor phase chemistry. Also for potassium, the importance of alkali chloride (KCl) has been suggested by Hansen [39] in the case of straw (biomass) containing a high amount of chlorine.
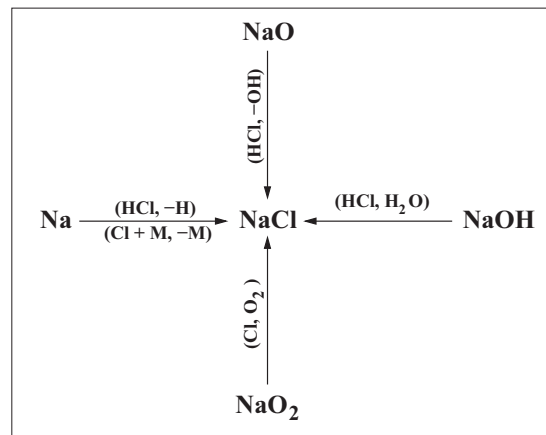
Figure 3.3: Schematic illustration of sodium chloride formation in a chlorine containing environment. Adapted from [103].

The alkali chloride and alkali hydroxide may be converted to alkali sulfate with the availability of SO$_2$ and SO$_3$ in an oxidizing atmosphere. An experimental study has been performed concerning the formation of sulfate in the gas and molten phase [47]. From this study, it was observed that the conversion of KCl to K$_2$SO$_4$ was significantly faster in the gas phase; up to 100 % conversion was obtained in the vapor phase under most conditions but only 0.5-2 % conversion in the melt. The results suggest that the most of KCl sulfation occurs in the gas phase. Glarborg et al. [30] have proposed a model for conversion of gaseous AOH (alkali hydroxide) and ACl (alkali chloride). The model relies on a detailed reaction mechanism for the high-temperature gas-phase interactions between alkali metals, the O/H radical pool, and chlorine/sulfur species. Particular attention is paid to alkali hydrogen sulfates and alkali oxysulfur chlorides as potential gas-phase precursors of A$_2$SO$_4$. Sulfation is initiated by oxidation of SO$_2$ to SO$_3$. Afterwards, sulfur trioxide recombines with alkali hydroxide or alkali chloride

to form an alkali hydrogen sulfate, AHSO$_4$, or an alkali oxysulfur chloride, ASO$_3$Cl. From the calculations, both of these compounds are sufficiently stable in the gas phase to act as precursors for formation of alkali sulfate. Another model regarding the conversion of alkali chloride to sulfate has been suggested by Tomeczek [111]. The reaction mechanism is shown in Table 3.1.

Table 3.1: Rate and Equilibrium Constants of Reactions Producing Na$_2$SO$_4$ and K$_2$SO$_4$: $k_i = k_{0,i}\, exp\left(-E_i/\Re T\right)$ and $K_i = C\, exp\left(D/T\right)$ [111]

Reaction	$k_{0,i}$ $\left(m^3/kmol\, s\right)$	E_i $(J/kmol)$	C	D (K)
S$_2$+2O$_2$ $\leftrightarrow$ 2SO$_2$	1.9 x 10^{11}	1.85 x 10^8	1.6 x 10^{-4}	43488
SO$_2$+0.5O$_2$ $\leftrightarrow$ SO$_3$	1.5 x 10^5	2.30 x 10^6	1.4 x 10^{-5}	11850
2NaCl$_{(g)}$+H$_2$O$_{(g)}$+SO$_{2(g)}$+0.5O$_{2(g)}$ $\leftrightarrow$Na$_2$SO$_{4(g)}$+2HCl$_{(g)}$	5.0 x 10^{11}	1.01 x 10^7	1.5 x 10^{-21}	76040
2KCl$_{(g)}$+H$_2$O$_{(g)}$+SO$_{2(g)}$+0.5O$_{2(g)}$ $\leftrightarrow$K$_2$SO$_{4(g)}$+2HCl$_{(g)}$	4.9 x 10^{11}	1.01 x 10^7	2.3 x 10^{-21}	72640

3.2.4 The Formation of the Alkali Compounds in This Work

To have a better prediction of the alkali effect on the deposition mechanisms, a more comprehensive model for the formation of the alkali compounds is necessary. A detailed model considering at least several important aspects is rarely reported in the literature. Hence, a model for the formation of the alkali compounds including the alkali release during the primary step, the homogeneous reactions, and the secondary reaction is proposed in this work.

In the case of coal combustion, the primary step of alkali release is modelled based on the work of Steffin [104]. In the model, it is assumed that the water soluble alkali (NaCl), an important species related to fouling of the superheaters, is released into the gas phase in the primary step of hard coal combustion. Decomposition of alkali and bonding of alkali are considered during the primary step of the alkali release. The consumption rate of solid NaCl in the combustion process is described by a first-order rate expression:

$$\frac{dm_{NaCl,coal}}{dt} = -k_{dec} \cdot m_{NaCl,coal} - k_{bon} \cdot m_{NaCl,coal} \quad (3.4)$$

where the first term on the right side of the equation refers to the part of solid NaCl which is vaporized into the gas phase (Reaction 3.1), whereas the second term refers to the bonding of NaCl into the aluminosilicate (Reaction 3.3). The rate of both reactions (k_{dec} and k_{bon}) is calculated as follows:

$$k_i = k_{0,i} \cdot exp\left(-\frac{E}{\Re T}\right) \quad (3.5)$$

The constants for the decomposition rate and the bonding rate have been experimentally determined as shown in Table 3.2. The formation of NaCl in the gas phase during alkali release is expressed by:

$$\frac{dm_{NaCl,(g)}}{dt} = k_{dec} \cdot m_{NaCl,coal} \tag{3.6}$$

Table 3.2: Rate Constants of the Decomposition and Bonding Reaction of NaCl [104]

Reaction	Frequency factor $k_{0,i}$ $[\frac{1}{min}]$	Activation Energy E_i $[J/kmol]$
Decomposition	8.2 x 10^9	239 x 10^6
Bonding	3.9 x 10^7	157 x 10^6

After having been released into the gas phase, the homogeneous reactions may occur which are modelled based on the reaction mechanism proposed by Srinivasachar [103] for the sodium-chlorine system. NaCl may be converted to sulfate with the availability of sulfur in the gas phase. The global model which is suggested by Tomeczek [111] in Table 3.1 is implemented in AIOLOS for the sulfation process. A small modification was made concerning the formation of SO_2 in the gas phase. Instead of using the model proposed by Tomeczek, in this work the formation of SO_2 which has been developed by Han [38] to model the SO_x reduction processes in pulverized coal furnaces is used. In the model, the organic sulfur is released mostly as H_2S during the devolatilization process [5, 129]. The released H_2S is then oxidized to SO_2 according to the global mechanism:

$$H_2S + \frac{3}{2}O_2 \rightarrow SO_2 + H_2O \tag{3.7}$$

A kinetic model for the H_2S oxidation process has been proposed in [114]. The inorganic sulfur (in the form of pyrite) left in the coal after pyrolysis is assumed to be released directly as SO_2 parallel to the char burnout. On the other hand, a part of the chlorine in the coal is assumed to be converted to HCl parallel to the devolatilization process, and the other part is vaporized during the alkali release according to reaction 3.1. There is an investigation reported by Raask [84] that almost 50 % of chlorine in the coal is released as HCl without corresponding loss of sodium.

The reaction rate in turbulent flows is not only determined by chemical kinetics but also affected by turbulent flow characteristics. The Eddy Dissipation Concept (EDC) which has been applied by many researchers [28, 65, 76] is used to model the interaction between turbulence and chemistry for the homogeneous reactions of alkali in the gas phase. More details about the EDC model can be found in [66, 67].

In addition to the bonding reaction in the primary step of alkali release, a secondary reaction between the released alkali and the aluminosilicate in the fly ash may occur [104, 126]. Fig.3.4
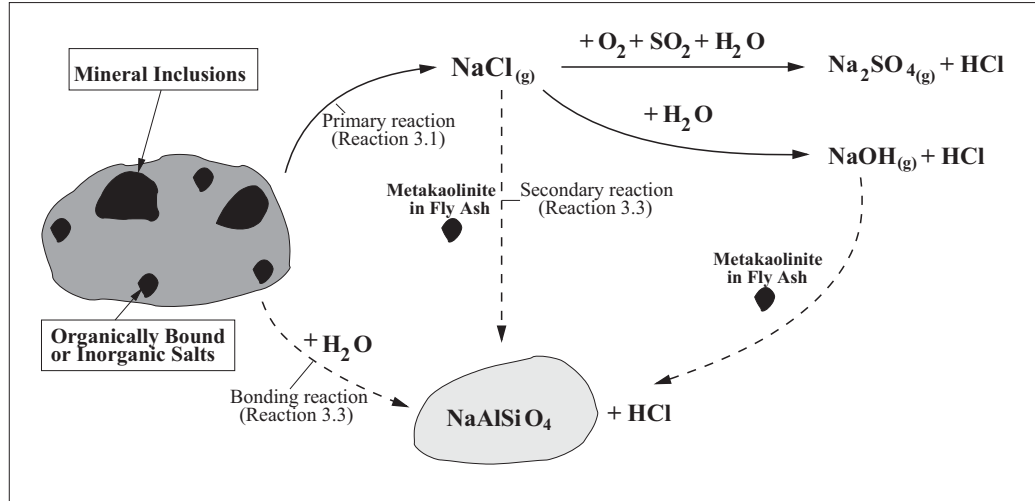
Figure 3.4: Schematic illustration of alkali release and alkali conversion during coal combustion.

shows the model of the global processes of alkali release involving the primary step and the heterogeneous reaction between $NaCl_{(g)}$ and aluminosilicate. Considering the typical residence time of alkali in furnaces, it seems that the secondary reaction may have a significant effect on the alkali behaviour during the combustion process, and the effect increases as the residence time increases [104]. In the present work, the secondary reaction is modelled analogue to the char burn out model implemented in AIOLOS. More details about the char burn out model can be found in [96]. The following reaction scheme has been proposed to model the secondary reaction in the case of combustion of hard coal [81, 104]:

$$2\ NaCl_{(g)} + H_2O + Al_2O_3.2SiO_2 \longrightarrow 2\ NaAlSiO_4 + 2\ HCl_{(g)} \tag{3.8}$$
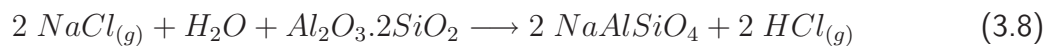
In this work, the aluminosilicate is presented as metakaolinite ($Al_2O_3.2SiO_2$). The consumption rate of metakaolinite is proportional to the specific surface area of the particle, A_p, and to the mass of the metakaolinite, m_{kao} itself:

$$\frac{dm_{kao}}{dt} = -k_{eff} \cdot A_p \cdot m_{kao} \tag{3.9}$$

The reaction rate is on one hand limited by a physical rate (diffusive process), k^D and on the other hand by a chemical reaction, k^{ch}, described by an Arrhenius equation [104]. By using the '*Resistance Equation*' (RE) concept, the effective reaction rate k_{eff} is governed proportionally to the partial pressure of sodium chloride, p_{NaCl}:

$$k_{eff} = p_{NaCl}\ \frac{k^{ch} \cdot k^D}{k^{ch} + k^D} \tag{3.10}$$

$$k^{ch} = k_{0,i} \, exp \left(-\frac{E}{\Re \, T_p} \right) \tag{3.11}$$

$$k^D = \frac{2 M_{M_{Al_2O_3.2SiO_2}} \, f \, D_{NaCl}}{d_p \, \Re \, T_p} \times 10^5 \tag{3.12}$$

where d_p, T_p, $\Re$, $M_{M_{Al_2O_3.2SiO_2}}$, f are the particle diameter in m, the particle temperature in K, the universal gas constant in $JK^{-1}kmol^{-1}$, the molar mass of metakaolinite, and the reaction coefficient of $Al_2O_3.SiO_2$ in Reaction 3.8, respectively. The pre-exponential factor, $k_{0,i}$, and the activation energy, E, of the secondary reaction are 2.548 $kg/\left(m^2.s.Pa\right)$ and 4.1462×10^7 $(J/kmol)$, respectively. The diffusion coefficient D_{NaCl} of sodium chloride is defined as proposed in [48]:

$$D_{NaCl} = 1.425 \times 10^{-10} \times T^{1.88} \tag{3.13}$$

Hence the secondary reaction rate of NaCl, w_{bon}, can obtained by the following expression:

$$w_{bon} = -\frac{|\nu_{NaCl}|}{|\nu_{Al_2O_3.2SiO_2}|} \cdot k_{eff} \cdot A_p \cdot m_{kao} \cdot \varrho \tag{3.14}$$

where ν_{NaCl} and $\nu_{Al_2O_3.2SiO_2}$ are the stoichiometric coefficients of NaCl and $Al_2O_3.2SiO_2$, respectively. Further description regarding the reaction rate which is implemented in AIOLOS can be found in [96].

In this model, metakaolinite, $Al_2O_3.2SiO_2$ is assumed to be distributed homogeneously in the char particle. In addition, no transport equation for metakaolinite was implemented in the model, so the consumption rate of metakaolinite in the particle is assumed to be parallel with that of char in the particle during combustion. However, the secondary reaction rate of NaCl$_{(g)}$ with metakaolinite is governed by the diffusive rate and the chemical rate of Reaction 3.8. With regard to diffusion, the model only considers boundary layer diffusion and some important phenomena such as char porosity, change in pore structure and external surface area during combustion, and possible catalytic effects are neglected [53].

This modelling strategy implemented for sodium may be also applicable for potassium. Some additional efforts are needed to modify the model according to the properties of potassium. A model in terms of the heterogeneous and the homogeneous reactions for the potassium release can be found in [1].

3.3 Transport and Deposition Mechanisms

Ash deposit formation on the heat transfer surfaces is governed at least by five major mechanisms: inertial impaction, eddy impaction, thermophoresis, condensation and chemical reactions [6, 56]. According to Lokare [64], each of the mechanisms has a specific driving

force, namely momentum, turbulence intensity, temperature gradients, vapor pressure of alkali compounds, and species concentration gradients, respectively. In fact, the models for the mechanisms were developed for coal combustion, however, they are also applicable for biomass combustion with the difference on the relative importance of the mechanisms [51].

3.3.1 Condensation

Condensation takes place when vapors pass over (relatively) cool heat transfer surfaces. Vapors entering the thermal boundary layer around a cool surface are expected to be in the condensed phase and subsequently deposited on the surface. The condensible species arrive on the heat transfer surface by at least three mechanisms [14, 44, 94], see Fig.3.5:

- Vapor diffusion followed by heterogeneous condensation on the surface.

- Homogeneous nucleation in the thermal boundary layer forming a fume followed by particle diffusion, eddy impaction, or thermophoresis on the surface.

- Heterogeneous condensation on existing fly ash particles followed by inertial impaction or eddy impaction or thermophoresis on the surface.
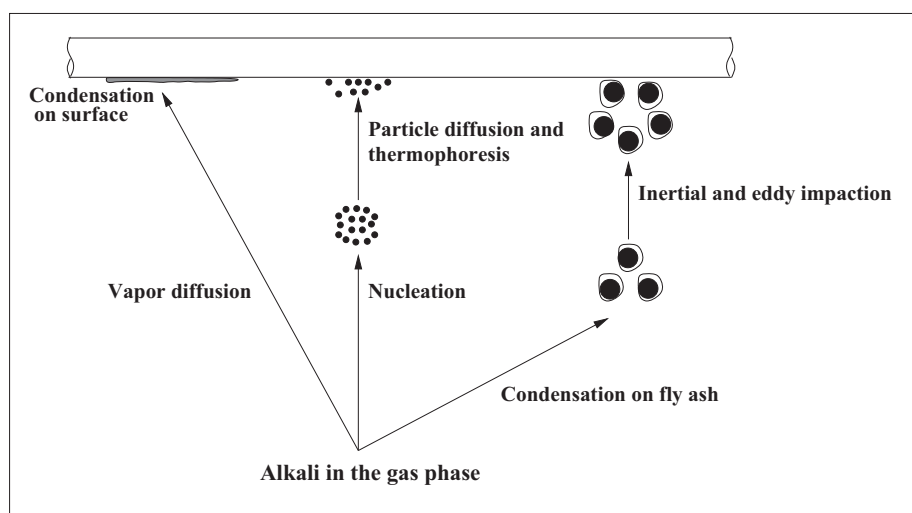
Figure 3.5: Schematic representation of vapor deposition mechanisms adapted from [51].

Considering the mode of occurrence of the inorganic material in the fuels, low grade fuels such as lignites, biomass and other similar fuels may produce large quantities of condensible species implying a significant contributor of condensation to the deposit formation. On the contrary, condensation has relatively minor contribution to the deposit build-up for most high-rank coals [6].

During the condensation process, homogeneous nucleation needs relatively high saturation pressure to occur [45]. Furthermore, in case boundary layer condensation is not fast enough, direct condensation by vapor diffusion may be a dominant mechanism of the deposit build-up. A number of models that allow for boundary layer condensation on aerosol particles are available in the literature [15, 48, 50, 80, 83]. However, it has been demonstrated in many sources that considering direct vapor deposition as the only deposition mechanism in the combustion process shows a reasonable result within an acceptable error [6, 45, 51, 64, 111].

Direct condensation models by vapor diffusion have been presented in the literature [10, 39, 45]. Actually, the models were used to determine the condensation rate of a specific alkali species, however, the models may be applied also for any other species with a special attention on the properties such as diffusion coefficient and molar mass depending on the alkali species of interest. In the following, some condensation models developed for biomass and coal combustion will be briefly described.

Hansen's Model

Fig.3.6 shows a schematic illustration of the condensation model proposed by Hansen [39]. The temperature profile is assumed to be linear through the stagnant film layer. The condensation rate of the gaseous component is governed by the rate of diffusion through the film layer, which can be approximated as follows:

$$\dot{n}_{C,i} = D_i \cdot c_G \cdot \frac{d\psi_i}{dy} \tag{3.15}$$

where $\dot{n}_{C,i}$, c_G, D_i, and ψ_i are the molar flux $[kmol/m^2 s]$ of species i, the total gas concentration $[kmol/m^3]$ at the given temperature and pressure, the diffusivity of species i in the gas $[m^2/s]$, and the mole fraction of species i in the gas, respectively. The diffusion coefficient (regarded as the binary diffusion coefficient) is a function of temperature and can be expressed as:

$$D_{12} = \frac{0.001858 \cdot T^{3/2} \cdot \left(\left(M_{M_1} + M_{M_2}\right)/M_{M_1} \cdot M_{M_2}\right)^{1/2}}{p \cdot \sigma_{12}^2 \cdot \Omega_D} = \frac{K_D}{\Omega_D} \cdot T^{3/2} \tag{3.16}$$

In the equation above, T denotes temperature, M_{M_1} and M_{M_2} denote the molar masses of the two components, p is the pressure, whereas σ_{12} and Ω_D are the constants depending on temperature and material [10]. Subscript 1 and 2 refer to the condensible species and the gas mixture, respectively. In the last part of Equation 3.16, all parameters except Ω_D and temperature are included in the constant K_D. Ω_D is assumed to be constant in the relevant temperature range (600 - 1000 $°C$). The constants for KCl diffusion in N_2 are given in [39] as: $\sigma_{12} = 3.9035$; $\Omega_D = 1.016$. After the insertion of Equation 3.16 into Equation 3.15, the diffusion rate can be expressed as follows:

$$\dot{n}_{C,i} = -\frac{K_D}{\Omega_D} \cdot T^{3/2} \cdot \frac{p}{\Re\, T} \cdot \frac{d\psi_i}{dy} \tag{3.17}$$

where $\Re$ in Equation 3.17 is the universal gas constant. The flux through the film layer is assumed to be independent of position (in y-direction), and this is expressed as:

$$\frac{d}{dy}\left(\dot{n}_{C,i}\right) = \frac{d}{dy}\left(\frac{p\,K_D}{\Re\,\Omega_D}\cdot T^{1/2}\cdot\frac{d\psi_i}{dy}\right) = 0 \qquad (3.18)$$

Furthermore the following boundary conditions are applied to solve the differential equation:

$$\begin{aligned} y = 0 \;&\rightarrow\; \psi_i = \psi_{i,s} \;,\; T = T_s \\ y = \delta_\psi \;&\rightarrow\; \psi_i = \psi_{i,bulk} \;,\; T = T_{bulk} \end{aligned} \qquad (3.19)$$

And since $\psi_{i,s} << \psi_{i,bulk}$, the condensation flux can be expressed by the following equation:

$$\dot{n}_{C,i} = \frac{p\cdot K_D}{\Re\,\Omega_D}\cdot\psi_{i,bulk}\cdot\frac{\Delta T}{2\,\delta_\psi}\cdot\frac{1}{T_{bulk}^{1/2} - (T_{bulk} - \Delta T)^{1/2}} \qquad (3.20)$$
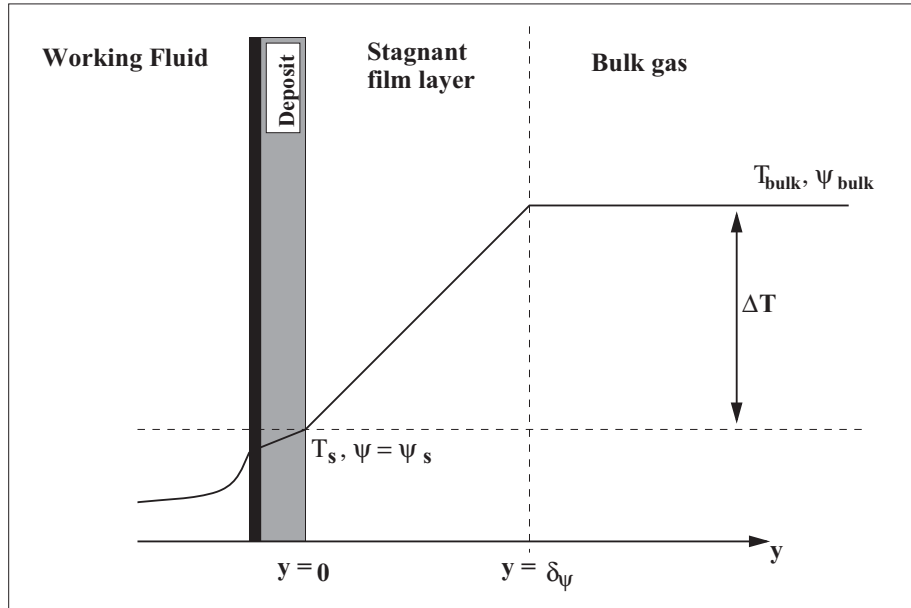
Figure 3.6: Schematic illustration of temperature and concentration gradient over boundary layer.

The equation above shows that the condensation flux is the function of bulk gas temperature, T_{bulk}, the temperature difference between bulk gas and tube surface, ΔT, and the thickness of the film layer, δ_ψ. The flux is dependent on the bulk gas concentration of component i, whereas in this case the effect of bulk gas temperature is not very likely. For the condensation onto a cylinder, the film layer thickness, δ_ψ, can be obtained from the Sherwood number in Equation 3.21, whereas the Sherwood number is expressed as the function of Reynolds number (Re) and Schmidt numbers (Sc) [69] (see Equation 3.23).

$$\delta_\psi = d_t/Sh \qquad (3.21)$$

$$Re = \varrho_g \cdot u_g \cdot d_t/\mu_g \qquad (3.22)$$

$$Sh = 0.61 \cdot Re^{0.5} \cdot Sc^{1/3} \qquad (3.23)$$

In Equation 3.21, d_t denotes the tube diameter, whereas the Reynolds number in Equation 3.22 is dependent on the density of gas, ϱ_g, the gas velocity, u_g, and the dynamic viscosity of gas, μ_g.

Film Theory

The condensation flux can be modelled also based on the film theory by Lewis. Fig. 3.7 shows the profiles of temperature, velocity, and concentration during the condensation process with the different boundary layer thicknesses δ_T, δ_v, and δ_ψ. In the model, the condensible
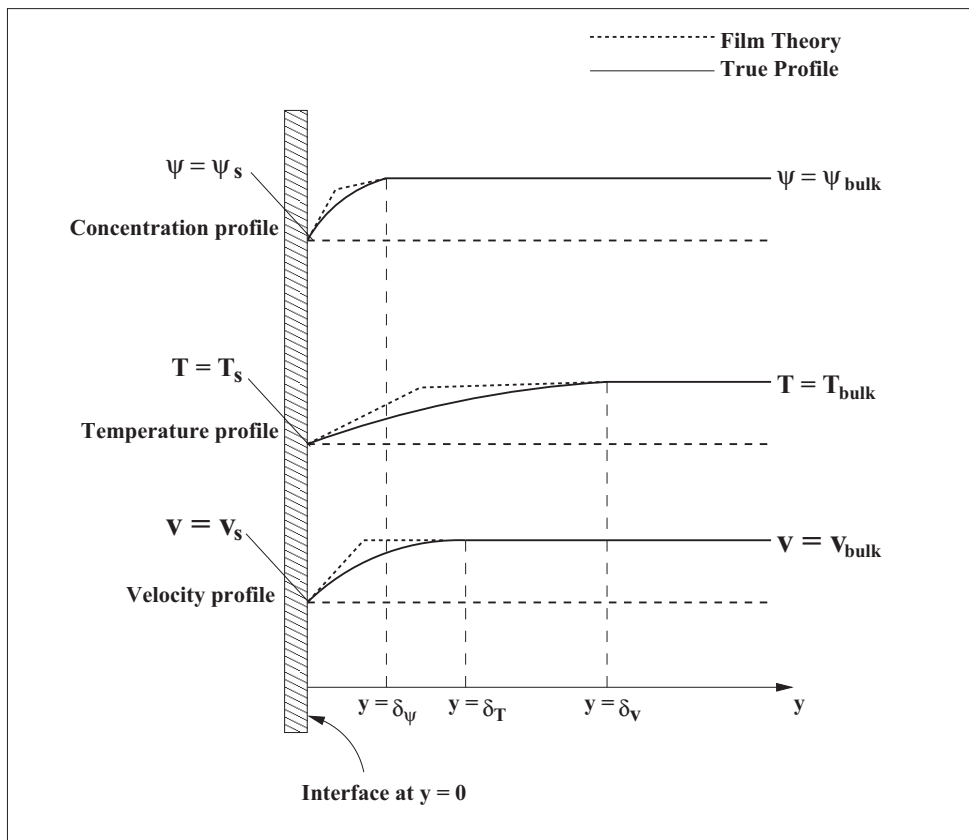
Figure 3.7: Profiles of boundary layer for temperature, velocity and concentration along a flat surface. The unbroken curves represent the true profiles, and the broken curve are the prediction of the film model [10].

species is transported in the boundary layer by diffusion and convection. Thus the molar flux of condensible species $\dot{n}_{C,i}$ towards the heat transfer surface is expressed as [10]:

$$\dot{n}_{C,i} = \underbrace{-c_G \cdot D_i \cdot \frac{\partial \psi_i}{\partial y}}_{\text{diffusive term}} + \underbrace{\psi_i \cdot (\dot{n}_{C,i} + \dot{n}_{inert})}_{\text{convective term}} \tag{3.24}$$

where $\dot{n}_{inert}$, c_G, D_i, ψ_i are the molar flux of an inert gas, the total gas concentration, the diffusion coefficient of condensible species i, and the mole fraction of condensible species i in the gas, respectively. It is assumed that $\dot{n}_{inert} = 0$ then the equation above may be re-arranged to the following equation:

$$\dot{n}_{C,i} = -\frac{c_G \cdot D_i}{1 - \psi_i} \cdot \frac{\partial \psi_i}{\partial y} \tag{3.25}$$

Similar to Hansen's model, the molar flux of condensible species i is taken to be constant in y-direction:

$$\frac{\partial \dot{n}_{C,i}}{\partial y} = 0 \tag{3.26}$$

By the use of the boundary conditions:

$$\psi_i \mid_{y=0} = \psi_{i,s} \tag{3.27}$$

$$\psi_i \mid_{y=\delta_\psi} = \psi_{i,bulk} \tag{3.28}$$

the differential equation (equation 3.24) can be solved to obtain the profile of condensible species i in the film layer as follows:

$$\left(\frac{1 - \psi_i}{1 - \psi_{i,s}} \right) = \left(\frac{1 - \psi_{i,bulk}}{1 - \psi_{i,s}} \right)^{\frac{y}{\delta_\psi}} \tag{3.29}$$

The derivative of ψ_i from equation 3.29 can be obtained as follows:

$$\frac{\partial \psi_i}{\partial y} = -(1 - \psi_{i,s}) \frac{1}{\delta_\psi} \left(\frac{1 - \psi_{i,bulk}}{1 - \psi_{i,s}} \right)^{\frac{y}{\delta_\psi}} ln \left(\frac{1 - \psi_{i,bulk}}{1 - \psi_{i,s}} \right) \tag{3.30}$$

Inserting this expression into equation 3.25, the molar flux of condensible species at $y = \delta_\psi$ is given by the following equation:

$$\dot{n}_{C,i} = \frac{D_i}{\delta_\psi} \cdot c_G \cdot ln \left(\frac{1 - \psi_{i,bulk}}{1 - \psi_{i,s}} \right) \tag{3.31}$$

By assuming that the gas at $y = \delta_\psi$ behaves as an ideal gas, the equation above may be written as follows:

$$\dot{n}_{C,i} = \frac{D_i}{\delta_\psi} \cdot \frac{p_G}{\Re \cdot T_G} \cdot ln \left(\frac{1 - \psi_{i,bulk}}{1 - \psi_{i,s}} \right) \tag{3.32}$$

By using the expression $\dot{m}_{C,i} = \dot{n}_{C,i} \cdot M_{M_i}$, where M_{M_i} is the molar mass of species i, the mass flux of species i, $\dot{m}_{C,i}$, can be expressed as follows:

$$\dot{m}_{C,i} = \frac{D_i}{\delta_\psi} \cdot \frac{p_G \cdot M_{M_i}}{\Re \cdot T_G} \cdot ln\left(\frac{1 - \psi_{i,bulk}}{1 - \psi_{i,s}}\right) \tag{3.33}$$

The boundary layer thickness, δ_ψ, can be obtained by using the formulation (equation 3.21) described in Hansen's model, whereas the mole fraction of species i at the surface deposit is calculated by the equation derived in Appendix A.2.

Goldbrunner's Model

The classic film theory which is described in the previous subsection is able to predict the condensation rate well in the case of horizontal flow along the heat transfer surface [45]. The model may still be used for vertical flows with the implementation of a correction factor. Hence, a model based on the generalized film theory has been developed by Goldbrunner [33]. The model will be described by starting from the one-dimensional mass balance equation:

$$\frac{\partial \psi_i}{\partial t} + \frac{\partial \dot{n}_{C,i}}{\partial y} = 0 \tag{3.34}$$

Equation 3.34 can be expanded to show its convective and diffusive terms. It is assumed that density and diffusion coefficient are constant, then the following equation can be obtained:

$$\underbrace{\frac{\partial \psi_i}{\partial t}}_{transient} + \underbrace{v\frac{\partial \psi_i}{\partial y}}_{convective} = \underbrace{D_G \cdot \frac{\partial^2 \psi_i}{\partial y^2}}_{diffusive} \tag{3.35}$$

For a binary system, the equation above may be written as:

$$\begin{aligned} \frac{\partial \psi_i}{\partial t} + \left((\dot{n}_{C,i} + \dot{n}_{inert})\frac{\partial \psi_i}{\partial y}\right) \\ = D_G \cdot c_G \cdot \left(\frac{\partial^2 \psi_i}{\partial y^2}\right) \end{aligned} \tag{3.36}$$

With $\psi_{inert} = 0$ and steady state conditions assumed, the equation can be simplified as follows:

$$\dot{n}_{C,i} \cdot \frac{\partial \psi_i}{\partial y} = D_G \cdot c_G \cdot \frac{\partial^2 \psi_i}{\partial y^2} \tag{3.37}$$

The following boundary conditions are applied to solve the differential equation:

$$\psi_i \mid_{y=0} = \psi_{i,s}, \quad \psi_i \mid_{y=\delta_\psi} = \psi_{i,bulk} \tag{3.38}$$

$$\frac{\partial \psi_i}{\partial y}\Big|_{y=\delta_\psi} = 0, \qquad \frac{\partial \dot{n}_{C,i}}{\partial y} = 0 \tag{3.39}$$

After integrating the differential equation twice, it can be obtained:

$$\frac{\psi_{i,bulk} - \psi_i}{\psi_{i,bulk} - \psi_{i,s}} = e^{\left(\dot{n}_{C,i} \frac{y}{c_G \cdot D_G} \right)} \tag{3.40}$$

The condensation flux can be expressed based on Equation 3.40 as:

$$\dot{n}_{C,i} = c_G \cdot \frac{D_G}{y} \cdot ln \left(\frac{\psi_{i,bulk} - \psi_i}{\psi_{i,bulk} - \psi_{i,s}} \right) \tag{3.41}$$

According to Hoppe [45], it is difficult or even impossible to determine the boundary layer thickness, δ_ψ, where $\psi_i = \psi_{i,bulk}$. A constant has to be defined as the ratio of the concentration of condensible i at $y = \delta_\psi$ to that of condensible i in the bulk gas, for example:

$$\frac{\psi_i\,(\delta_\psi)}{\psi_{i,bulk}} = 0.95 \tag{3.42}$$

Goldbrunner has made some calculations with constants ranging from 0.95 to 0.99. The calculation results have been compared to experimental ones. Based on his investigation, a constant of 0.97 was proposed as the ratio of ψ_i at $y = \delta_\psi$ to $\psi_{i,bulk}$. Using this ratio, Equation 3.41 can be written as follows:

$$\dot{n}_{C,i} = c_G \cdot \frac{D_G}{\delta_\psi} \cdot ln \left(\frac{0.03 \cdot \psi_{i,bulk}}{\psi_{i,bulk} - \psi_{i,s}} \right) \tag{3.43}$$

This condensation flux may also be expressed on a mass basis by the following equation:

$$\dot{m}_{C,i} = \frac{D_G}{\delta_\psi} \cdot \frac{p_G \cdot M_{M_i}}{\Re \cdot T_G} \cdot ln \left(\frac{0.03 \cdot \psi_{i,bulk}}{\psi_{i,bulk} - \psi_{i,s}} \right) \tag{3.44}$$

3.3.2 Inertial Impaction

The deposition mechanism by inertial impaction is most important for large particles (10 μm or larger) [6, 51]. In this process, large particles have sufficient inertia to traverse the gas stream lines and impact on the heat transfer surface. The rate of inertial impaction depends on target geometry, particle size and density, and gas flow properties [6]. The rate of inertial impaction can be expressed as the function of the dimensionless impaction efficiency, η_p. The impaction efficiency is defined as the ratio of the number of particles impacting the surface (N_i) to the number directed towards the surface in the free stream (N_C). Fig. 3.8 shows the schematic illustration of this concept for the particle impacting a tube in cross flow. In the literature, the formulation of the impaction efficiency is started by defining the characteristic time or length scales of the particle motion (τ_p) and the flow field (τ_f):

$$\tau_p = \frac{\varrho_p \cdot d_p^2}{18\,\mu_g}\psi \quad [s] \tag{3.45}$$

$$\tau_f = \frac{L}{u_{char}} = \frac{d_t/2}{u_g} \quad [s] \tag{3.46}$$

where ϱ_p, d_p, μ_g, ψ are the particle density (kg/m^3), the particle diameter (m), the gas viscosity $(kg/m\,s)$, and a correction factor accounting for deviations from Stokes law. The ratio of these time scales yields the well-known definition of the Stokes number, Stk.

$$Stk = \frac{\varrho_p\, d_p^2\, u_g}{9\,\mu_g\, d_t}\psi \tag{3.47}$$
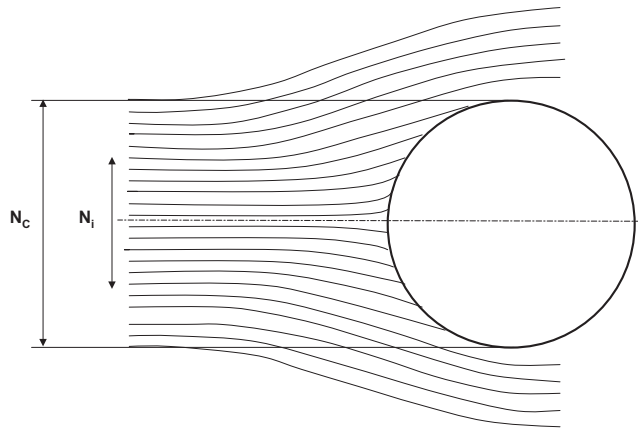
Figure 3.8: Schematic illustration of the impaction efficiency ($\eta_p = N_i/N_c$) [51].

A correlation between the impaction efficiency with the Stokes number for a single cylinder in cross flow has been addressed by several researchers:

$$\eta_p\,(Stk) = \frac{1}{1 + b\,(Stk - a)^{-1} - c\,(Stk - a)^{-2} + d\,(Stk - a)^{-3}} \tag{3.48}$$

where η_p represents the impaction efficiency. Some sets of coefficients for Equation 3.48 proposed by different investigators can be seen in Table 3.3. The coefficients proposed by Israel and Rosner were determined on the base of the empirical correlations to modeled results. The model used conventional particle trajectories and a potential flow field around a cylinder in cross flow [64]. Two sets of coefficients were also given by Baxter in Table 3.3, one with the effect of thermophoresis (Baxter-a) and the other without this effect (Baxter-b). It is shown in Fig. 3.9 that the impaction efficiencies in equation 3.48 which are calculated with three different sets

Table 3.3: Coefficients for equation 3.48 from different investigators [51]

	a	b	c	d
Israel and Rosner	0.125	1.25	-0.014	0.00508
Baxter-a	0.1425	1.28	0.00215	0.00587
Baxter-b	0.1238	1.34	-0.034	0.0289

of coefficients from Table 3.3 are identical [51]. A minor difference exists only at a relatively low Stokes number. This is most pronounced if it is calculated by using the coefficient with the effect of thermophoresis (Baxter-b).
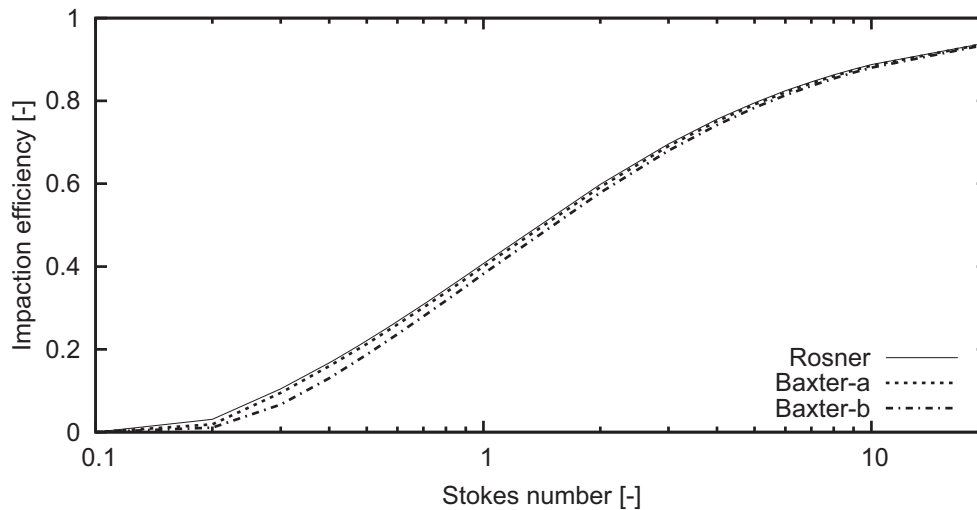

Figure 3.9: The calculated impaction efficiency vs the Stokes number. The curve is generated based on Equation 3.48 and the coefficients in Table 3.3 [51].

It has been investigated that angular position (θ) may affect the impaction efficiency of the particle onto a cylinder [123]. This is illustrated schematically in Fig. 3.10. The impaction efficiency was observed to be maximum at the forward stagnation point of the cylinder. With the increase of angular position measured from this point, it decreases continuously, and ultimately and at a certain maximum angle, the impaction efficiency becomes zero. In addition, the particle velocity upon impaction and the impaction angle may vary with angular position. In the work of Rosner and Tandon [95], a correlation has been proposed to model the impaction efficiency involving the effect of angular position. The correlation is partly based on the work of Wessel and Righi [123]. Hence, the impaction efficiency depending on the angular position (η_p) can
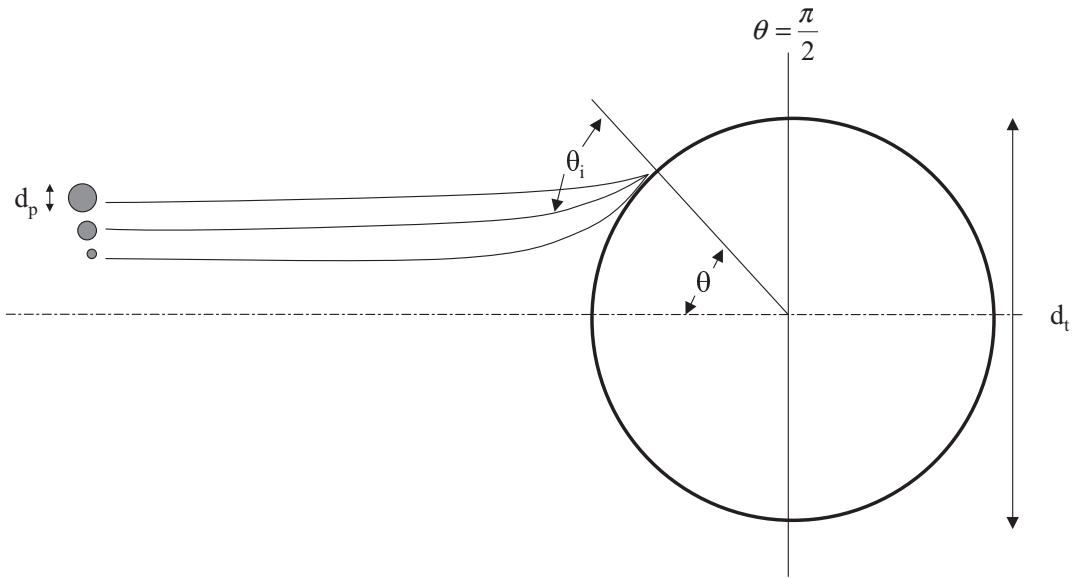
Figure 3.10: Schematic illustration of the effect of angular position on the impaction efficiency [51].

be expressed as the function of the impaction efficiency from Equation 3.48 and the maximum angular position (θ_{max}) at which inertial impaction occurs using a cosinusoidal relationship:

$$\eta_p (Stk, \theta) = \frac{\pi}{2} \frac{\eta_p (Stk)}{\theta_{max}} \, cos \left(\frac{\pi}{2} \frac{\theta}{\theta_{max}} \right) \tag{3.49}$$

where θ is the angular position measured from the stagnation point. The maximum angular position is calculated based on the following correlation:

$$\frac{\theta_{max}}{\pi/2} = \begin{cases} b \, ln \, (8Stk) + c \, (Stk - a) + d \, (Stk - a)^2, & 0.125 < Stk < 0.5 \\ \left[1 + b \, (Stk - a)^{-1} - c \, (Stk - a)^{-2} + d \, (Stk - a)^{-3} \right]^{-1}, & 0.5 < Stk \end{cases} \tag{3.50}$$

The coefficients in Equation 3.50 can be obtained from the following table.

Table 3.4: Coefficients for equation 3.50

Stk range	a	b	c	d
0.125 - 0.5	0.125	0.696596	-1.822407	1.1452745
greater than 0.5	0.125	0.7722744	0.271871	0.06049905

3.3.3 Eddy Impaction

As reported in literature [64, 111], eddy impaction is relevant only for small particles. In general, small particles have not enough momentum to deposit via inertial impaction. However, the

eddies may add momentum to the particles which are entrained in turbulent eddies and disrupt steady streamlines to impact on the tube surfaces. The deposition by eddy impaction is less understood than the deposition mechanism in the previous section because of the difficulty in describing the turbulent eddies. Most of the models in the literature describing this phenomenon are related to empirical correlations. One of the empirical models was proposed by Muyshondt [70]. This correlation has been used to model turbulent deposition in the furnace of a utility boiler [90]. In the model, the dimensionless deposition velocity ($u_{d,turb}^+$) is expressed as the function of Reynolds number (Re) as follows:

$$u_{d,turb}^+ = a_1 \, exp\left[-0.5\left(\frac{Re - a_2}{a_3}\right)^2\right] + a_4 \, exp\left[-0.5\left(\frac{ln\left(\tau^+\right) - ln\left(a_5\right)}{a_6}\right)^2\right] \tag{3.51}$$

where τ^+ is the relaxation time of the particle which can be obtained from the following correlation:

$$\tau^+ = \frac{1}{18}C_{Cun}\frac{\varrho_p}{\varrho_g}d^{+2} \ \ with \ \ d^+ = \frac{d_p \, u_\tau}{\nu_g} \tag{3.52}$$

In Equation 3.52, C_{Cun}, ϱ_p, ϱ_g, d^+, d_p, u_τ, ν_g represent the Cunningham correction, the particle density, the gas density, the dimensionless particle diameter, the particle diameter, the shear velocity, and the gas kinematic viscosity, respectively. The Cunningham correction and the shear velocity can be calculated based on the following equations:

$$u_\tau = \sqrt{\frac{\mu_g \, u}{L \, \varrho_g}} \tag{3.53}$$

$$C_{Cun} = 1 + Kn\left(1.155 + 0.471\right) + exp\left(-0.596/Kn\right) \tag{3.54}$$

where μ_g, u, L, Kn are the dynamic gas viscosity, the gas velocity, the characteristic length, and the Knudsen number. All constants ($a_1 - a_6$) in Equation 3.51 were determined experimentally by Muyshondt [70]. The constants are reported to have the following values: $a_1 = 2.26 \times 10^{-2}$, $a_2 = 4.03 \times 10^4$, $a_3 = 1.533 \times 10^4$, $a_4 = 0.1394$, $a_5 = 49.0$, $a_6 = 1.136$. Hence, the deposition velocity as the function of the dimensionless deposition velocity is expressed as:

$$u_{d,turb} = u_{d,turb}^+ \cdot u_\tau \tag{3.55}$$

The deposition rate may be expressed based on the 2-step method proposed by Pyykoenen [82] as follows:

$$\dot{m}_{dep} = C_p \, u_{d,turb} \tag{3.56}$$

where C_p is the particle concentration near to the wall. Another deposition model by eddy impaction considering the effect of roughness of the deposit surface has been proposed by Fan and Ahmadi [26].

3.3.4 Thermophoresis

Thermophoresis is the process of particle motion which is influenced by a local temperature gradient. Thermophoretic force on a particle may be induced either by a gas phase temperature gradient or by a temperature gradient in the particle itself [6]. The high temperature gas molecules on the hot portion of the particle have a higher collision frequency and energy than those on the low temperature portion. As the consequence, the pressure on the high temperature part will be higher than that on the low temperature part. This causes a net force in the direction of low temperatures. The thermophoretic force decreases as the deposit grows, because the deposit accumulation on the tube surface decreases the temperature gradient in the thermal boundary layer. Talbot has made an investigation about the existing thermophoresis models [110]. Furthermore, he proposed a correlation to calculate the deposition velocity $(u_{d,Th}^+)$ which is valid in the whole range of Knudsen number $(0 \leqslant Kn \leqslant \infty)$:

$$u_{d,Th}^+ = \frac{2\, C_s\, \nu \left(\frac{K_g}{K_p} + C_t\, Kn \right) \left[1 + Kn \left(A + B\, exp\left(\frac{-C}{Kn} \right) \right) \right] \frac{\Delta T}{T_0}}{(1 + 3\, C_m\, Kn) \left(1 + 2\frac{K_g}{K_p} + 2\, C_t\, Kn \right)} \tag{3.57}$$

where ν, Kn, ΔT, $\frac{K_g}{K_p}$ are the gas kinematic viscosity, the Knudsen number, the difference between the gas and the deposit surface temperature, and the ratio of gas thermal conductivity to particle thermal conductivity. The ratio is difficult to determine because it strongly depends on the structure of the particle. Typical values for this ratio range from 0.02 to 0.03 [90]. In Equation 3.57, C_s, C_t, C_m, A, B, C are the model constants which have the following values: $C_s = 1.17$, $C_t = 2.18$, $C_m = 1.14$, $A = 1.20$, $B = 0.41$, $C = 0.88$. The Knudsen number is dependent on the particle diameter (d_p) and the thermodynamic state of gas and may be obtained from the following equations:

$$Kn = \frac{2\bar{\lambda}}{d_p} \quad where \quad \bar{\lambda} = \frac{2\,\nu}{\bar{c}} \quad and \quad \bar{c} = \sqrt{\frac{8\, \Re\, T_g}{\pi\, M_{M_{mix}}}} \tag{3.58}$$

where $\Re$, $\bar{\lambda}$, T_g, and $M_{M_{mix}}$ represent the universal gas constant, the wavelength, the gas temperature, and the molar mass of the gas mixture, respectively. Then, the deposition velocity and the mass deposition rate are calculated in the same way as described in Section 3.3.3.

3.3.5 Ash Deposition Mechanisms on the Superheater [This Work]

In the model, three deposition mechanisms: inertial impaction, eddy impaction, and thermophoresis are considered. The following table gives an overview of the model which is applied depending on geometry and particle size. The model has been used to predict the growth of deposit layer inside the furnace of utility boilers and its effect on the heat transfer degradation.

Table 3.5: The implemented deposition mechanisms depending on geometry and particle size [90]

Mechanism	Water Wall Fine Particles	Water Wall Coarse Particles	Tube Geometry Fine Particles	Tube Geometry Coarse Particles
Inertial Impaction		✓		✓
Eddy Impaction	✓	✓		
Thermophoresis	✓		✓	

The implemented model is used as the framework to develop AIOLOS concerning ash deposition mechanisms. Furthermore, the condensation model described in the previous section has been included as an additional mechanism because it is believed to have a significant contribution to the formation of initial deposit layer in the furnace.

The present work has been focused on the deposit build-up on the superheater tubes. Two major contributors responsible for deposit formation in this part are inertial impaction and condensation [64]. However, there is a possibility that some particles may arrive and stick on the water wall before reaching the superheater tubes. The model implemented by Richter [90] is used to accommodate this effect. The particle arrival rate on the water wall is calculated by means of Lagrangian approach, considering the influence of fluid turbulence by a stochastic model (see section 2.7). An additional variable, C_{ndep} is introduced in the model. This variable having the initial value of 1 represents the undeposited particle cloud which is calculated at each trajectory especially when the particle cloud arrives at the deposit layer. Based on the 2-step method proposed by Pyykoenen [82], this variable can be expressed as follows:

$$C_{ndep,2} = C_{ndep,1} \left(1 - f_{Trans} \, f_{stick} \right) \tag{3.59}$$

where $C_{ndep,2}$ is the undeposited particle cloud as the function of $C_{ndep,1}$, the part of the particle cloud which enters a cell near to the wall cell. In the equation, f_{Trans} and f_{Stick} represent the impaction efficiency and the sticking probability. A detailed discussion about the sticking probability will be made in section 3.4. In case all of the particle cloud is deposited on the surface, $C_{ndep,2}$ is equal to 0. The impaction efficiency, f_{Trans}, on the superheater tubes is calculated based on the model which is described in section 3.3.2, whereas this value is assumed to be 1 in case of inertial impaction on the water wall. Furthermore, the deposition rate on the superheater tubes is governed by the deposition rate by inertial impaction (Section 3.3.2) and the condensation rate (Section 3.3.1):

$$\frac{dm_{dep}}{dt} = I \cdot f_{stick} + C \tag{3.60}$$

where I and C are the impaction rate and the condensation rate.

3.4 Ash Sticking Probability

In the previous section, the fundamental mechanisms describing the particle transport to the heat transfer surfaces in furnaces were presented. However, not all arriving particles will stick on the surface. They may stay at the surface to build a new deposit layer or bounce causing erosion of the surface. Hence, the adhesion propensity requires also special attention in order to predict the formation of a deposit layer. In terms of deposit layer formation, it should be distinguished between the short term and the long term deposit build-up. The former one refers to the condition directly after the contact with the surface, the particles will either bounce or stay on the surface at least for a very short period of time. The latter one is related to the behaviour of a deposit layer after relatively long periods of time including sintering, chemical reaction, erosion and change of the thermal properties of the layer. Modelling the short-term deposit formation will be described in the actual section.

The general phenomenon of the sticking probability of a particle impacting on a surface has been investigated by several researchers [116, 117]. The viscosity of the ash particle can be used as a parameter determining the stickiness of the particle on the heat transfer surface. It has been identified that the following conditions may occur inside the furnace:

- High viscosity of particles/deposit surface leads to the particle rebound on impact, without sticking.

- Low viscosity of particles/deposit surface leads to the sticking of the particles on the surface due to the dissipation of kinetic energy, plastic deformation and adhesion of the particles.

- Very low viscosity of the particles leads to the flowing of the particles on the surface due to the complete deformation of the particles.

It has been also observed in real furnaces that the existence of a film layer with very low viscosity either on the impacting particles or on the deposit surface influences the sticking probability of the particles on the surfaces. The film layer may be formed by the condensible species or the melted ash particle, and some of the kinetic energy of the particle will be lost on impaction due to effective energy dissipation. A positive correlation is observed between the sticking probability of particles and the layer thickness [39]. In general, there are several forces which play a predominant role concerning the interaction between the particles and the deposit surface. A model of such interaction can be found in [90].

For modelling purposes, there are various applicable methods to quantify the adhesion propensity of fly ash particles, e.g., ash fusion temperature, empirically derived viscosity models, information from phase-diagrams and equilibrium calculations, or experimentally determined ash capture efficiencies generated in lab-scale combustors. None of the methods is superior in

all aspects of relevance and their performance strongly depends on the specific case of application. In case of a lignite-fired utility boiler, a method based on the viscosity models has been developed and discussed in [90]. This work utilizes a melt fraction approach to calculate the sticking probability when considering the deposit formation in biomass co-fired boilers.

3.4.1 Ash sticking probability for coal-fired boiler with biomass co-combustion [This Work]

Condensation of potassium vapor may be the dominant mechanism at the initial stage of deposit formation for the biomass co-firing systems as well as for the biomass-fired boilers. The condensible potassium species at the deposit and particle surfaces efficiently capture the silica-rich particles. This was observed in the work of Nielsen [73]. Hence, Hansen [39] suggested that the sticking probability is proportional to the fraction of melt at the surface. In the present work the melt fraction based sticking concept developed by Kaer [51] was implemented into AIOLOS. The net fraction of arriving particles contributing to deposit growth (f_{stick}) is obtained following a concept proposed by Walsh [119]. This concept considers incoming sticky particles depositing on sticky or non-sticky surfaces as well as incoming non-sticky particles depositing on sticky surfaces. These considerations are written in the following equation:

$$
\begin{aligned}
f_{stick} = {} & P_{stick}\left(T_p\right) + \left[1 - P_{stick}\left(T_p\right)\right] P_{stick}\left(T_s\right) \\
& - k_{Ersn}\left[1 - P_{stick}\left(T_p\right)\right]\left[1 - P_{stick}\left(T_s\right)\right]
\end{aligned}
\tag{3.61}
$$

where k_{Ersn}, T_p, and T_s denote the erosivity of impacting ash particles towards the deposit, the particle temperature, and the deposit surface temperature, respectively. The erosion coefficient depending on the impact energy of the particles as well as the ash composition can be determined experimentally [90]. In this work, the effect of erosion is not considered to predict the deposit formation. Thus, a sticking criterion based on melt fraction (f_{melt}) can be expressed as follows [51]:

$$
\begin{aligned}
& f_{melt} < 10\% \text{ mass of molten phase} : \rightarrow \text{non-sticky} \\
& 10\% < f_{melt} < 70\% \text{ mass of molten phase} :\rightarrow \text{sticky} \\
& f_{melt} > 70\% \text{ mass of molten phase} : \rightarrow \text{flowing}
\end{aligned}
\tag{3.62}
$$

Based on this expression, a correlation between the sticking probability and the melt fraction can be obtained as illustrated in figure 3.11. In order to obtain the sticking probability of the impacting particles and that of the surface, the melt fraction of the particles as well as the surface is required. In case of biomass fired boilers, two types of ash are considered, potassium salt and silica-rich particles. Potassium salt is the major species released in the gas
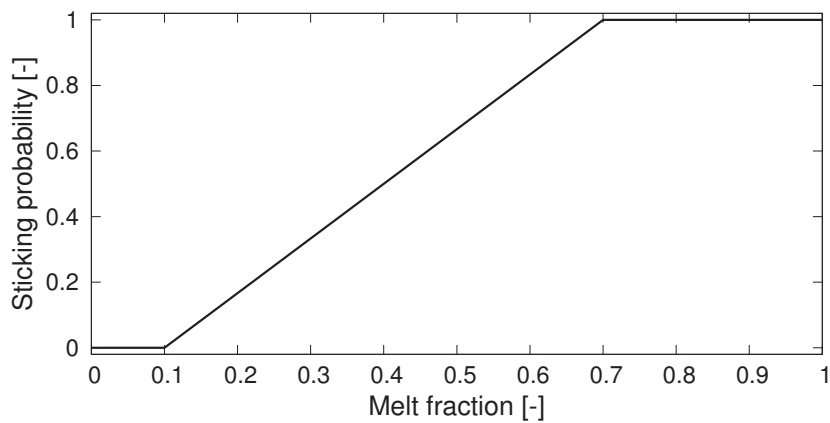
Figure 3.11: Sticking probability related to the melt fraction. Adopted from Kaer [51].

phase especially in straw fired furnaces (section 3.2.2), and has a significant contribution to the deposit formation via condensation (see section 3.3.1). In addition, silica-rich particles are the major ash particles in respect to the deposit formation [51]. Thus, the melt fractions can be estimated as a function of local temperature and composition (indicated by T and X) as follows:

$$f_{melt}(T, X) = f_{melt,KCl}(T) \frac{m_{KCl}}{m_{total}} + f_{melt,silicate}(T) \frac{m_{silicate}}{m_{total}} \tag{3.63}$$

Melt fraction of KCl ($f_{melt,KCl}$) and that of silica particles ($f_{melt,silicate}$) are related to the temperature and calculated based on figure 3.12. The melting curves in this figure are estimated
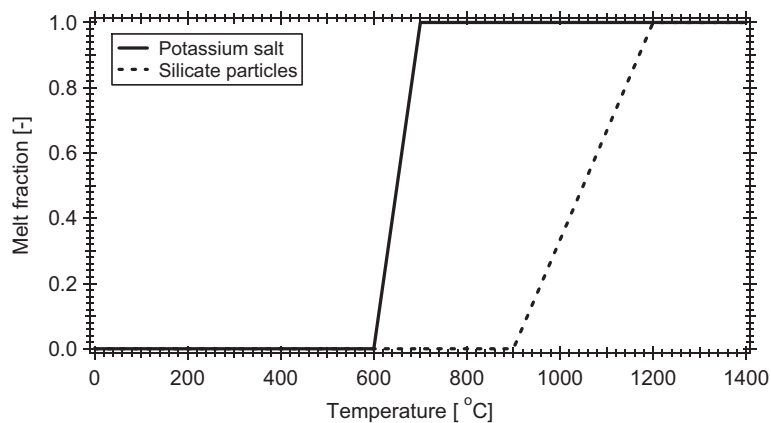
Figure 3.12: Approximated melting curves of potassium salt and silicate particles. Adopted from Kaer [51].

from the measured melting curves of ashes performed by Hansen [39] for straw-fired boilers. In general, this concept is also applicable to describe the sticking probability of ash particles in

case of a co-firing system with the difference on the species under investigation. In addition, this work also uses straw as the type of biomass either in case of 100% biomass or in case of co-firing biomass with coal.

3.5 Thermal and Physical Properties of Deposit

Ash deposits reduce the process efficiency in a boiler due to the heat transfer degradation on the furnace walls, superheater tubes, and other heat transfer surfaces. In order to predict the reduction of heat transfer rates, the surface temperature of the water walls/tubes or the deposits has to be calculated. To estimate the surface temperature, the working fluid temperature, and heat transfer resistances (thermal conductivity and emissivity) of the tube material and the ash deposits must be known (see Fig. 3.13). The latter is not an easy task due to the difficulty in determining the local thickness and the physical structure of the deposits. The magnitude of the thermal conductivity is determined by the macro structure of the deposit, i.e., its porosity, degree of sintering, pore and particle size distribution. It has been identified that the deposit structure has the dominant effect [87]. Through the deposit ash, heat transfer by conduction
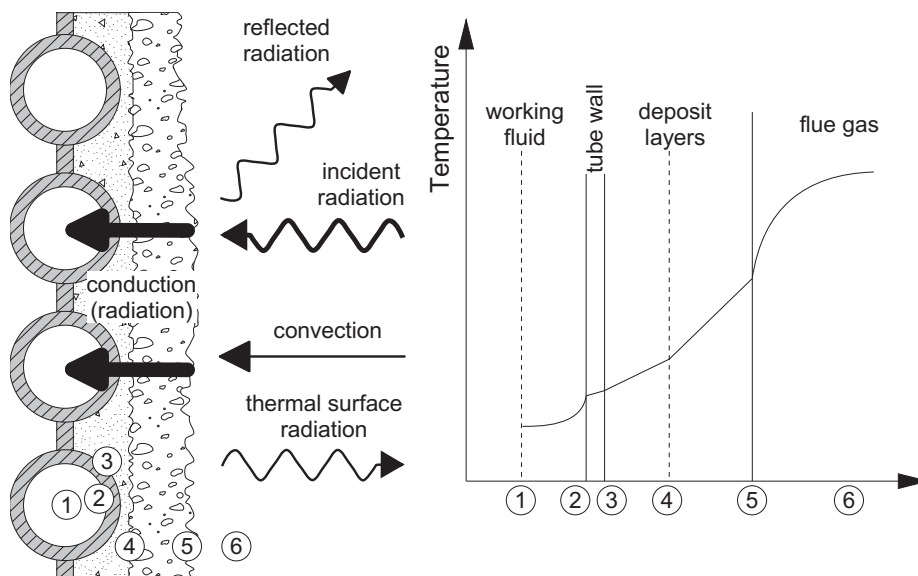
Figure 3.13: Schematic of the heat transfer mechanisms through deposits in the furnace region. Adopted from Schnell [99].

occurs through both, the solid and gas phase, and radiation occurs through the pores of the deposits. Thus, these heat transfer modes will contribute to the effective thermal conductivity. A correlation of Botterelli can be used to model this mechanism [12]. In addition, Gupta and Wall [35] propose a model that takes into account both conductive and radiative heat transfer since both mechanisms occur in parallel. However, radiation has a significant effect only if large pores and high temperature coincide in the deposits [99].

3.5.1 Deposit Thermal Conductivity

Values for the thermal conductivity of the gas- and solid-phase material are needed to give a first impression about the importance of porosity for calculating the effective thermal conductivity. A value of 0.06 $Wm^{-1}K^{-1}$ is used for the thermal conductivity of gas, which is comparable to the thermal conductivity of air at typical deposit temperatures, whereas a value of 3 $Wm^{-1}K^{-1}$ is used for solid material, which is representative of the thermal conductivity of silica containing material at high temperature. According to those values, the effective thermal conductivity is in the range of 0.06 - 3 $Wm^{-1}K^{-1}$ for different values of deposit porosity. However, deposit porosity is not the only important parameter to determine the effective thermal conductivity. An additional structure parameter, the degree of sintering, must be also considered as illustrated theoretically as follows.

Firstly, two combinations of the thermal conductivity of two materials (solid and gas) are introduced, one for a parallel combination (Fig. 3.14a) and the other for a series combination (Fig. 3.14b). The effective thermal conductivity for those combinations can be written as:
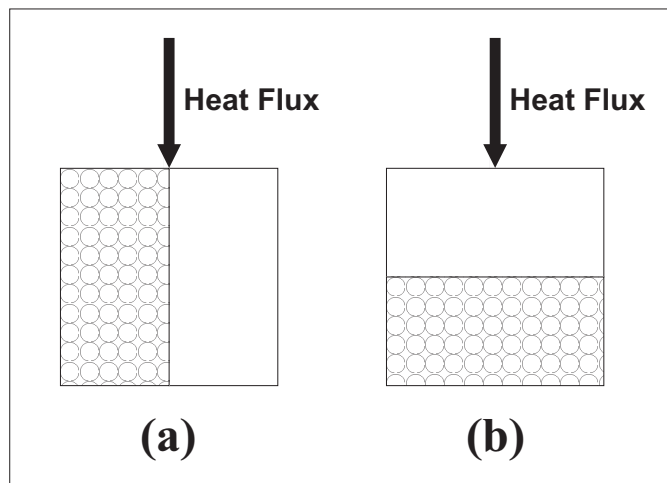
Figure 3.14: Two deposits with similar porosity (0.5) but significantly different in thermal conductivity [7]. (a) parallel combination, (b) sequential combination.

$$K_{parallel} = \phi_{deposit}K_g + (1 - \phi_{deposit})K_{solid} \left[Wm^{-1}K^{-1}\right]$$
$$K_{series} = \frac{K_gK_{solid}}{(1 - \phi_{deposit})K_g + \phi_{deposit}K_{solid}} \left[Wm^{-1}K^{-1}\right] \tag{3.64}$$

where K and ϕ denote the effective thermal conductivity and the porosity, respectively. Fig. 3.14 shows qualitatively two extreme cases having similar porosities (around 0.5). However, the theoretical analysis (Fig. 3.15) shows a significant difference in the effective thermal conductivity for the deposits. From the practical point of view, those thermal conductivities do not exist. On the other hand porosities of deposits found in coal-fired furnaces are in the range of
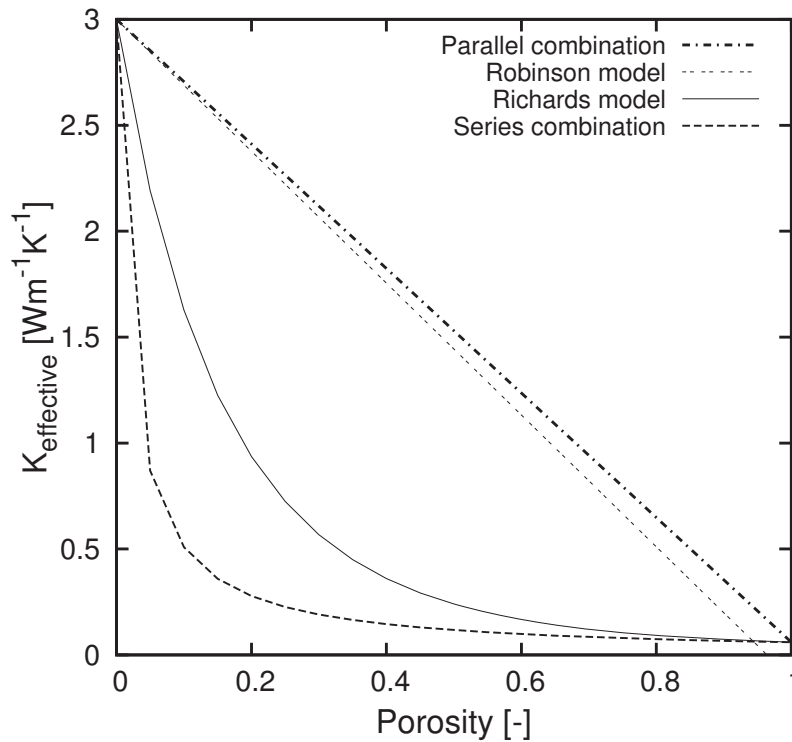
Figure 3.15: The effective thermal conductivity calculated by various models. Adapted from [90].

0.2 to 0.8 [99]. This range is reported when considering slagging and fouling in a utility boiler. In addition, the two values calculated from the parallel and series combinations can be regarded as an upper theoretical limit (dashed-dot line) and a lower theoretical limit (dashed line) of the thermal conductivity, respectively. Two additional models are shown also in the figure, one is proposed by Richards [89], and the other by Robinson [93]. Based on Richards model, the thermal conductivity is calculated by the following equation:

$$K_{effective} = (1 - F) \ K_{solid} + F \ K_g \tag{3.65}$$

where F is the fraction of the conductivity attributed to the gas which is calculated as a function of porosity ϕ as follows:

$$F = \frac{2^n}{2^n - 1} \left(1 - \frac{1}{(1 + \phi)^n} \right) \tag{3.66}$$

In equation 3.66 n is an empirical parameter, and has a value of 6.5 [89]. From Fig. 3.15, it can be seen that the conductivity lies above the lower theoretical limit of the thermal conductivity. Another correlation between the conductivity and the porosity is based on an experimental study performed by Robinson [93]. The correlation lies slightly under the upper theoretical limit of the conductivity. It is obvious that there is a big difference in the results of the two

models. It can be assumed that there was a difference in the sintering degree of the deposits under investigation when performing their experiments to derive the models.

In this work, a model proposed by Brailsford and Major [13] is used to approximate the thermal conductivity of ash deposits. The model considers not only the porosity of deposits but also the sintering degree. The following equation can be used to calculate the thermal conductivity for the powdery deposit as well as for the sintered deposit:

$$K_{sintered/powdery} = \frac{K_{cont} \left[\omega \, \vartheta_{discr}^{2/3} + \left(1 - \vartheta_{discr}^{2/3} \right) \right]}{\left[\omega \left(\vartheta_{discr}^{2/3} - \vartheta_{discr} \right) + \left(1 - \vartheta_{discr}^{2/3} + \vartheta_{discr} \right) \right]} \tag{3.67}$$

The basic concept of the model assumes that the ash deposit can be differentiated into a continuous phase and a discrete phase. In case of sintered deposit, the discrete phase is represented by the gaseous part of the deposit, whereas the continuous phase is represented by the solid part of the deposit,

$$K_{cont} = K_{solid} \qquad K_{discr} = K_g \qquad \vartheta_{discr} = \phi \qquad \omega = \frac{K_g}{K_{solid}}. \tag{3.68}$$

On the contrary, in the case of powdery deposit, the solid part represents the discrete phase, whereas the gaseous part represents the continuous phase in case of powdery deposit,

$$K_{cont} = K_g \qquad K_{discr} = K_{solid} \qquad \vartheta_{discr} = 1 - \phi \qquad \omega = \frac{K_{solid}}{K_g}. \tag{3.69}$$

In Fig. 3.16, the effective thermal conductivity is calculated by using equation 3.67 for the two cases, sintered and powdery deposit. In real applications, such extreme values of the thermal conductivity are usually not found since even a liquid slag layer may still have some gaseous pores. In case of mixed deposit, another model was proposed by Brailsford and Major:

$$K_{mix} = \frac{K_{sintered}}{4} \left[A + \sqrt{\left(A^2 + 8 \, \frac{K_{powdery}}{K_{sintered}} \right)} \right], \tag{3.70}$$

where A is calculated by the following equation:

$$A = \left(3 \, V_{powdery}^* - 1 \right) \frac{K_{powdery}}{K_{sintered}} + \left(3 \, V_{sintered}^* - 1 \right) \tag{3.71}$$

Here, $V_{powdery}^*$ and $V_{sintered}^*$ refer to the volume fraction of powdery deposit and of sintered deposit, respectively. The deposit structure (in respect to the degree of sintering) and the porosity are not decoupled from each other [99]. It seems that the deposit has a molten, highly sintered consistency whereas in the case of a higher porosity, a structure with a lower degree of sintering exists. To take into account these phenomena, Brailsford and Major proposed the
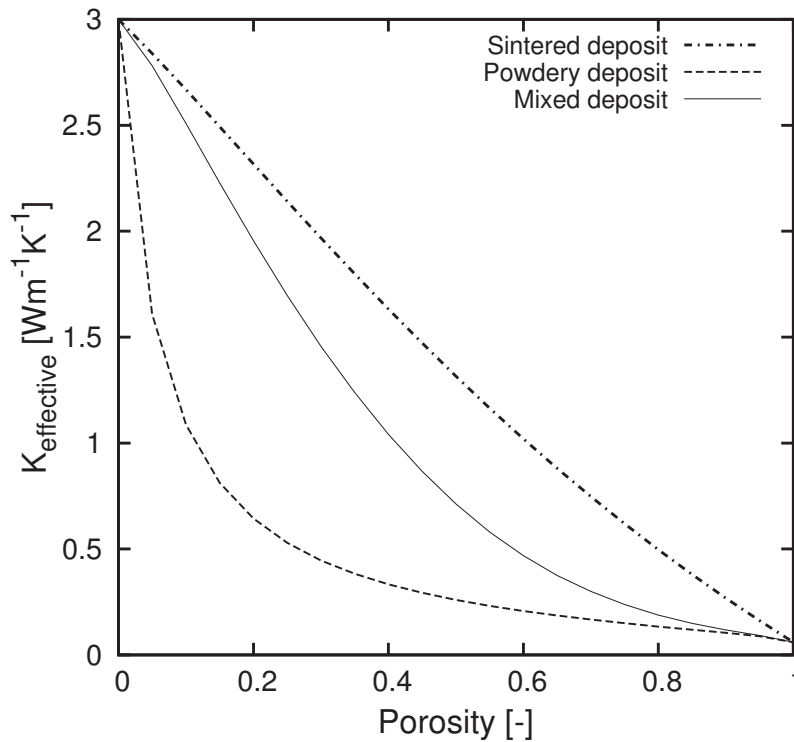
Figure 3.16: Effective thermal conductivity based on the model proposed by Brailsford and Major [13]. The thermal conductivity is calculated at 600 $^\circ C$.

following correlation as a relation between the volume fraction of powdery deposit and the porosity:

$$V^*_{powdery} = \phi\left[\alpha + (1 - \alpha)\phi\right], \; where \quad \alpha = 0.8 \tag{3.72}$$

Furthermore, the calculated thermal conductivities based on equation 3.70 are also shown in Fig. 3.16. From the figure, it can be seen that the effective thermal conductivity of the mixed structure with a high porosity comes close to the curve for powdery deposit, whereas at a lower porosity, it approaches the highly sintered deposit.

Chemical composition and temperature are the additional variables which have an effect on the effective thermal conductivity. However, the published results are not consistent in respect to these issues [118]. These inconsistencies are not surprising since these parameters may both directly and indirectly affect deposit thermal conductivity. The composition directly influences the thermal conductivity due to the variation in the thermo-physical properties for different deposit materials. Indirect effect of the composition on the thermal conductivity may be due to its influence on the degree of sintering. This effect is likely more significant than the direct one [90]. Similar to the chemical composition, temperature may directly influence the deposit conductivity. The deposit may contain amorphous as well as mineral phase with a great difference in the temperature behaviour. Due to lack of experimental data, it is difficult

to describe this behaviour concerning its effect on the thermal conductivity. Based on the difficulties, a constant value of 3 $W m^{-1} K^{-1}$ is chosen in this work for the conductivity of solid material, similar to the value used by several research groups, for example Gupta [36], Kaer [51] and Richards [89]. This is the typical value of material containing SiO_2 and Al_2O_3 at high temperature [112, 113]. Thus, the thermal conductivity of the gas phase is calculated as a function of temperature, written by [97]:

$$K_g = 0.0243 \left(\frac{T}{273.15} \right)^{0.82} \tag{3.73}$$

During deposit build-up, several layers may be formed which are different to each other in porosity and degree of sintering. A layered deposit has been found on the heat transfer surface of a straw fired boiler as well as on that of a big utility boiler [73, 84]. In order to describe these phenomena, the following equation can be used to calculate the effective thermal conductivity of a layered deposit as the function of the conductivity from individual layers:

$$\frac{K_{effective}}{L_{tot}} = \sum_{i}^{n} \frac{K_{effective,i}}{L_i} \tag{3.74}$$

where $K_{effective,i}$ and L_i denote the thermal conductivity and the thickness of layer i. If the steam tube temperature and the flux ($\dot{q}$) at the deposit surface are known, the surface temperature can be calculated by the following equation:

$$T_s = \dot{q} \cdot \frac{L_{tot}}{K_{effective}} + T_{tube}, \tag{3.75}$$

whereas the thickness of layer i (L_i) is calculated as follows:

$$L_i = \frac{\dot{m}_{dep} \, \Delta t_i}{\rho_{dep} \, (1 - \phi_i)} \tag{3.76}$$

where $\dot{m}_{dep}$ and Δt_i represent the deposition rate and the time interval, respectively.

3.5.2 Radiative Properties

An additional mechanism, radiation, may have a significant influence on the effective thermal conductivity. In terms of radiation, it can be distinguished between the radiation through a solid transparent medium and the radiation through pores. The former mechanism is inherent in determination of the thermal conductivity in section 3.5.1 due to the difficulty to avoid this effect during experiments. Furthermore, the major concern of this subsection is a brief description of the latter mechanism. The most important properties affecting the radiation through pores are the pore size and the porosity.

In the present work, a model proposed by Botterill et al. [12] is utilized to calculate the radiation effect on the effective thermal conductivity which can be written as:

$$K_{rad} = 4\,\sigma\,\chi\,d_{pores}\,T^3 \tag{3.77}$$

where σ, χ, d_{pores} and T are the Stefan-Boltzmann's constant, an exchange factor, the diameter of pores and the deposit temperature, respectively. The exchange factor is dependent on the porosity ϕ and the emissivity ε, which can be calculated based on either the Godbee and Ziegler model [32]:

$$\chi = \frac{\phi\varepsilon}{1-\phi}, \tag{3.78}$$

or the Laubitz model [58]:

$$\chi = \frac{1 - (1-\phi)^{2/3} + (1-\phi)^{4/3}}{1-\phi}\varepsilon. \tag{3.79}$$

By using emissivity of $\varepsilon = 1$, Botterill performed an evaluation of the model. However, a significant effect of temperature on the emissivities shown by the experimental results was not observed. Gupta has made a comparison between the thermal conductivities obtained from the model and the measured ones. In the experiments, the thermal conductivities were measured at temperatures of 100 $^\circ C$ and 450 $^\circ C$. It was found that the calculated conductivities at $\chi = 1$ are in good agreement with the measured ones. However, this exchange factor will be compatible only at low temperature conditions and at low porosity of deposit. On the other hand, the radiation through pores should have only small contribution at such low temperature conditions. If the emissivity ε is assumed to have a value 0.8, the porosity ϕ is 0.35 for $\chi = 1$. At higher porosity, it is clear that the exchange factor will be above that value.

After obtaining the conductivity related to the radiation through pores, the effective conductivity can be calculated as follows:

$$K_{effective,rad} = K_{effective} + K_{rad} \tag{3.80}$$

where $K_{effective,rad}$ is the thermal conductivity with the inclusion of radiation through pores and $K_{effective}$ is calculated based on the equations in section 3.5.1. Fig. 3.17 gives an illustration concerning the contribution of radiation through pores to the thermal conductivity for two temperature conditions. The dashed lines represent the thermal conductivity calculated by Equation 3.80 with the inclusion of the radiation effect. The solid lines are obtained by using Equation 3.70 assuming that the deposit structure is a mixed one. From the figure it can be seen that the radiation effect is relatively small at the lower porosities of deposit. The effect tends to be more significant at the higher porosities and at the higher temperatures. It can be
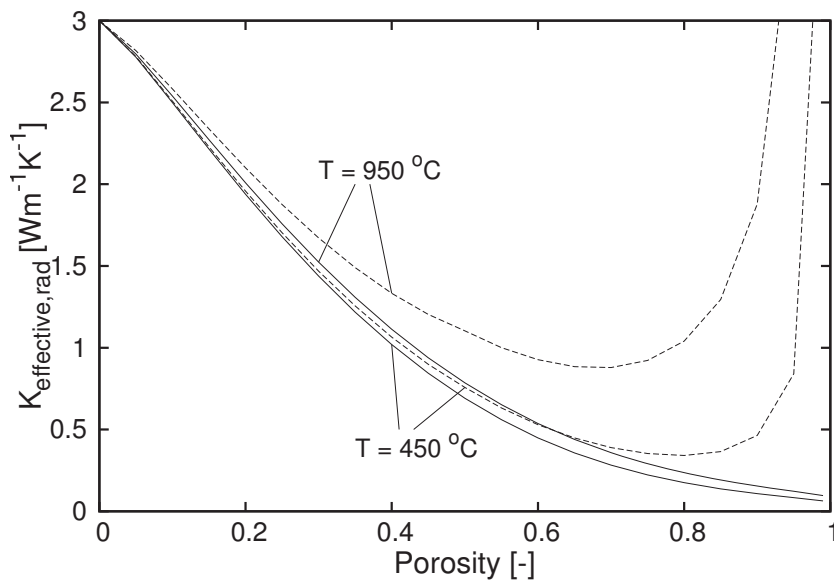
Figure 3.17: The effective thermal conductivity with the inclusion of radiation through pores (dashed lines) and without the inclusion of radiation through pores (continuous lines).

observed also that for all conditions, there is an extreme difference for the porosities starting from 0.8. However, this condition is rarely found in practical applications. Hence it can be concluded that the radiation will have a significant influence if the deposits with large pores and high temperature are considered.

However, the optical properties (emissivity and absorptivity) for the radiative heat transfer to the deposit surface are more important compared to the radiation through pores. The optical properties and the conductivity of the deposit change continuously during growth depending on the instantaneous composition, physical state and structure. Wall et al. [118] present predicted trends for the absorptivity and conductivity coefficient as shown in Fig. 3.18.

Initially, the wall is clean, and the absorptivity for this condition is high, around 0.8 for an oxidized steel. The first deposit layer is from fine particles which are transported to the surface by thermophoresis. In this stage, the deposit absorptivity decreases to around 0.3. As the layer starts to collect larger particles, the absorptivity increases slightly to a value between 0.4 to 0.5. During development of this layer, the surface temperature increases until reaching a limit where fusion of the surface initiates, causing the absorptivity to increase to 0.9. However, this value can be reached only in an exceptional case. It seems that intermediate steady state indicated by the horizontal arrows is more likely to occur due to the periodical sootblowing in the furnaces. In AIOLOS, the deposit absorptivity is assumed to have a constant value between 0.6 and 0.8 as a realistic value under steady-state conditions. In terms of the conductivity coefficient, the tendency initially is similar to the absorptivity until at a certain point when the coarse ash starts to form deposit layer. Then, unlike the absorptivity, the conductivity
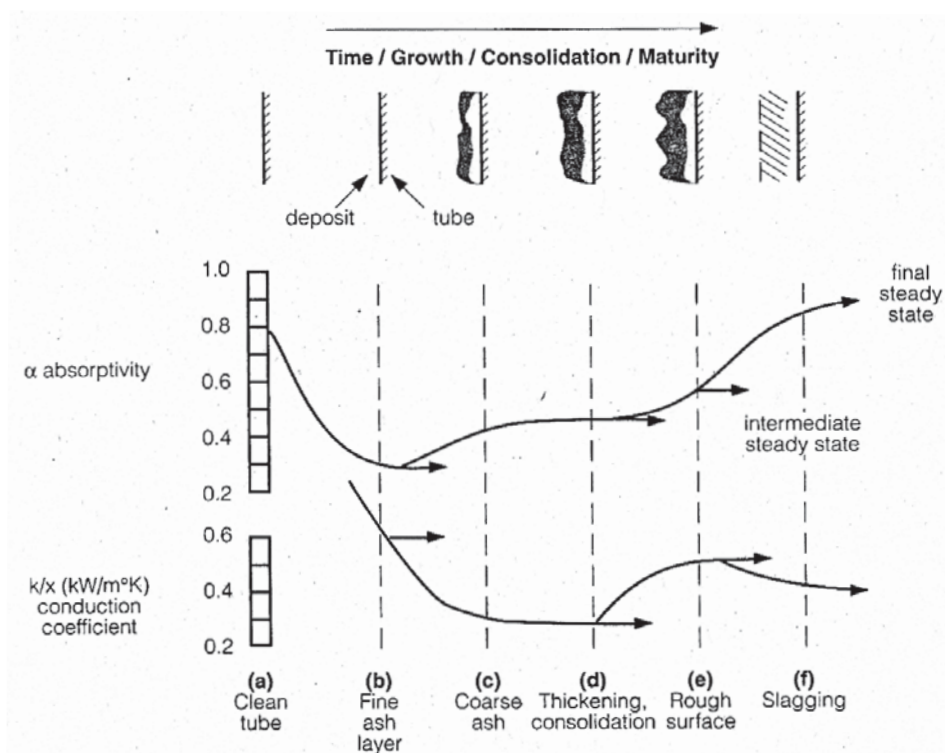
Figure 3.18: Evolution of deposit conductivity and absorptivity during deposit build-up. Adopted from Wall et al. [118].

coefficient will continue to decrease though at a lower rate. Afterwards, if the thickness of the deposit layer can compensate the increase of the effective conductivity due to the sintering degree, the conductivity coefficient will decrease, and vice versa.

An experimental investigation has been performed to determine the emissivity depending on the chemical composition of the deposit [34]. Two important results of the investigation are shown in Fig. 3.19. The figure shows the emissivities of two deposits, one with a high content of Fe_2O_3 (on the left hand side), and the other with a high content of $CaSO_4$ (on the right hand side). From the figure, it can be concluded that the emissivity is affected by the chemical composition and the deposit temperature. This observation is clearly shown in the case of deposits with a high content of $CaSO_4$.

On the other hand, a model proposed by Boow and Goard [11] can be used to calculate the emissivity of the deposit surface. In the model, the emissivity is related to the size of the deposited particles, written by:

$$\varepsilon_{total} = a \log d_p + b \tag{3.81}$$

where a and b are the coefficient and the constant depending on material, respectively. Based on the measurements for laboratory and furnace ashes made by the authors, the coefficient has a value of 0.30, whereas the constant has a value of 0.16. The particle sizes in the measurement
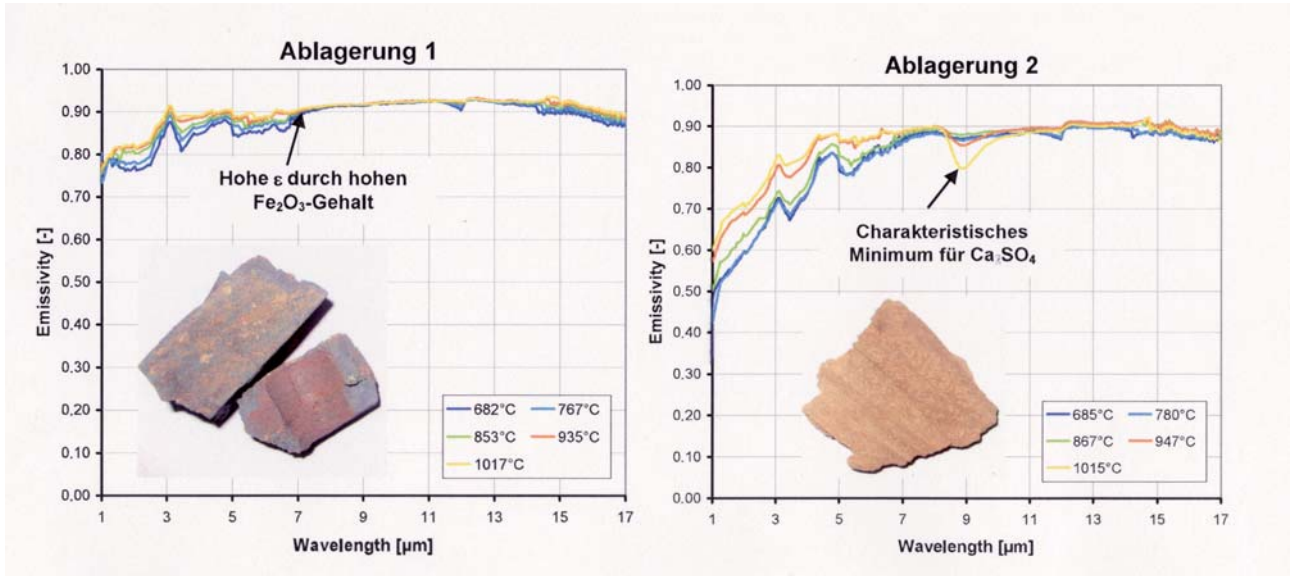
Figure 3.19: Spectral emissivities for two deposits. Adopted from Greffrath et al. [34]. Translations of the German words: Ablagerung = Deposit, Hohe ε durch hohen Fe$_2$O$_3$-Gehalt = High emissivity due to a high content of Fe$_2$O$_3$, Charakteristisches Minimum fuer CaSO$_4$ = Characteristic minimum for CaSO$_4$. *The misspelling of $CaSO_4$ in the original literature has been corrected.*

ranged from 7 μm to 420 μm. Fig. 3.20 shows the calculated emissivity based on the model. In addition, the emissivity of a transparent powder (colourless) is presented also in the figure, which is calculated using equation 3.81 with coefficient 0.25 and constant 0.13. It is obvious from the figure that the emissivity varies considerably at lower particle sizes. On the contrary, the increase of emissivity tends to be lower at bigger particle sizes (for example, from 30 μm to 140 μm). Furthermore, this observation may also be regarded as another evidence that the chemical composition has a significant influence on deposit surface emissivity. Ash particles and deposit surface undergo complex mineral transformation, whereas only several transformations are well understood [56]. Hence, equation 3.82 is used to calculate the emissivity for the typical ash deposit in a utility boiler [90]. It can be seen that the emissivity does not only depend on the particle size, but also on the surface temperature of deposits.

$$\varepsilon_{total} = 0.12 \log d_p + 0.44 + \left(2.10^{-7}T_s^2 - 6.10^{-4}T_s + 0.3\right)\left(\frac{300}{d_p}\right)^{0.14} \tag{3.82}$$

It should be noted that in equation 3.81 and 3.82 the surface temperature is in Kelvin, whereas the particle size is in μm. In Figure 3.20b, the emissivities calculated using Equation 3.82 for surface temperature of 675 K, 775 K, and 875 K have been also included. This shows that the emissivities are quite sensitive to the temperature. For the same particle size, the difference in emissivity is around 0.03 for a different surface temperature of 100 K. Qualitatively, the
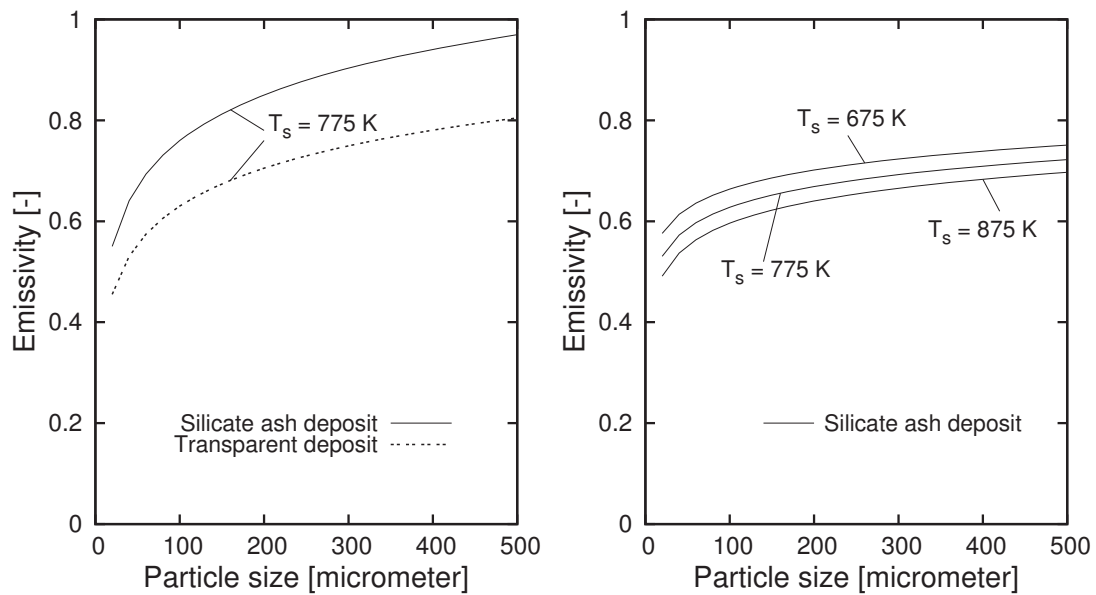
Figure 3.20: Emissivity of ash deposit, (a) calculated by equation 3.81 [11], and (b) calculated by equation 3.82.

calculated emissivities are in the similar trend compared to the Boow model though a significant difference in gradient regarding the increase of emissivity is clearly observed in the figure. In real furnaces, the surface temperatures may vary widely, and it is required to predict realistic optical properties to describe heat transfer through the deposit [109]. In addition, it has been shown also that the model (Equation 3.82) is in good agreement with the correlation proposed by Wall [118].

3.6 Simulation of the Alkali Release Effect on Deposition Mechanisms with AIOLOS

In the present work, a model predicting the release of alkali compounds and its effect on the deposition of superheaters has been developed. An overview of the model's functional modules with their individual purposes is given by the scheme in Fig. 3.21. Additional input data obtained from the elution analysis is required by the model. Firstly, a basic simulation is performed by AIOLOS supplying velocity, temperature and concentration of major flue gas species. In terms of alkali release, the heterogeneous reactions as well as the homogeneous reactions are considered in the respective alkali species, i.e. sodium and potassium. Modelling alkali release is integrated in the Eulerian frame, and its detailed explanation can be found in section 3.2. The basic simulation including the alkali release calculation is performed to obtain the free stream properties according to the probe location. Condensation models in

connection with the released alkali have been implemented to take into account the effect of alkali especially at the initial stage of the deposition process (section 3.3.1). Ash deposition processes are modeled in the Lagrangian frame and implemented in the post processing step. Various ash deposition mechanisms are described in section 3.3. To calculate the stickiness of arriving particles and surface, a melt approach described in section 3.4 is used. Afterwards, the deposit properties such as the deposit thickness and the deposit composition are updated after each time step supplying the input data for the next time step. As shown in the figure, there are two time frames denoted as inner time step and outer time step. The outer time step is required if the deposit formation greatly affects the distribution of the major variables such as temperature and velocity in the furnace.
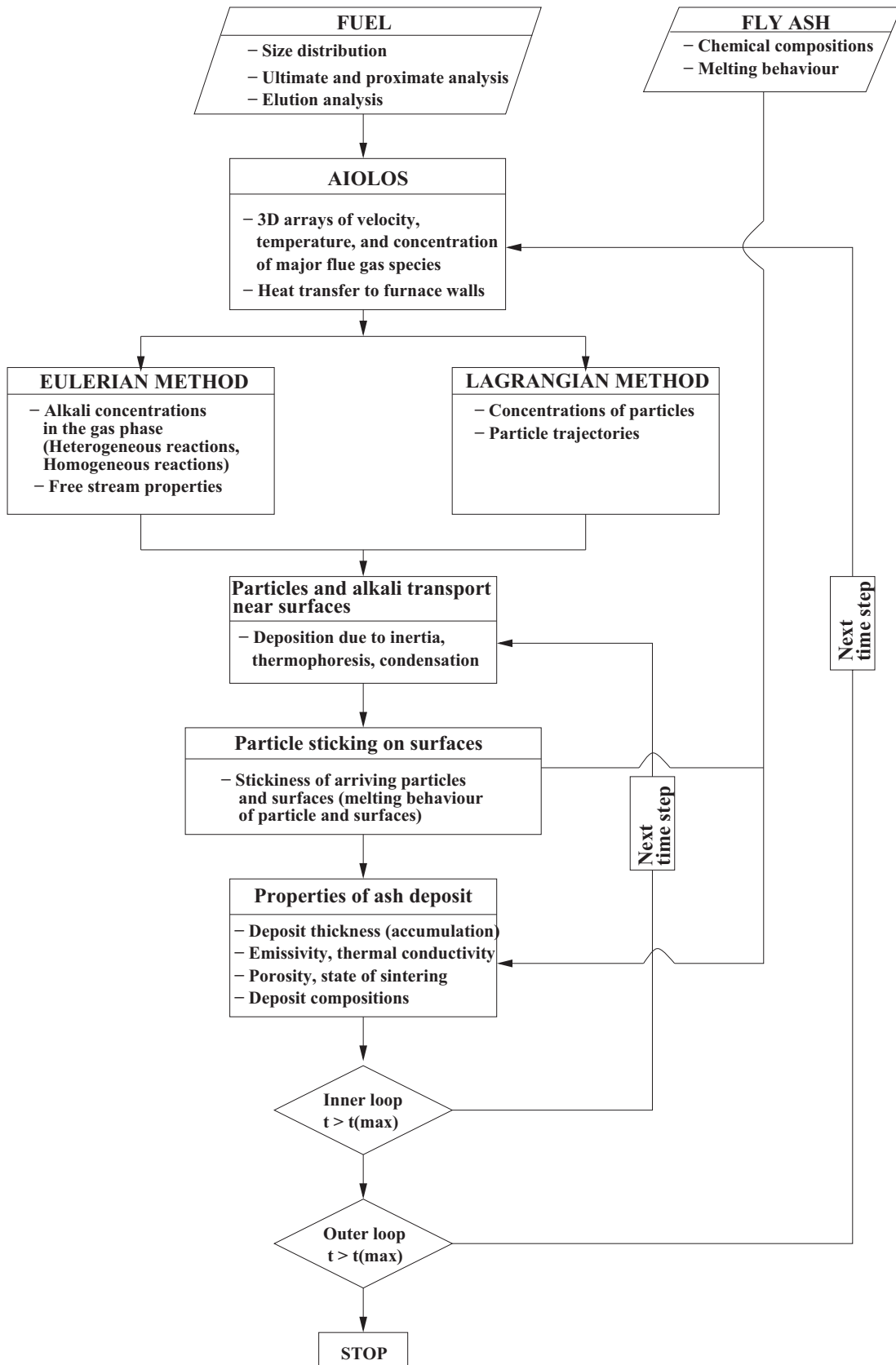
Figure 3.21: Flow chart illustrating the ash deposition and heat transfer prediction model.

4 Comprehensive Evaluation of the Model

4.1 Simulation of Alkali Release

In the present work, the numerical simulations and experiments are performed on a 20 kW_{th} entrained flow combustion reactor (EFCR). The reactor is electrically heated and subdivided into five regulated heating zones to maintain isothermal conditions over the whole reactor. The maximum temperature of the reactor is 1450 $°C$. Schematically, the reactor is shown in Figure 4.1. The ceramic reactor tube has a length of 2.5 m and an internal diameter of 200 mm. A
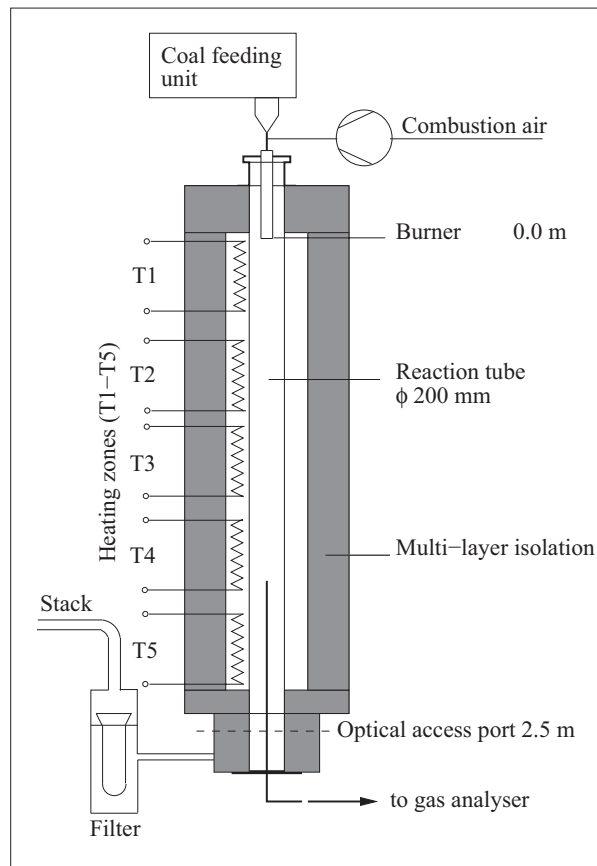
Figure 4.1: Scheme of the entrained flow combustion reactor (EFCR).

gravimetric screw conveyor supplies a constant coal-feeding rate in the range of 0.5 - 5 kg/h. The gas concentrations of O_2, CO_2, CO, NO_x and SO_2 can be measured at different positions along the reactor axis by extracting the gas samples using an oil-cooled gas probe. The gas phase alkali concentration was measured by using the excimer laser-induced fluorescence (ELIF) method. The measurement of the emitted alkali was done at the exit of the reactor. The ELIF method allows on-line and in-situ measurement of gas phase alkali concentrations [86].

4.1.1 Sodium release calculation

Experiments on the reactor have been conducted extensively to study the release of alkali in the gas phase [85]. Some of the experimental studies used a German bituminous coal, Ensdorf which was combusted with an air ratio of 1.15. The carrier air for the investigated case is set at a constant rate of 1.5 m^3/h. The temperature variations of the coal experiments ranged from 1100 $°C$ to 1400 $°C$. In this case, the residence time of the flue gas and particles in the ceramic tube is in the range of 4 s to 17 s. The coal mass flow and combustion air were adjusted, depending on the required residence time. In order to evaluate the model, two sets of experimental results which correspond to the residence times of 5 s and 7.5 s are compared with the simulation ones. In order to reduce computing time and considering the cylindrical reactor layout, 2D axial symmetry was assumed. Thus, a 2D cylindrical grid system with 37 radial and 427 axial cells was applied.

Table 4.1: The proximate, ultimate and ash analysis of the Ensdorf coal

Proximate analysis ($\%, raw$)							
Moisture	Volatile	Ash	Fixed C	LHV(MJ/kg)			
1.96	34.4	7.08	56.57	29.94			
Ultimate analysis ($\%, daf$)							
C	H	N	S	Cl	O (Rest)		
75.43	5.06	0.82	1.64	0.43	16.62		
Ash analysis ($mg/g_{coal,dry}$)							
Na_2O	K_2O	CaO	MgO	SiO_2	Al_2O_3	Fe_2O_3	SO_3
0.78	1.48	8.46	1.82	33.94	11.03	10.7	41.0

The coal analysis is given in Table 4.1, whereas the 4-step elution analysis (1st step: ionized water, 2nd + 3rd step 1M Ammoniumacetat (AAc), 4th step 1M HCl) illustrating the forms of every element in the coal is shown in Table 4.2. Based on the ash analysis, it can be observed that the potassium content is higher than the sodium content. However, it can be expected that most of the potassium content will remain solid at typical coal combustion temperatures because of its high affinity to aluminosilicate in the coal. Looking into the elution analysis in

Table 4.2: The elution analysis of the Ensdorf coal

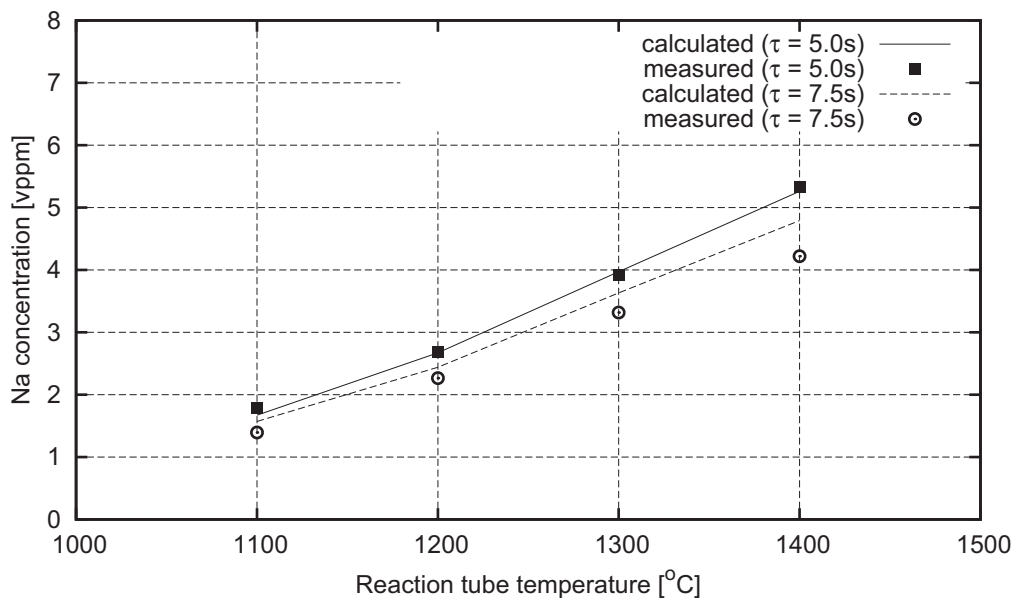| % raw coal	H_2O	AAc	HCl	Σ [%]
Na	29.2	2.47	5.07	36.73
K	1.75	0.69	1.52	3.96
Ca	13.62	69.18	2.34	85.14
Mg	13.74	48.28	14.27	76.29
Fe	0.0	0.0	54.26	54.26
Al	0.015	0.016	7.47	7.5

Figure 4.2: Flue gas Na concentration vs temperature for the combustion of Ensdorf coal.

more detail, it can be seen that 80% of the soluble sodium (36.73% of sodium in the raw coal) is in the form of water soluble one. The rest of sodium is assumed to be in the form of silica based sodium. The ratio of water soluble sodium and chlorine is lower than 1. In this case, chlorine is present over-stoichiometrically in the combustion process, and chlorination of alkali species is favored [103].

Fig. 4.2 shows the sodium release as the function of reaction tube temperature for two residence times. For the residence time of 5 s, the simulation result matches well with the experimental one. However, a slight discrepancy can be observed for the residence time of 7.5 s. The sodium release into the gas phase is over-predicted for the higher residence time. This can be attributed to the assumption that the consumption rate of metakaolinite may follow the char burnout rate. In addition, this simplification leads to the homogeneous distribution of metakaolinite in the coal particle which is not found in reality. A larger discrepancy is expected
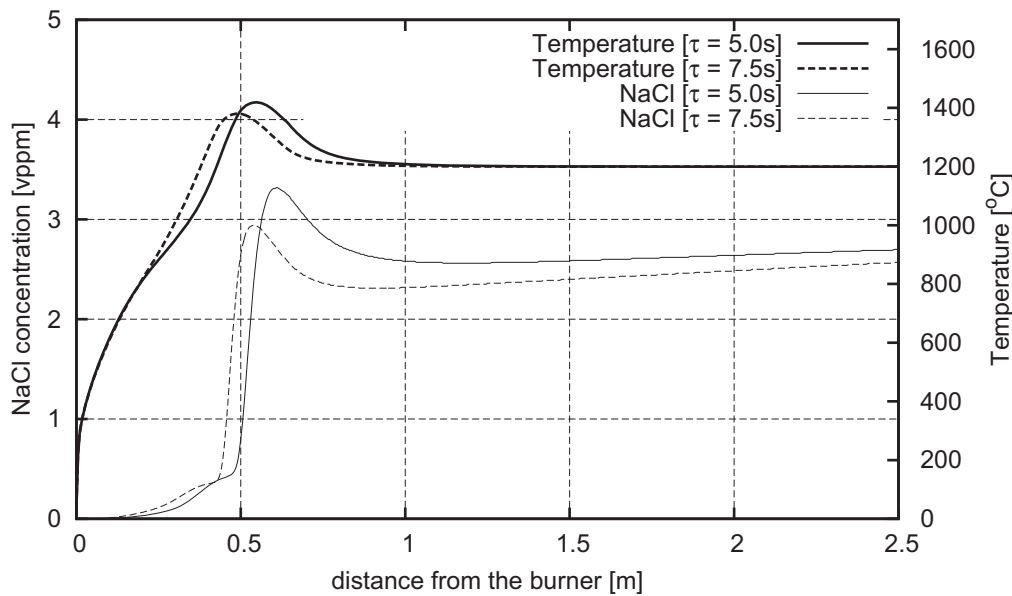
Figure 4.3: Flue gas NaCl concentration profile along the reactor axis. Reactor wall temperature $T_w = 1200\ ^\circ C$.

to occur if a case with higher residence time is considered. In this case the consumption rate of metakaolinite ($2SiO_2.Al_2O_3$) for capturing NaCl to form a water insoluble product ($NaAlSiO_4$) should be lower than the char burnout rate. This reaction is based on Reaction 3.3 in section 3.2.1. However, the typical residence time in the furnace of a pulverized coal fired utility boiler is usually lower than 10 s. This means that the model predicts well the sodium release with an acceptable error. Furthermore, the secondary reaction model based on the AIOLOS char burnout model analogy can be applied in this case. A positive correlation can be observed as well between the sodium release and the reaction tube temperature. The sodium gas concentrations increase from 1.7 $vppm$ at 1100 $^\circ C$ to 5.3 $vppm$ at 1400 $^\circ C$ for residence time of 5 s, whereas the increase for residence time of 7.5 s is from 1.6 $vppm$ to 4.8 $vppm$. It can be seen that the quantitative and qualitative behaviour of sodium release seems to be different for the two residence times. Furthermore, the discrepancy of the released sodium in the gas phase between two residence times decreases as the temperature decreases. One reason for this is that at higher temperature, not only the alkali release rate, but also the alkali capturing rate is getting higher. Another reason is that the longer residence time allows more contact time for capturing the released alkali into the matrix of the coal or ash. The positive correlation between temperature and the capturing rate was also observed in [63, 128].

Fig. 4.3 shows predicted temperature and volume concentration of NaCl in the gas phase at the reactor wall temperature of 1200 $^\circ C$. From the original amount of water soluble sodium in the coal, a maximum possible concentration was calculated assuming 100% release. Considering
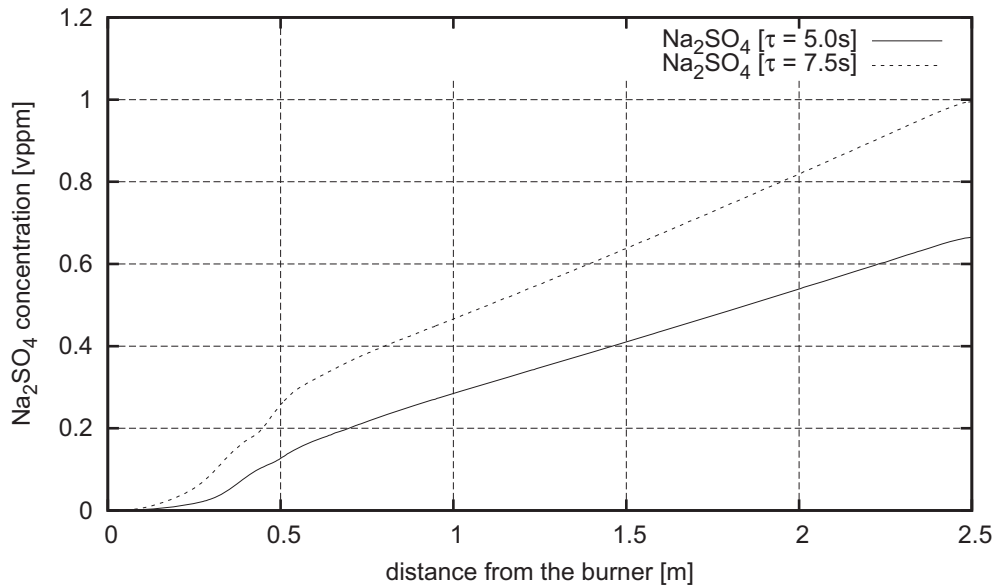
Figure 4.4: Flue gas Na_2SO_4 concentration profile along the reactor axis. Reactor wall temperature $T_w = 1200\ ^\circ C$.

the (Na+K)/Cl ratio, it is assumed that sodium will be released mostly as NaCl. Thus, the maximum concentration of NaCl would be 10 $vppm$. The figure shows that the concentrations of NaCl at the exit of the reactor are only around 25% of the maximum concentration. The simulation result implies a high retention of sodium by metakaolinite. The water soluble sodium and metakaolinite are assumed to be in the same particle so that the bonding reaction may occur before or as the sodium is evaporated [63]. This process may be completed in milliseconds in the combustion chamber [104]. The sodium may further be captured by metakaolinite after its release into the gas phase. This process could play a significant role at higher residence times. Based on the calculation, the amount of sodium which is captured by metakaolinite after having been released into the gas phase was around 3 $vppm$. This means that the capturing process as the sodium has been evaporated plays the predominant role under the prevailing conditions.

After being released in the gas phase, NaCl may be further converted to Na_2SO_4 in the presence of sulfuric gases. The formation of sodium sulfate for two residence times is presented in Fig. 4.4. Sodium sulfate has a lower vapor pressure compared to sodium chloride. Furthermore, unlike NaCl, physical condensation of sodium sulfate may occur in the range of the investigated reactor temperature. However, the figure shows that the concentrations of sodium sulfate are one order of magnitude lower than that of sodium chloride. Thus, it can be concluded that in this case, instead of the physical condensation, the capture of sodium in the gas phase is dominated by a combined process of diffusion and reaction at the high temperature, which is discussed in section 3.2.4. From the figure, it can be observed as well that the sodium
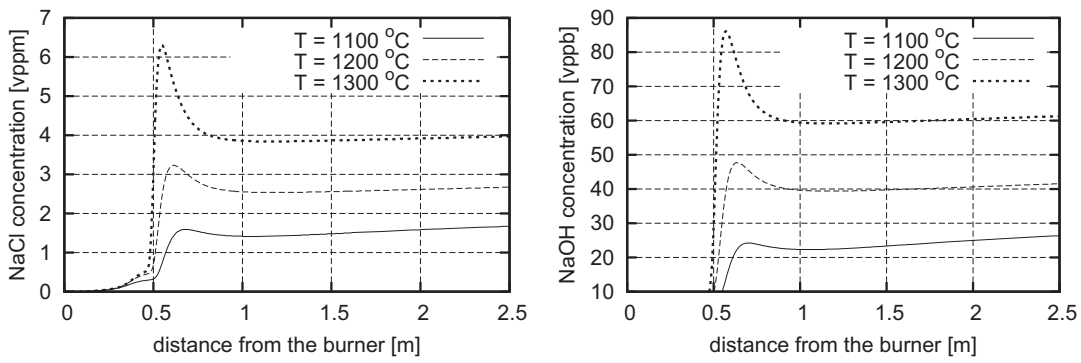
Figure 4.5: Profiles of NaCl and NaOH concentration along the reactor axis. Residence time $= 5 \ s$.
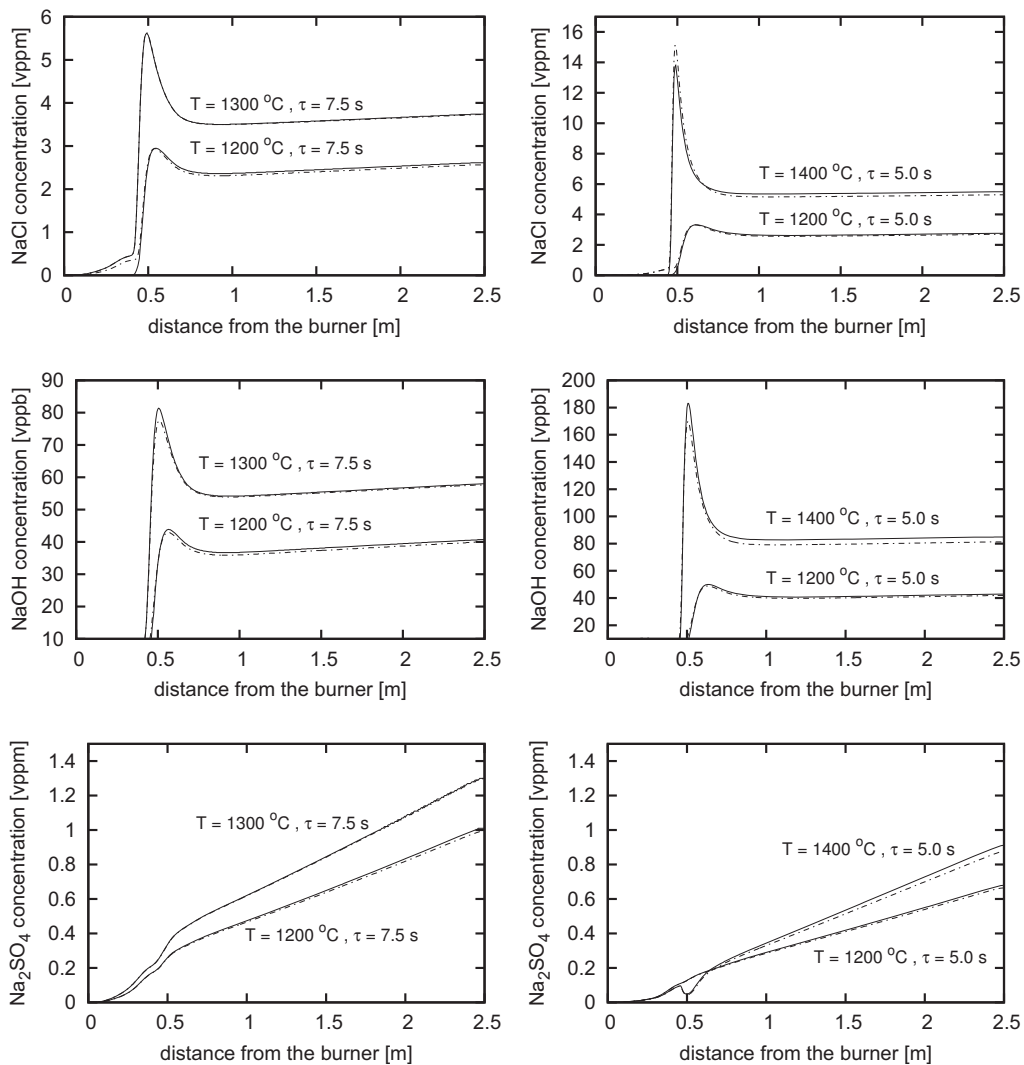

Figure 4.6: Comparison of the global mechanism (solid lines) with the detailed mechanism (dashed lines) at two residence times and two temperatures.

sulfate concentration is higher at higher residence time. Qualitatively, this result is consistent with the observation made by Iisa [47]. The conversion of sodium chloride to sulfate has not been completed yet even at the residence time of 7.5 s. This could be also attributed to the fact that the vaporization of sodium still occurs even only to a small extent until the end of the reactor. Then, the vaporized sodium chloride is further converted to sulfate.

Fig. 4.5 illustrates the axial profiles of NaCl concentration and NaOH concentration. At a residence time of 5 s, increasing temperature enhances the formation of NaCl and NaOH in the gas phase. All of the peak concentrations take place at the peak flame temperatures inside the reactor. NaOH may be converted as well to Na_2SO_4 providing condensible species which may affect the deposition process on colder parts of the furnace. However, comparing the concentration of NaOH to that of NaCl, it seems that the effect of NaOH in this case is not very likely. The similarity in trends between the NaCl concentration profiles and the NaOH concentration profiles are also shown at each temperature condition. This indicates that the equilibrium of the NaCl to NaOH reaction occurs rapidly, whereas the alkali capture and the alkali release are the rate limiting-step in the formation of alkali compounds in the gas phase. In addition, there are several evidences from the literature that bonding of NaOH by aluminosilicate is better than that of any other species such as NaCl and Na_2SO_4. However, it can not be assumed that the bonding of NaOH is more favorable than those species [57]. The importance of NaOH on the bonding reaction is also reported by Mwabe and Wendt [71]. These authors state that NaCl firstly will be converted to NaOH by reaction with water vapor and then the actual bonding reaction with NaOH take places. In this work, bonding reaction of NaOH illustrated in Fig. 3.4 will be not significant due to relatively small concentration of NaOH in the gas phase.

Concerning the homogeneous reactions of sodium in the gas phase, a global model is proposed as a simplification of the model which is given in [103]. The global model was constructed by considering the species of interest (NaCl and Na_2SO_4) which may condense on the colder parts of the furnace. In the global model, only two reactions are considered regarding the reaction of sodium compounds in the gas phase, one is the reaction (2) in Table A.1 (the formation of NaOH) and the other is the relevant reaction in Table 3.1 (the sulfation of NaCl). The concentrations of the species: NaOH, NaCl, and Na_2SO_4 from the global model have been compared to the ones calculated from the detailed model. The calculations for two residence times and temperature conditions ranging from 1200 $°C$ - 1400 $°C$ are shown in Fig. 4.6. From the figure, it can be seen that the global mechanism reproduces the results of the original model very well concerning the investigated species. In general, the concentrations predicted by the global model are slightly higher that the ones predicted by the detailed one. At certain temperatures, the discrepancies are more visible towards the exit of the reactor. However, considering the typical residence time and temperature inside a real furnace, the error introduced by the global mechanism against the detailed mechanism can be neglected.

In order to have a better prediction on the effect of sodium compounds on the deposition mechanism inside the utility boiler, an aerosol formation model coupled with the model of the formation of sodium compounds should be implemented in AIOLOS. However, this will promote an increase of computational time and cost especially when the detailed mechanism is still used. Hence, the simplification of the model to the global mechanism, on the one hand can reduce the model complexity and the computing time, and on the other hand it is able to predict the sodium compounds with good accuracy. The global model is utilized afterwards to predict the formation of condensible species in the gas phase when the simulations with large numbers of grid points are performed.

4.1.2 Potassium release calculation

To evaluate the predictive capability of potassium release, two experimental data sets are used. The experimental data are based on the work of Schuermann [101] and of Reichelt [85] for a coal with high content of chlorine and a coal with low chlorine content, respectively. The simulations were also performed on the atmospheric-pressure drop tube reactor with the same grid system used for sodium release calculation (section 4.1.1). The proximate, elementary, and ash analysis of the fuels are given in Table 4.3.

In terms of potassium release for low chlorine content coal, the measurements made for a lignite coal were chosen. At the measurement point, the gas temperature corresponds to the reactor wall temperature which ranged from 1100 to 1400 $°C$. The air ratio was 1.15, and the overall gas residence time was about 6 s. Using the data from coal analysis, it can be calculated that the ratio of Na+K to Cl is more than 1. With relatively low sulfur content of the coal, it is assumed that the potassium compound which is mainly released into the gas phase is potassium hydroxide. In this case, the reaction scheme in Table A.2 was used to model the transformation of the potassium compounds in the gas phase. After vaporization, the present species such as H, OH, O, and H_2O may affect the conversion of potassium. To reduce the computational effort, the radical mole fractions are expressed as functions of the major species O_2, H_2, and H_2O by utilizing the partial equilibrium approach for the hydrogen oxidation reaction sequence.

Based on the coal analysis, the ash content of the lignite coal is only a half of that for Ensdorf coal. A positive correlation between the reaction tube temperature and the released potassium concentrations is observed in Fig. 4.7. This indicates that the release of alkali is more dominating than its bonding reactions. Looking in more detail into the ash analysis reveals that the SiO_2 and Al_2O_3 content are relatively low in the coal ash. These species in the form of aluminosilicate are the most important species in terms of the secondary reaction of alkali species. Furthermore, the ash content itself in the coal is also low. This means that the effect of the secondary reaction seems to be negligible. As a conclusion, good agreement between the measured and calculated potassium concentration can be also seen from the figure even if the secondary reaction is not considered in this case.

Table 4.3: Coal analysis

			Lignite coal	Goettelborn coal
Proximate	Moisture	% raw	9.59	1.48
Analysis	Volatile	% raw	48.89	34.84
	Ash content	% raw	3.59	6.39
	Fixed carbon	% raw	37.93	57.19
Elementary	C	% raw	59.86	74.38
Analysis	N	% raw	0.65	1.2
	S	% raw	0.35	0.78
	H	% raw	6.2	4.87
	O_{diff}	% raw	32.9	10.74
	Cl	% raw	0.04	0.18
Ash	Al_2O_3	%	5.41	27.35
Analysis	CaO	%	36.37	5.61
	Fe_2O_3	%	12.87	13.53
	K_2O	%	0.59	3.00
	MgO	%	9.81	3.00
	Na_2O	%	6.4	0.45
	SiO_2	%	43.82	2.51
	SO_3	%	-	1.93

A further modelling study should predict the potassium release for high chlorine content coal. In this case, the experiment was conducted to determine the released potassium for a bituminous coal (Goettelborn). In the experiments, the temperature ranges from 1000 to 1400 $°C$. To evaluate the predictive capability, the experimental result corresponding to an overall residence time of about 4 s was chosen. Based on the coal analysis, the ratio of Na + K to Cl is lower than 1. Therefore, potassium chloride is the predominant potassium compound in the gas phase. Once in the vapour phase, atomic potassium encounters the complex reducing-oxidizing chemistry of the flame and post-flame regions where the chemical reactions governing the formation and destruction of potassium chloride occur in parallel. The important chemical reactions and their forward reaction rate coefficients are listed in Table A.3. The alkali release mechanism in this case is similar to the model implemented for the lignite coal. Again, the secondary reaction is neglected since the release of alkali is investigated at a low residence time. From Fig. 4.8 it can be seen that the released alkali as a function of temperature shows the same trend as the experimental data. The alkali release increases linearly as the temperature increases. However, the calculated potassium concentration is beyond the expectation that it should lie above the experimental values. During the coalification, the alkali undergoes a
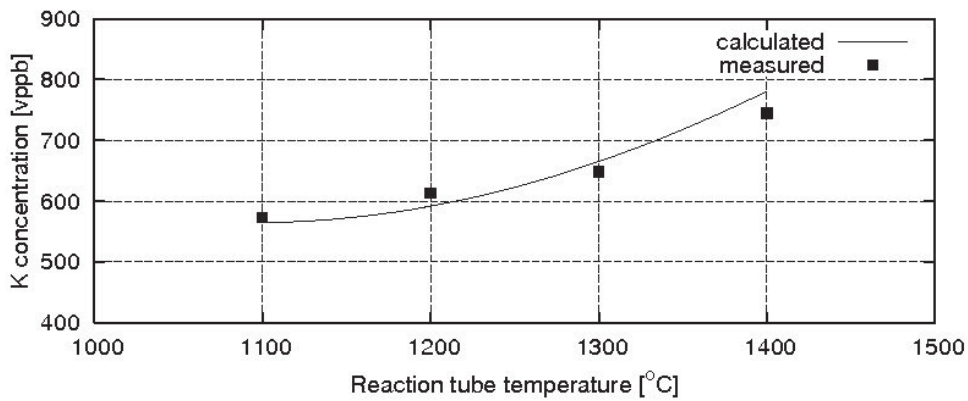
Figure 4.7: Flue gas K-concentration vs. temperature for the combustion of a lignite coal.
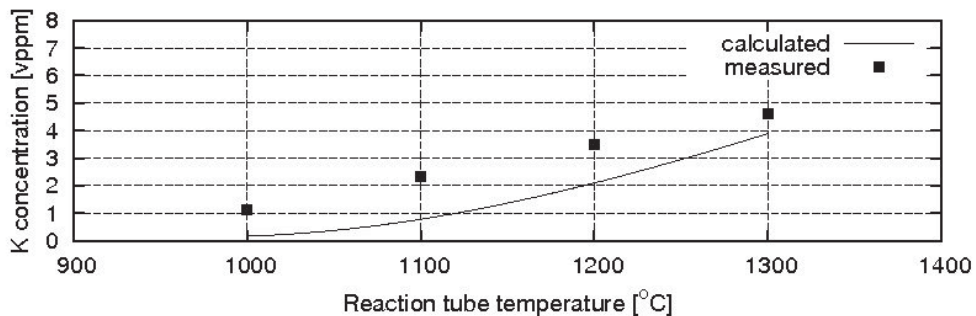

Figure 4.8: Flue gas K-concentration vs. temperature for the combustion of Goettelborn Coal.

process which may change its forms in the coal matrix. This will lead to the heterogeneity in alkali form as well as the difference in behaviour of alkali release for different types of coal. The reaction rate in terms of alkali release for a type of coal may not be applicable for another type of coal. Furthermore, even if the potassium concentration is obviously under-predicted for the Goettelborn coal, it is still in the same order of magnitude as the measured values.

4.1.3 The effect of alkali compounds on the deposition mechanisms for coal and biomass-fired boilers

In order to investigate the capabilities of the model to predict the effect of potassium compounds on the deposition rate at the initial stage of deposit build-up, simulations were performed for the 0.5 MW semi-industrial pulverized-fuel combustion facility (KSVA) [42]. A simple sketch of the KSVA including a cooled probe can be seen in Fig. 4.9. Two biomasses with different potassium content are considered in this case. The proximate analysis as well as the ultimate analysis of the biomasses can be seen in Table 4.4. More details about the fuel analysis are described in section 4.2. All simulations were run with constant thermal input of 400 kW with

an air ratio of 1.2. The calculation time for a basic simulation run was approximately 15 h on a NEC-SX8 supercomputer using eight CPUs.
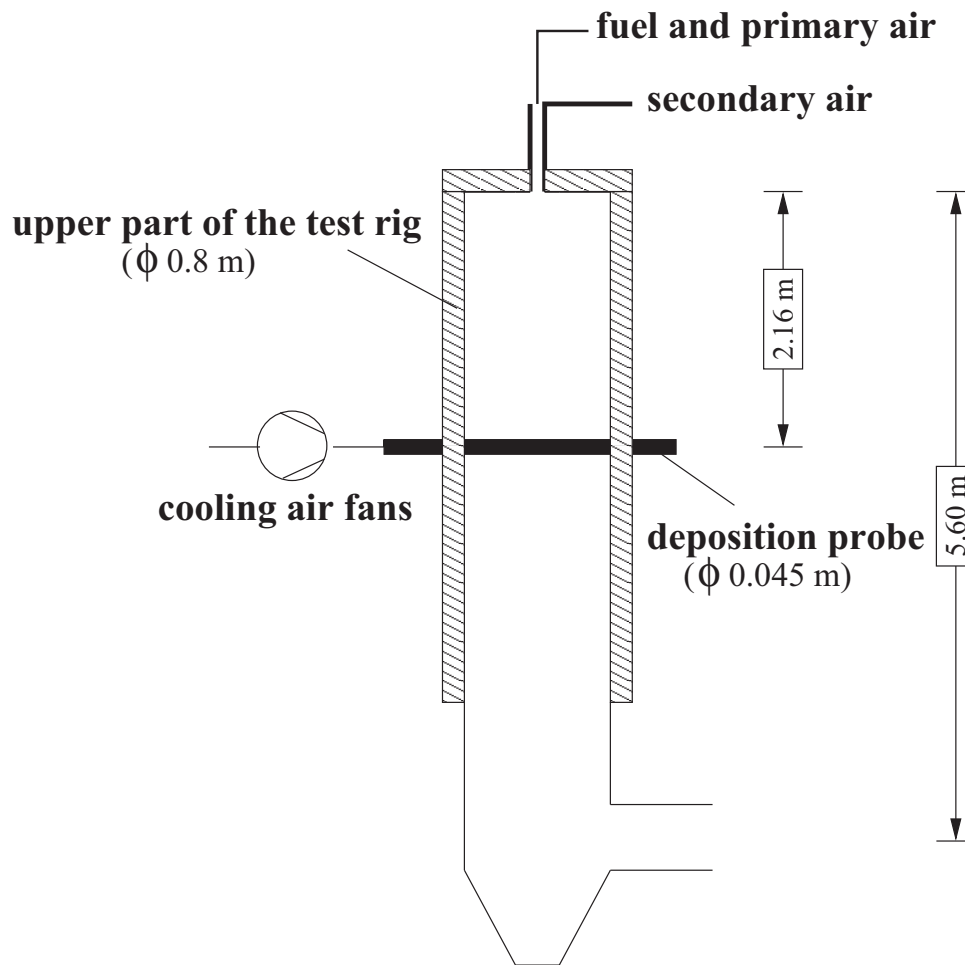

Figure 4.9: Pulverized-fuel combustion test rig (500 kW).

From the fuel analysis, the particle sizes for both biomasses are relatively large. Thus, it is reasonable to assume that the only deposition mechanism of ash particles to be considered in this work is inertial impaction. However, considering the high volatile content of biomasses and possible fragmentation processes, small size particles may form during combustion, then the mechanisms such as thermophoresis and eddy impaction will play a significant role for the particle deposition. The air-cooled probe is inserted in the furnace to simulate the heat exchangers in the convective section of a utility boiler. Observations of the superheater surfaces in boilers indicate that deposits may cover both the front and rear parts of the superheater tubes. According to literature [111] it is assumed that the large particles above 10 μm hit the front parts of the tube while the particles smaller than 10 μm deposit on the rear part of the tube through eddy impaction. Based on this assumption and considering the large size of biomass particles, deposition rates are calculated only on the front part of the probe. The

Table 4.4: Fuel analysis

			Hard coal (SK)	Straw 1 (BM1)	Straw 3 (BM3)
Calorific	HHV raw	MJ/kg	31.18	16.85	14.92
Value	LHV raw	MJ/kg	30.18	15.43	13.75
	HHV dry	MJ/kg	31.82	18.65	16.92
	LHV dry	MJ/kg	30.89	17.44	16.01
Proximate	Moisture	%	2.0	9.6	11.7
Analysis	Volatile	% dry	33.2	78.7	71.3
	Ash content	% dry	9.3	6.4	13.4
	Fixed carbon	% dry	56.2	14.8	15.3
Elementary	C	% dry	73.5	46.2	41.4
Analysis	N	% dry	1.48	0.65	1.09
	S	% dry	0.88	0.07	0.10
	H	% dry	4.26	5.46	4.18
	O_{diff}	% dry	9.0	40.8	38.9
	Cl	% dry	0.22	0.29	0.53
Particle Size	$d_{10\%}$	μm	9	265	120
Distribution	$d_{50\%}$	μm	37	800	600
	$d_{90\%}$	μm	81	1800	1650
Ash	Al_2O_3	%	23.6	1.0	0.4
Analysis	CaO	%	5.5	6.4	4.3
	Fe_2O_3	%	13.3	0.6	0.3
	K_2O	%	2.9	10.6	14.8
	MgO	%	2.9	1.4	0.9
	Na_2O	%	1.5	2.0	0.4
	SiO_2	%	40.1	70.4	68.6
	SO_3	%	7.4	2.4	1.9
	TiO_2	%	0.9	0.1	0.0
	P_2O_5	%	0.2	2.7	1.9
Ash Melting	$T_{0.95}$	$°C$	1070	750	810
Behaviour	$T_{0.5}$	$°C$	1315	1215	1235
	$T_{0.2}$	$°C$	1365	1380	1385

temperature of the air-cooled probe was kept constant at 650 $°C$, simulating the temperature range of the superheater tubes in a boiler. To predict particle arrival rates on the tube, inertial impaction is considered and calculated based on Lagrangian particle tracking (see section 2.7). In terms of alkali form in the fuel matrix, biomass is assumed to be similar to lignite coal. Furthermore, the alkali release model for lignite coal is also applied for biomass (see section 3.1).

A global view of deposition occurring inside the furnace can be seen in Fig. 4.10. The implemented operating conditions as well as the boundary conditions for both biomasses are similar. The simulations have been performed using a two-domain computational grid involving the burner and the upper part of KSVA.

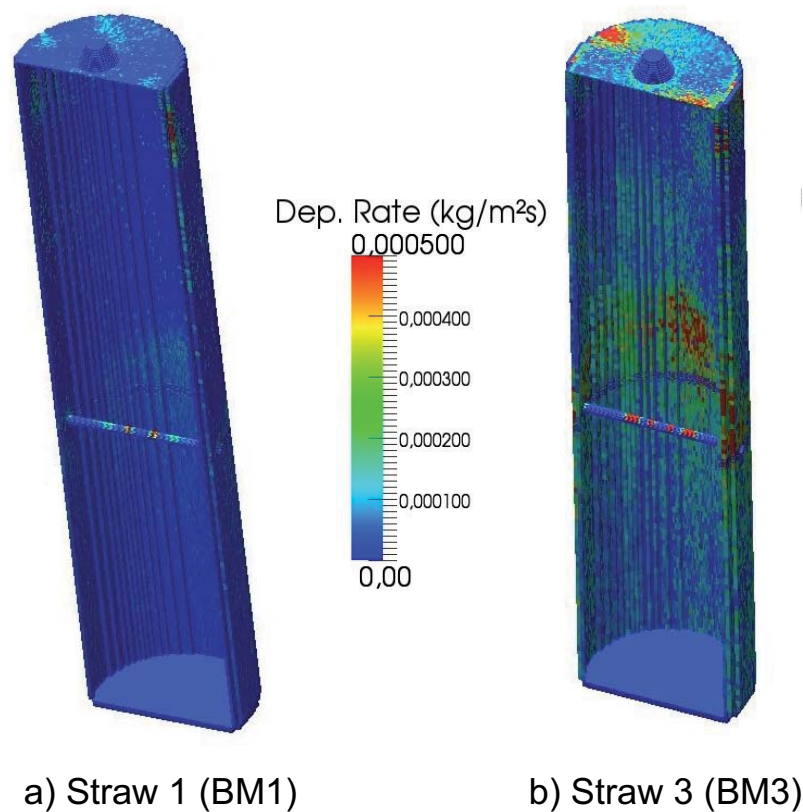a) Straw 1 (BM1) b) Straw 3 (BM3)

Figure 4.10: Calculated deposition rate profile on the KSVA wall.

At the initial stages of deposit formation, condensation of vapours may play an important role either on the furnace wall or on the convective tubes of a boiler. As the deposit grows thicker, the outer surface temperature of the deposit increases. The temperature increase is in the range of 30-100 $°C/mm$ which depends on thermal conductivity of the deposits and the local heat flux. This is the typical value for deposits in the furnace region [124]. With relatively high temperature increase, condensation has a significant effect only at the initial stage of deposit build-up in short time period. Once the initial deposit has formed, the deposit surface

tends to be sticky (according to the high temperature), and most of impacting particles will be held on the surface, thus deposit grows thicker. This indicates that particle impaction is the dominant mechanism for slag build-up [9]. Unlike slagging deposit, the increase of temperature in the convective pass of a boiler (categorized as fouling deposit) is somewhat smaller due to the lower flue gas temperature. In this case, condensation processes play a significant role. The effect of condensation in the convective part may have a longer time scale compared to that in the furnace.

Based on the fuel analysis, it can be seen that both biomasses have a relatively high content of chlorine and potassium. Then, it can be expected that potassium will be released in the gas phase as potassium chloride. The release of potassium chloride for biomass is calculated based on the mechanism which is described in section 4.1.2. In the simulation of the KSVA, the released potassium chloride may condense on the cooled deposition probe providing a sticky layer that efficiently captures other ash particles.
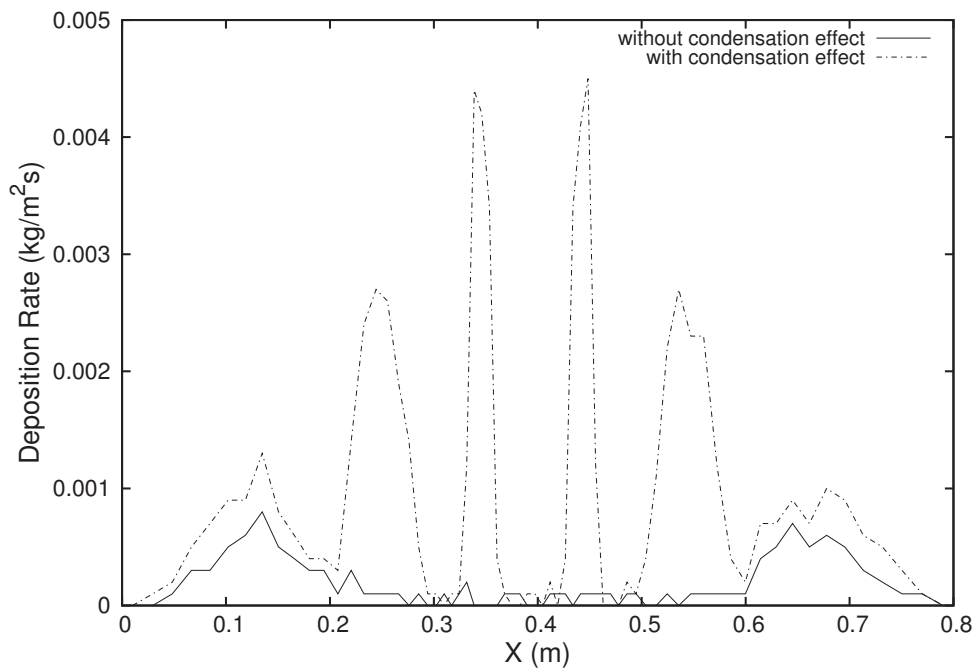

Figure 4.11: The deposition rate along the probe with and without condensation model.

The simulation results in Fig. 4.11 can give a first impression about the effect of condensible potassium chloride on the deposition rate. The simulations were run for two cases, one with the existence of condensible KCl on the probe, and the other without. Based on the calculation, the deposition of ash particles may still occur even without the existence of condensible KCl, but to a much smaller extent. The deposition rate is the averaged deposition rate over the circumference of the probe for every position along the probe. Inertial impaction, the only deposition mechanism for particles which is considered in this case, can be categorized as a fast
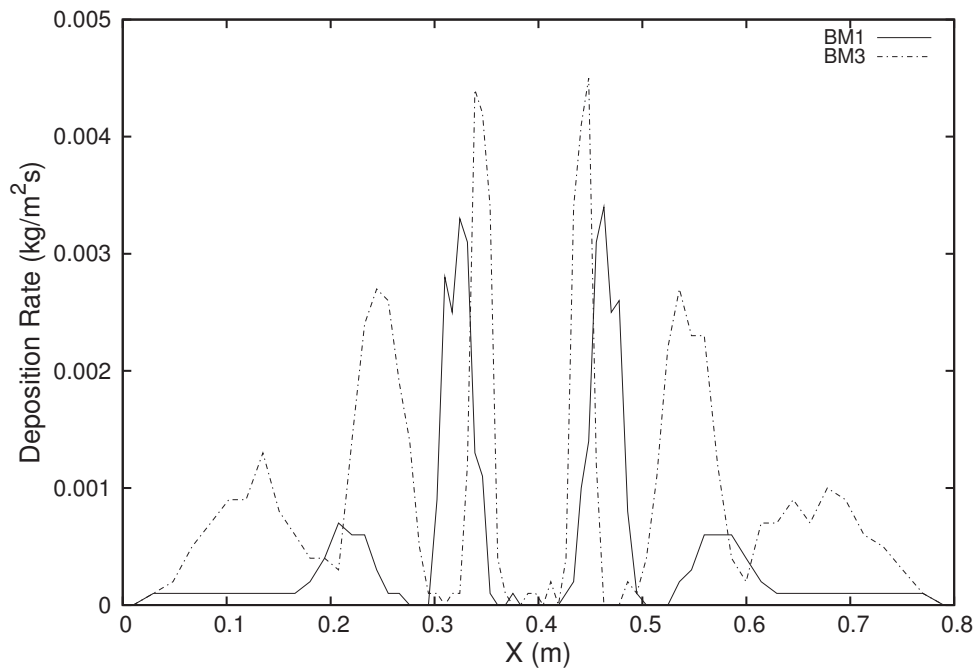
Figure 4.12: The deposition rate profile along the probe for BM1 and BM3.
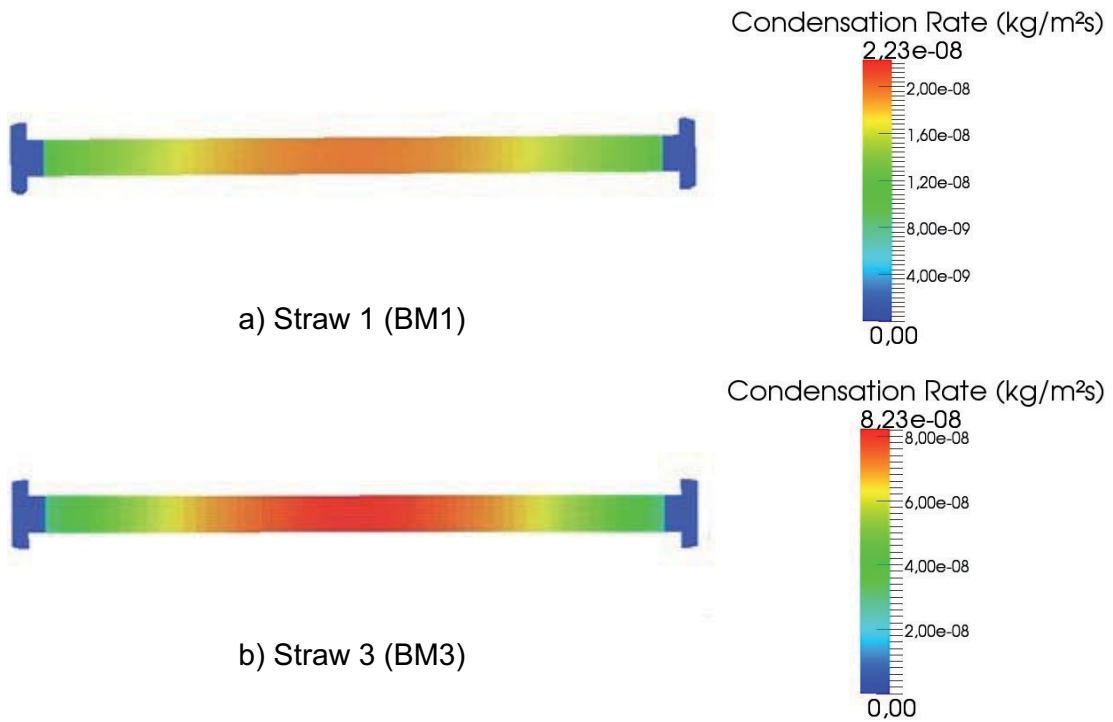

a) Straw 1 (BM1)

b) Straw 3 (BM3)

Figure 4.13: Calculated condensation rate profiles on the deposition probe.

deposition process. Therefore, a small fraction of melting particles is formed to provide a sticky layer on the particle. By comparing the two simulations, it can be seen that the deposition rate in a certain area may differ by a factor of 30. Thus, from this observation, it can be concluded that the consideration of the condensible potassium species model has a significant influence on the predicted amount of deposit build-up.

In order to obtain further insight into the deposition rate on the probe, two profiles are shown in Fig. 4.12. The deposition rate for BM3 is higher than that for BM1, reflecting the higher amount of ash for BM3 than for BM1. It can be observed also from Fig. 4.13 that the condensation rate is higher for BM3 than for BM1. This can be the implication of higher amount of potassium in BM3 than for BM1. From the figure, it can be observed also that the condensation rate is higher at the middle of the probe which corresponds to the axis of the reactor. This can be attributed to the higher concentration of KCl due to the higher temperature on the axis. For biofuels like straw, the formation of the inner layer deposit on superheaters by condensation plays a larger role than that of the furnace deposit. Considering this importance, a more detailed investigation of the deposition process, including a model describing the increase of the deposit surface temperature in a time interval should be made. This subject will be discussed in section 4.2.

4.1.4 Summary

In this section, a numerical modelling approach to predict alkali release in the gas phase has been discussed. The models were implemented in the 3D combustion simulation code AIOLOS. In this case the alkali release model for the lignite coal is also implemented for biomass. Evaluation of the model has been performed by running the simulations on a small-scale entrained flow reactor. The model for sodium release is evaluated by running simulations for the combustion of a German bituminous coal. The effect of the secondary reaction is also applied in the model by using the char-burnout model analogy in AIOLOS. The simulation results correspond well with the measurements especially at a residence time below $10 \ s$. In order to evaluate the proposed model of potassium release, simulation runs were performed for the combustion of a lignite coal with a low content of aluminosilicate, and a hard coal at a low residence time. The calculated potassium release from those cases was found to be in good agreement with the measured values. The effect of the alkali/Cl ratio in the fuel on the alkali release is also demonstrated in this work. Furthermore, the impact of potassium chloride on the deposition on the superheater has also been modelled. Using biomass with high content of potassium and chlorine, simulation runs were performed on a 500 KW semi-industrial scale pulverized fuel test rig. Based on the results, it can be concluded that the condensible KCl on the probe has a significant effect on the deposition rate especially at the initial stage of deposit build-up.

4.2 Simulation of Deposit Formation

In the previous section, alkali release in a simple two-dimensional semi-technical scale combustion test rig has been studied. By comparison with measured data, these predictions make it possible to evaluate many aspects of mathematical models for the behaviour of alkali compounds during combustion. In order to investigate the deposit formation in a practical situation, a more comprehensive model has been implemented in AIOLOS based on the theoretical background described in chapter 3. A model taking into account the effect of deposit formation on the temperature increase has been integrated into the deposition model of AIOLOS. Experiments conducted at the 0.5 MW pulverized-fuel combustion test rig (Fig. 4.9) are also used to evaluate the proposed models. To validate the model, the data sets published by Heinzel [42] concerning the mass concentration of ash on the deposition probe have been used. On these terms, the predicted concentration of accumulated deposit after several hours will be compared to the experimental data. The temperature increases are obtained at several time steps according to the thickness and thermal properties of the deposit.

In order to investigate the behavior of deposit formation for a biomass co-combustion system, simulations were performed at various thermal shares of biomass. Two kinds of straw termed "BM1" and "BM3" were co-fired with a hard coal ("SK"). The proximate, elementary and ash analysis are shown in Table 4.4. Several operating conditions are set to be constant for all thermal shares as shown in Table 4.5, whereas the fuel flow rate as well as the volume flow of secondary air (SL) for different thermal shares are shown in Table 4.6.

Table 4.5: Constant operating conditions

Volume flow of fuel carrying air	100 m_N^3/h
Air ratio	1.2
Thermal input	400 kW
Temperature of secondary air	300 $°C$
Duration of ash collection	16 h
Deposition probe diameter	0.045 m

As mentioned in section 3.6, the prediction of deposit formation has been performed in a post-processing step based on the coupled Eulerian/Lagrangian framework. Basic simulations for all cases were made in two steps. In the first step, a simulation without the deposition probe was conducted to extract some free stream properties according to the probe position. These properties are required as the boundary conditions to calculate the deposition rate as well as the condensation rate. In the second step, a simulation with the deposition probe was made supplying flow, temperature, and species concentrations field. Then, the post-processing step

Table 4.6: Fuel flow rate

Thermal share	Coal mass flow rate	Biomass mass flow rate	Volume flow of SL
	$[kg/s]$	$[kg/s]$	$[m_N^3/h]$
87.5 % Coal - 12.5 % BM1	1.122E-02	2.967E-03	335.033
75 % Coal - 25 % BM1	9.622E-03	5.935E-03	332.761
50 % Coal - 50 % BM1	6.414E-03	1.187E-02	328.306
75 % Coal - 25 % BM3	9.622E-03	6.702E-03	324.768

was executed to calculate the deposit build-up within several time steps using the boundary conditions obtained from the basic simulations. Large numbers of particles are tracked through the furnace until they touch and eventually stick to the furnace wall or the deposition probe, or they simply leave the furnace through an outlet. The arrival rates of the alkali species and those of ash particles on various surfaces are calculated considering the major deposition mechanisms, i.e. condensation and inertial impaction, respectively. Based on the computed arrival rates, the deposition rates are estimated taking into account particle and substrate adhesion propensity which is calculated based on the melting behaviour approach described in section 3.4.1. The basic simulations were performed on the supercomputer NEC SX-8 of the High Performance Computing Center (HLRS) at University of Stuttgart. The computational time with eight processors for each step amounted to approximately 15 hours.

In case of a biomass co-combustion system, the reference fuel used in this work is a typical German hard coal. The coal is from the "Saar" region known as "Goettelborn" coal. From Table 4.4, it is obvious that the coal is different from the biomasses with respect to the calorific value, volatile and fixed C content due to the degree of coalification. Biomass, the precursor of coal, was converted into lignite or brown coal which is further converted into bituminous or hard coal after many millions of years. During the coalification process, the fuel undergoes a physical and chemical transformation which leads to the increase of the calorific value and the fixed C content and the decrease of the volatile content. Whereas the coal has an ash content of approx. 9%, the biomasses have 6.4 % (BM1) and 13.4 % ash (BM3), respectively. There is quite a big difference in the ash content between the two straws.

From the elementary analysis, the combustible matter of the biomasses is comparable ranging from 41.4 - 46.2 % whereas the C content of the hard coal is around 70 %. On the contrary to the C content, biomasses usually have a higher content of oxygen than hard coal. This observation is also similar with respect to the volatile content and the fixed C content from the proximate analysis of the fuels. The biomasses have around 15 % fixed C and 70 % volatile matter, whereas the coal has 56.2 % fixed C and 33.2 % volatile matter.

Sulfur and chlorine may play a significant role for the formation of the condensible species. From the elementary analysis, the sulfur content of the coal is 0.88. This value is relatively high compared to the sulfur content of the biomasses. Straw 1 (BM1) has 0.07 % sulfur, whereas the sulfur content of Straw 3 (BM3) is slightly higher at 0.10 %. Furthermore, the chlorine content has a big influence to the form of alkali released in the gas phase. Generally, straw has a high chlorine content. It can be seen that Straw 1 (BM1) has 0.29 % chlorine, whereas the chlorine content of Straw 3 (BM3) is almost twice as much as that of Straw 1 (BM1).

In terms of calorific value, the high heating value of coal is 31.18 %, whereas that for biomasses ranges from 14.92-16.85 %. A bigger difference between the high heating value and the low heating value for both biomasses compared to that for coal is observed. This is due to the moisture content of the fuels.

The coal was milled to give a particle size distribution of 90 % less than 81 μm which was covered by assuming ten particle size classes (see Table 4.7). Biomasses have relatively big particle sizes. From Table 4.4, it can be seen that 90 % of BM1 particles is less than 1800 μm, whereas 90 % of BM3 is less than 1650 μm. In practical applications, it is allowable to inject a larger particle size of biomass than that of coal in pulverized fuel co-combustion [41]. As a boundary condition for the simulation runs, the biomasses were also distributed in ten particle size classes as shown in Table 4.7. The mass percentage in each class is similar (i.e., 1/10 of the total mass).

Table 4.7: Particle size distribution

	Mean particle diameter [μm]		
Particle class	Hard coal	BM1	BM3
1	4.5760	130.10	60.130
2	12.410	337.10	173.90
3	18.800	483.80	283.40
4	25.150	622.50	399.70
5	31.840	763.30	528.40
6	39.220	913.90	676.50
7	47.790	1084.0	855.20
8	58.510	1291.0	1088.0
9	74.030	1581.0	1438.0
10	133.50	2611.0	2935.0

Based on the ash analysis, the ash composition of the fuels differs significantly. This implies a different behaviour of the particle ashes with respect to their tendency to stick on the furnace surfaces. Whereas the biomass ashes are dominated by the silicium content of approx. 70 %,

the coal ash mostly consists of three species, i.e. SiO_2, Fe_2O_3, and Al_2O_3. The sodium content of the fuels is comparable to each other with BM3 at the lowest. In addition, potassium in both biomasses is relatively high, 10.6 % for BM1 and 14.8 % for BM3. On the other hand, the potassium content of coal is only a quarter of that of biomass. In general, potassium of biomass is the alkali species that has a significant amount in the fuels. More details obtained from an elution analysis show that around 12 % of sodium content in the coal is in the form of water soluble one, whereas the water soluble sodium in the straw is around 80 %. The potassium content in straws is dominated by the water soluble one (80 %). On the contrary, only around 2 % of potassium in the coal can be classified as water soluble potassium [42]. This observation suggests a great affinity of potassium in coal to the aluminosilicate.

4.2.1 Simulation results for coal-fired boilers with biomass co-combustion

In this section, some simulation results of the biomass co-combustion system are shown and discussed. These cases are classified as the basic simulations, and their results will be used as the boundary conditions in the post-processing step.

Fig. 4.14 shows the temperature profile along the axis of the furnace. In this case, 25 % BM3 (thermal share) is fired with the reference coal. Compared to the experimental data, the temperatures with the exception of the peak temperature are reasonably predicted. With respect to the peak temperature location, the predicted one occurs around 0.25 m earlier than the measured one. The discrepancy may be attributed to difficulties in determining the swirl number that was applied in the experimental investigations. Furthermore, the figure shows that the temperature tends to be lower towards the outlet of the furnace. Unlike the entrained flow reactor presented in section 4.1.1, the wall of this semi-technical scale furnace is not pre-heated. Furthermore, the constant temperature profile near to the reactor exit (see Fig. 4.3) is not observed in this case.

A further investigation has been made for three different thermal shares of BM1. The predicted temperature profiles in Fig. 4.15 show that for all thermal shares, the peak temperature is found at a distance of 0.25 m from the burner. A similar observation can be expected also in case of BM3 co-combustion. From figure 4.15, it can be seen that a case with the highest thermal share of coal yields the highest peak temperature. This is the implication of the higher heating value of the coal compared to the biomasses. The flame temperature with 87 % coal is around 20 $°C$ higher than the temperature with 75 % coal, whereas the difference between the flame temperature of 75 % coal and of 50 % coal is around 50 $°C$.

In accordance to the fuel analysis, the alkali species having the most significant amount in biomasses is potassium. As mentioned before, the sulfur content of the coal is relatively high. Co-firing biomasses with coals having a high sulfur content may lead to the formation
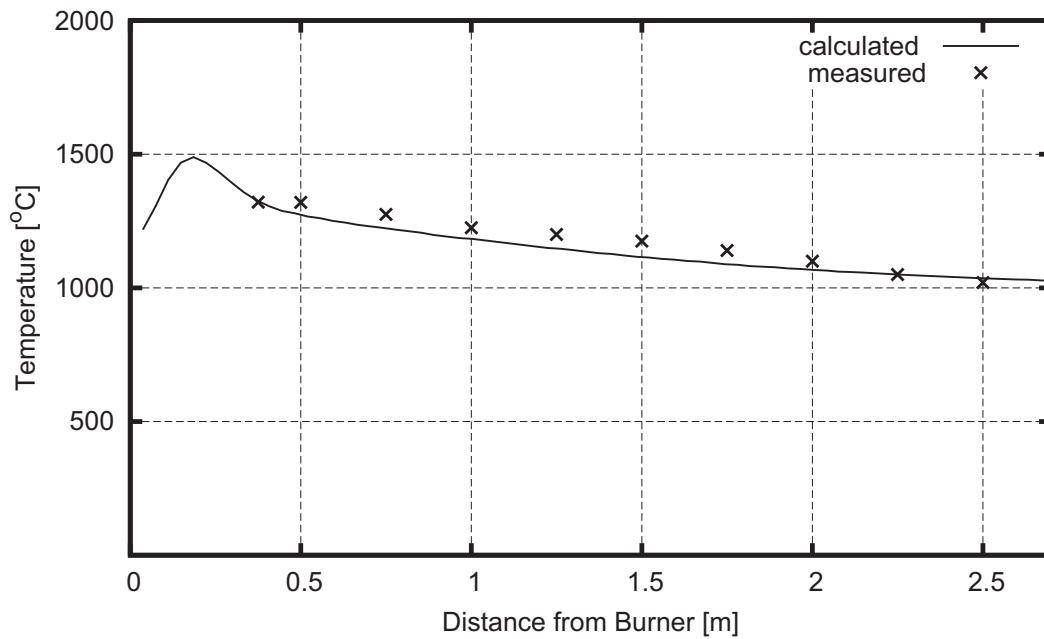
Figure 4.14: Temperature distribution along the furnace axis for 75 % Coal - 25 % BM3.
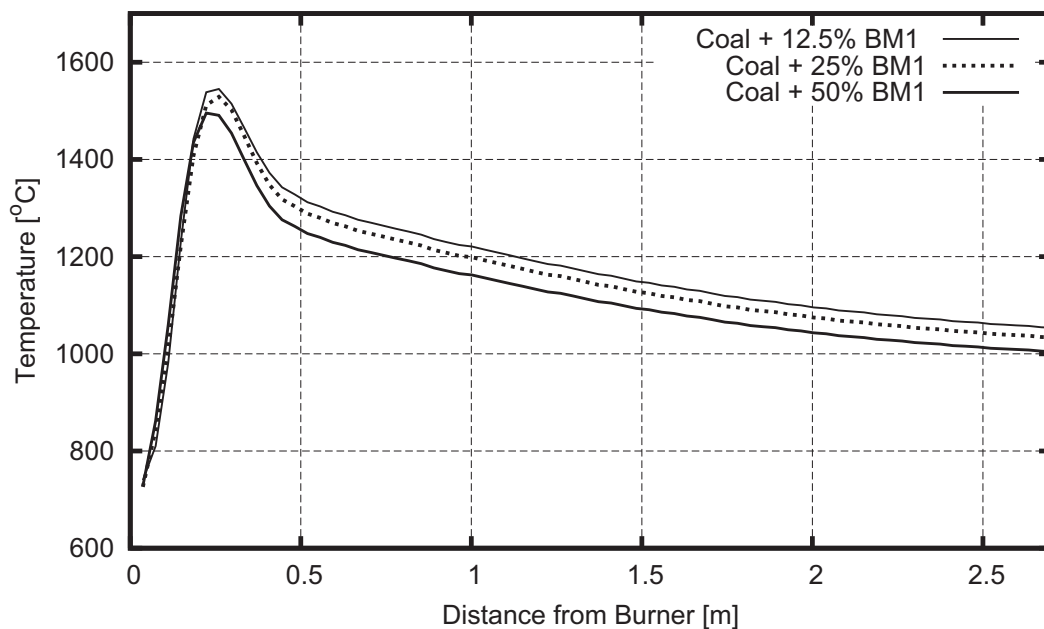

Figure 4.15: Temperature profile along the furnace axis for three different thermal shares of co-firing BM1 with coal.

of potassium sulfate in the gas phase. In this work, potassium sulfate is assumed as the only alkali species affecting the deposition mechanisms of the co-firing system. The vapor pressure of potassium sulfate is lower than that of potassium chloride. Furthermore, it makes sense to assume that condensation of potassium sulfate is more likely than that of potassium chloride [47, 105]. The mass fraction of potassium sulfate along the furnace axis for various thermal shares of biomass is given in Fig. 4.16. It can be seen from the figure that all cases show the
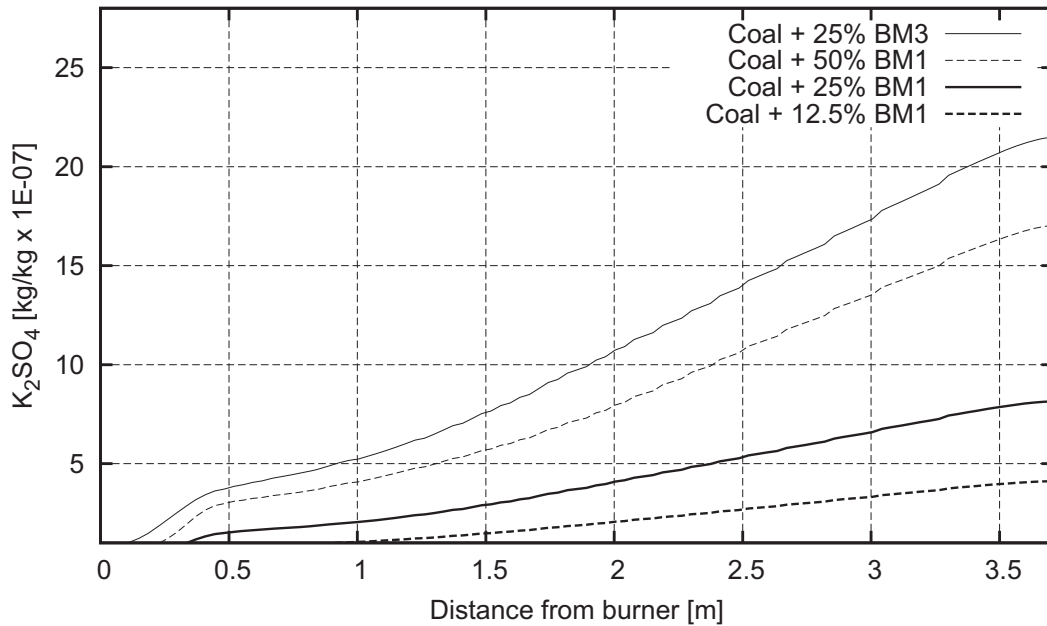

Figure 4.16: Mass fraction of K_2SO_4 along the furnace axis.

same trend. The first transverse is observed at the position where the peak temperature takes place. Afterwards, the potassium sulfate continues to form towards the end of the furnace. A further observation of the potassium sulfate concentration reveals that the formation rate of potassium sulfate is initially quite fast. Afterwards, the rate becomes slower, then increasing again until the end of the furnace. At the initial stage, the formation of potassium sulfate is determined by the vaporization of KCl in the gas phase. Once the vaporization is completed, the sulfation rate predominantly depends on the availability of SO_3 in the gas phase, and the availability of SO_3 is affected by the oxidation of SO_2 to SO_3. On the other hand, it was observed by Iisa [47] that the conversion of potassium chloride to its sulfate is higher as the temperature decreases. In this work, the oxidation model of SO_2 is included into the global model in terms of the formation of alkali sulfate (see reaction in table 3.1). The figure shows also that the mass fraction of potassium sulfate with 25 % thermal share of BM3 is the highest among others. Compared to the case of BM1 with the same thermal share condition, the case of BM3 shows a higher mass fraction of potassium sulfate. It can be attributed to the higher

content of potassium in BM3 than in BM1. Temperature condition has been shown also to have an effect on the release of alkali and the formation of alkali compounds in the gas phase. However, the temperature profiles from the two cases (Fig. 4.14 and Fig. 4.15) are not so different to each other to be a reason for that difference.

Looking in more detail to the cases of BM1 co-firing, the importance of the potassium content on the formation of potassium sulfate can also be seen. The co-firing system with lower thermal share of BM1 implies the higher temperature along the axis which yields the higher release rate of potassium chloride. However, a lower content of potassium due to the lower thermal share of BM1 may be the limiting factor for the formation of K_2SO_4 in the gas phase.
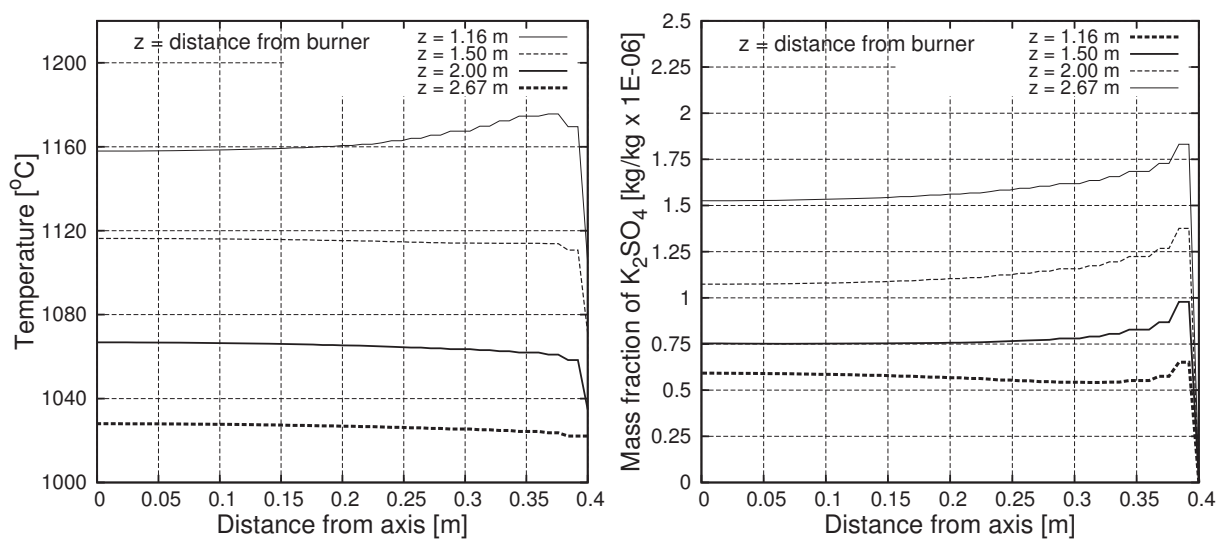

Figure 4.17: Predicted temperature and mass fraction of K_2SO_4 for coal + 25 % BM3.

The temperature profiles as well as the potassium sulfate profiles in radial direction are given in Fig. 4.17. The radial profiles are calculated at several positions concerning the distance from the burner. As shown in the figure, the highest temperature is observed at the distance 1.16 m from the burner. The temperature is getting lower at the position farther from the burner. This observation is consistent with the temperature profile in axial direction shown previously. After the peak temperature, a temperature decrease is observed towards the end of the furnace. On the contrary, the highest mass fraction of K_2SO_4 occurs at the distance 2.67 m from the burner. This is in agreement with the axial mass fraction shown in Fig. 4.16. Furthermore, the temperature profile varies widely near the burner. It can be attributed to the effect of the swirling factor in order to maintain a stable flame. Further downstream, the temperature distribution becomes more homogeneous due to the heat loss of the flame. In terms of K_2SO_4 mass fraction, the difference at each axial position is in the order of 10^{-6}. The highest gradient

is observed near to the furnace wall. This observation is made for coal + 25 % BM3, but a similar behaviour may be expected also for the other cases.

(a) Film theory
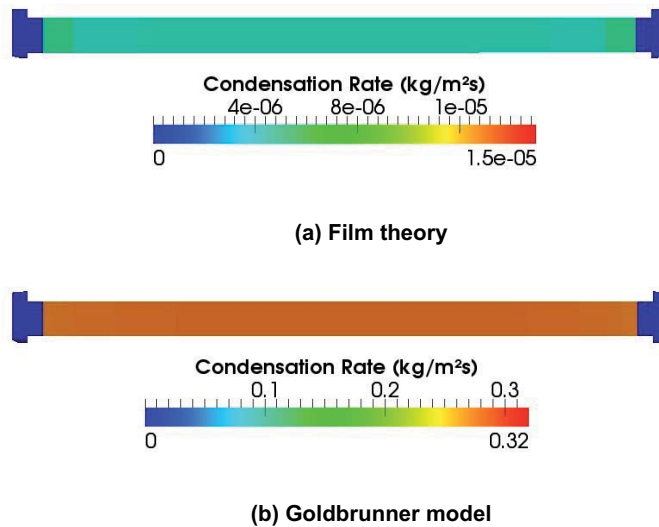

(b) Goldbrunner model

Figure 4.18: Condensation rate on the deposition probe for coal + 25 % BM3. Please note the different scales of the figures.

So far, the results from the basic simulations have been discussed and evaluated. A result obtained from the post-processing step is given in Fig. 4.18. The figure shows the condensation rates for K_2SO_4 on the deposition probe which are calculated by two condensation models. The deposition probe is located $2.67\ m$ downstream of the burner (see Fig. 4.9). A relatively big difference can be observed concerning the condensation rate predicted by the two models. The calculated rate obtained by the Film theory is about five orders of magnitude lower than that obtained by Goldbrunner's model. By using Goldbrunner's model, the deposit composition will be dominated by the condensible species which is far from reality if the result is compared to the experimental investigation. A similar observation with respect to the rate differences can be found also in the work of Hoppe [45]. In his work, the condensation rate predicted by the Film theory for Na_2SO_4 is six orders of magnitude lower than that by Goldbrunner's model. The difference is attributed to the implementation of the ratio between the concentration of condensible species at the boundary layer thickness and that of condensible species in the bulk gas for Goldbrunner's model. The result indicates that the film theory is more applicable in the present work. Hence, from this point onward, the film theory will be utilized to take into account the effect of K_2SO_4 on deposit formation. Furthermore, the figure shows that the condensation rate distribution is relatively homogeneous for the two models. This can be attributed to the homogeneous profiles observed for temperature and K_2SO_4 at this axial position as shown in Fig. 4.17.
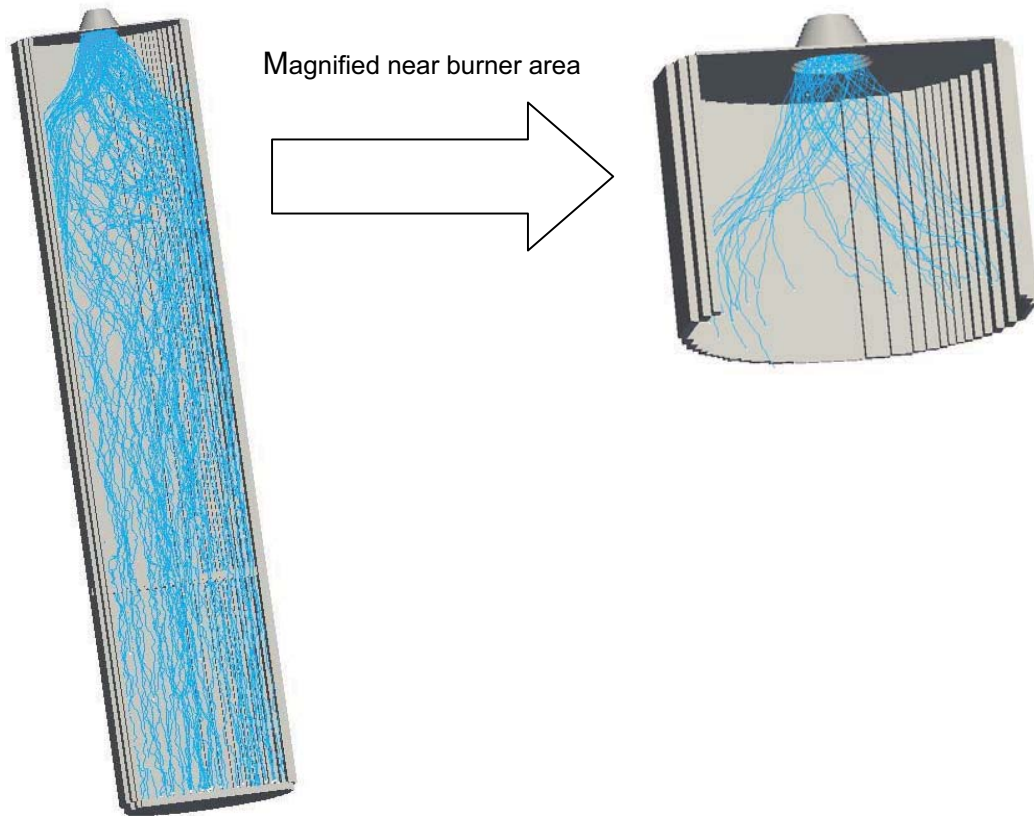
Magnified near burner area

Figure 4.19: Particle trajectories for coal + 25 % BM3.

Particle trajectories for the whole particle spectrum inside the furnace are presented in Fig. 4.19. In order to investigate the particle behaviour near to the burner, this area is magnified as shown on the right hand plot. In this case, a swirling factor of 0.49 is implemented to the secondary air flow. From the figure, it can be seen that most of the particles follow the secondary air flow. The figure shows that most of the particles get in touch with the furnace wall for the first time at a distance about 0.25 m from the burner. This implies that assuming no-slip condition between particle and fluid phase can be applied in the Eulerian approach to predict the flow behaviour in the basic simulations with a reasonable result. In terms of surface geometry, the particle that bounces to the probe surface is omitted from the calculation since statistically a particle may not get in touch with the surface twice [51].

Fig. 4.20 shows the deposition rate inside the furnace at the initial stage of deposit formation. For sake of clarity, the deposition probe is magnified and presented with its own scale. As mentioned on the theoretical background in section 3.3.5, the major deposition mechanism namely inertial impaction is considered. To deal with the fraction of arriving particles depositing on the furnace walls, a concept proposed by Walsh [119] is used. If the sticking probability for the arriving particle is known, for instance by using the melting approach, the fraction of arriving particles depositing can be obtained by a combination of particle and surface temperatures.
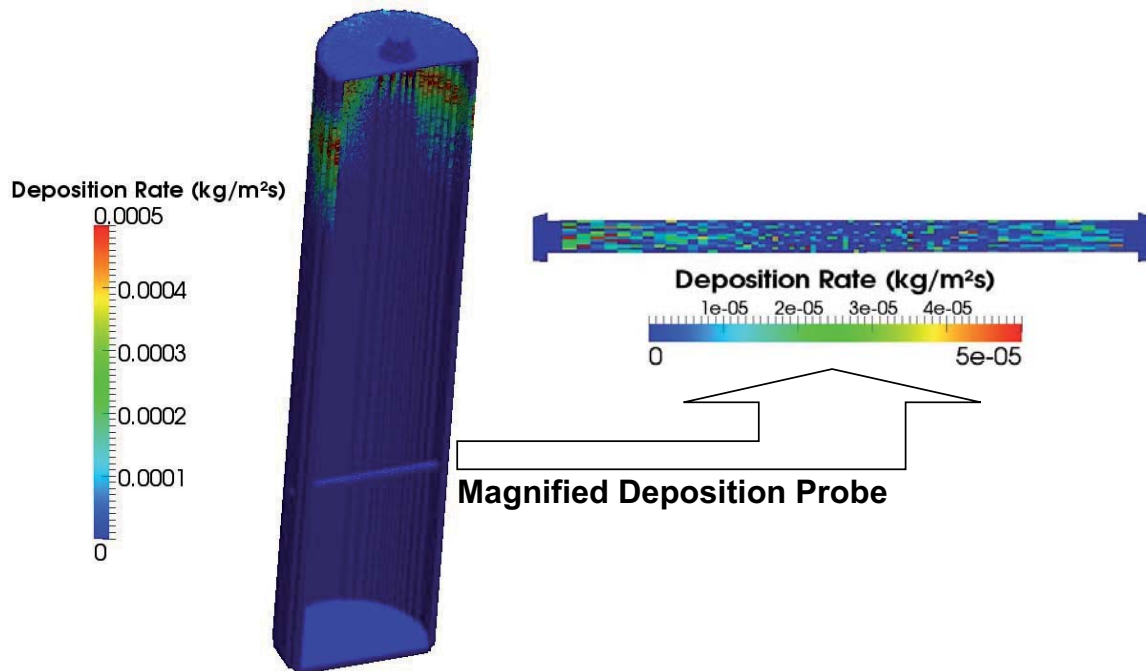
Figure 4.20: Deposition rate on the furnace wall and the deposition probe for coal + 25 % BM3. Please note the different scales of the figures.

Concerning the sticking probability on the deposition probe, a method based on the melting behaviour of the particle and the condensible species as introduced in section 3.4 is utilized. The melting behaviour of the three participating species, i.e. coal particles, biomass particles and the condensible species are considered [2]. With respect to the deposit formation on the deposition probe, condensation is also considered in addition to inertial impaction. From the figure it can be seen that the most severe deposit accumulation may occur on the area near to the burner. This area coincides with the location where most of the particles arrive at the furnace wall for the first time. Based on the temperature profile in Fig. 4.14, peak temperature occurs around this position, and considering the melting behaviour of the particles, a significant amount of melting particles will be found providing a sticky layer for the arriving particles on the furnace wall. However, the deposition rate in this area may be over-predicted. A relatively small particle may not have enough momentum to break a viscous sub-layer to arrive on the wall [91]. If the decrease of the particle size is slower due to delayed char burn-out and/or high ash content of the particles, the error will be relatively small. On the other hand, a model proposed by Wessel and Righi [123] is used to take into account the effect of the viscous layer on inertial impaction near to the cylindrical geometry. With this model, the deposition rate on the probe seems to be obviously lower than that predicted in the near-burner area. One reason for this observation is that the implementation of swirling flow near to the burner may be a limiting factor for a number of particles moving towards the small probe. Another reason

is that the particles do not possess enough momentum to penetrate the viscous layer due to their small size. As mentioned before, the deposition rate on the cooled probe may be greatly affected by the condensible species providing a sticky layer for the arriving particles.
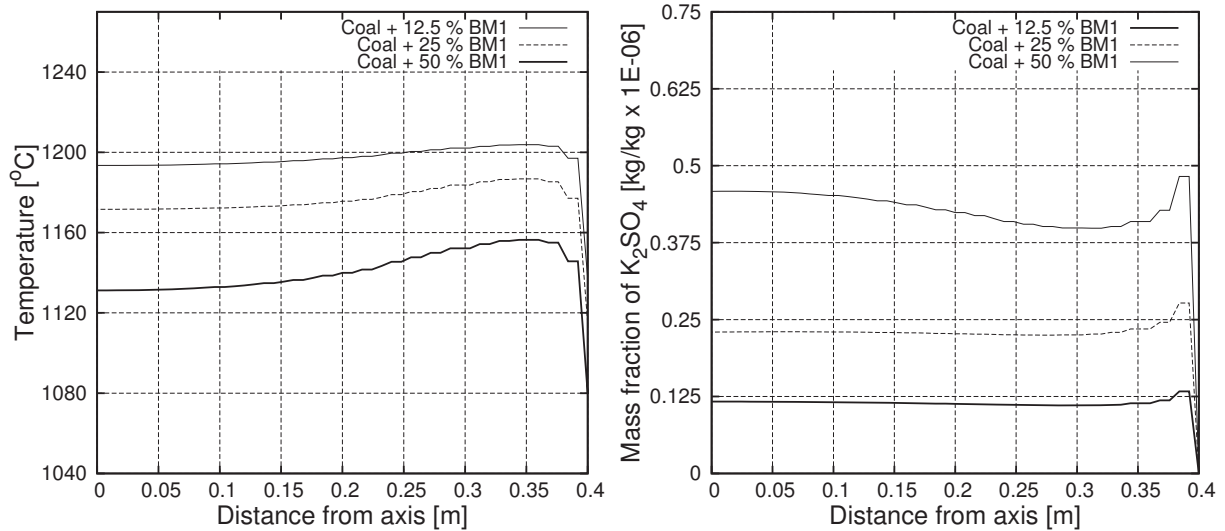

Figure 4.21: Predicted temperature and mass fraction of K_2SO_4 for co-firing BM1 with coal at a distance of 1.16 m from the burner.

The further discussion will focus on the cases of co-firing BM1 with coal. In these cases, the deposition probe is located at a distance of 1.16 m from the burner. Predicted temperature and mass fraction of K_2SO_4 for three different thermal shares of co-firing BM1 with coal at this position are given in Fig. 4.21. By comparison with Fig. 4.18, the temperature variation as well as the mass fraction profile is similar at the same position and the same thermal share. However, the mass fraction of K_2SO_4 of BM3 is around one order of magnitude higher than that of BM1 at this condition. This observation is ascribed to the higher release rate of potassium at the same temperature condition due to the higher content of potassium in BM3. Furthermore, Fig. 4.21 shows that a variation concerning K_2SO_4 profile is obviously observed for coal + 50 % BM1, whereas the profiles are relatively constant for the other thermal shares. This behaviour can be seen also for the temperature profile. It seems that the formation of K_2SO_4 depends on the released potassium in the gas phase, whereas the release rate of potassium is greatly affected by the temperature condition. In this case, potassium in the fuel is modelled to release as potassium chloride which acts as a precursor to the formation of potassium sulfate.

Fig. 4.22 shows the condensation rates in case of co-firing BM1 with coal. Please note that the scale of the figure is applicable for the three condensation rates. It is clearly shown that the rate for coal + 12.5 % BM1 is lower than the rate for the others, whereas the condensation rate for coal + 25 % BM1 is only slightly different from that for coal + 50 % BM1. A relatively low rate for coal + 12.5 % BM1 can be attributed to a very limited concentration of K_2SO_4 in the
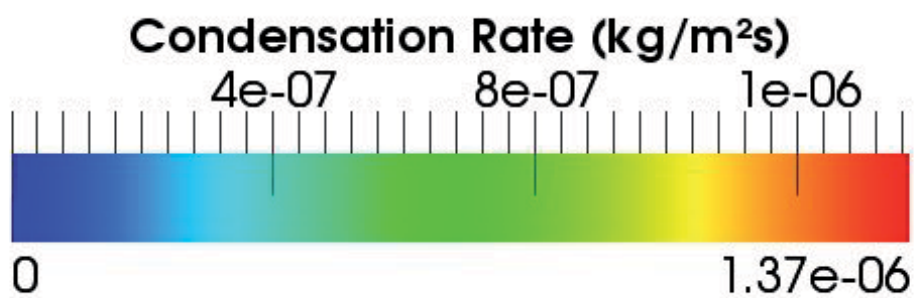
Figure 4.22: Condensation rate predicted with Film theory for three different thermal shares of co-firing BM1 with coal.

gas phase. This is emphasized by the fact that in the computational procedure, the involved species concentrations must be defined as "double precision" variables. Furthermore, the figure shows that the condensation rates vary along the probe where a relatively big variation can be seen for the two highest thermal shares of BM1. This can be attributed to the radial temperature variation at the probe location. The temperature affects the diffusion rate of the condensible species through the boundary layer. However, the radial concentration of K_2SO_4 in the gas phase is not in agreement with the trend of the condensation rate. It seems that this effect is not sensitive to the predicted condensation rate due to a low order of magnitude in the variation (see Fig. 4.21). The partial pressure of K_2SO_4 at a phase transition is calculated by means of the Clausius-Clapeyron equation (see Appendix A.2), afterwards the concentration gradient of the condensible species is obtained accordingly. It can be concluded that the cooling process from a higher temperature will lead to a higher condensation rate if the system is investigated at the same initial condition concerning the species concentration.

The effect of deposit formation on the temperature increase of the deposition probe can be seen in Fig. 4.23. Similar to the deposition rate shown in section 4.1.3, the temperatures shown in the figure are the averaged temperatures over the circumference of the probe for every position along the probe. As mentioned before, the probe is cooled by air to maintain the probe temperature similar to typical superheater temperatures in a utility boiler. For all cases, the surface temperature of the probe at initial condition is assumed to be 650 $°C$. The figure shows the predicted temperature profile along the probe for several time steps. In the course of time, the temperature increases as the deposit thickness increases. As mentioned before, the probe is located at a distance of 1.16 m from the burner in case of co-firing BM1 with coal. At this location, the temperature increase is more concentrated at the borders of the probe. As shown in the particle trajectories (see Fig. 4.19), particle arrivals are also more concentrated at these locations. Please note that the particle trajectories shown in Fig. 4.19 are for co-firing BM3 with coal, however, the same behaviour may be expected also for co-firing BM1 with coal. In addition, these positions are identified as the locations with higher condensation rate (see Fig. 4.22). In order to reduce the computational effort for this study, it was assumed that the variables such as the temperature field, species concentration, and velocity field are constant. This assumption will be a failure to apply if there is an extreme deposit formation affecting the flow behaviour of the fluid in the furnace during that time period. An additional error will arise also if the physical properties of the deposit layer change significantly at a very short time period. Those deficiencies will be the great challenges that should be handled in future work. A closer look on Fig. 4.23 reveals that the temperature increase for coal + 25 % BM1 is slightly higher than that for coal + 50 % BM1. A reason for this is that the fraction of melting particles may be higher for lower thermal shares of BM1 which leads to the higher sticking probability of the particles on the deposit surface. Furthermore, the temperature increase for co-firing BM3 with coal is lower than that for co-firing BM1 with coal due to a lower deposition
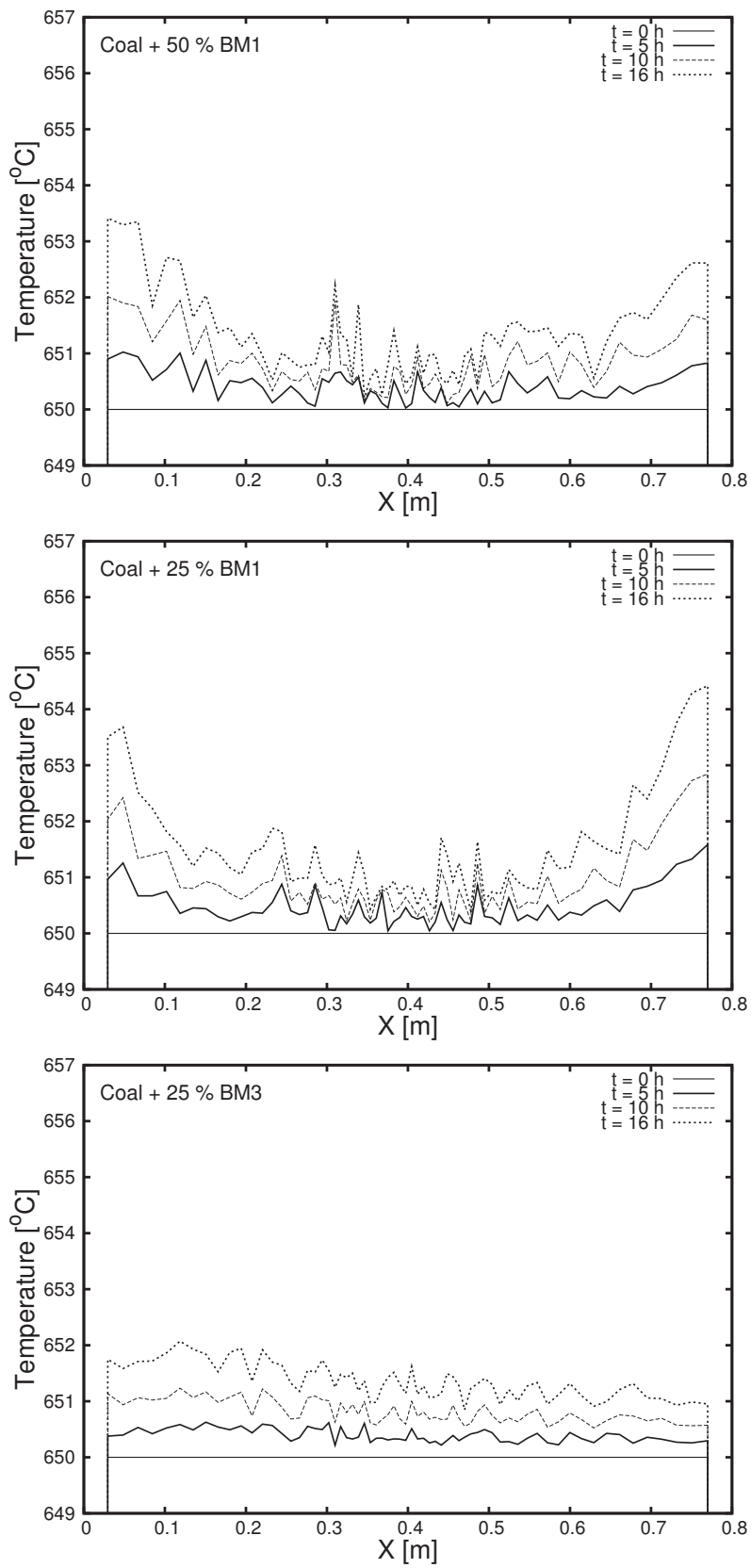
Figure 4.23: Temperature changes of the deposition probe as an effect of deposit formation.

rate. Remember that the probe is located further downstream at a distance of 2.67 m from the burner for the coal $+$ BM3 case. As shown in Fig. 4.17 and Fig. 4.18, the temperature and the condensation rate are uniformly distributed along the probe. The contribution of the particle melt fraction to the sticking probability at this location is negligible due to the low particle temperature.

It can seen also from the Fig. 4.23 that the increase of temperature for all cases is relatively small after 16 h. In case of co-firing BM1 with coal, the maximum temperature increase occurring at the borders of the probe is around 4 $^{\circ}C$, whereas that for co-firing BM3 with coal is around 2 $^{\circ}C$. For co-firing BM3 with coal, the deposition rate of particles is in the order of 10^{-5} $kg\,m^{-2}\,s^{-1}$, whereas the condensation rate is in one order of magnitude lower. Based on this observation, it seems that particle deposition becomes the major contributor to the formation of the deposit layer. Another evidence is that the increase of temperature along the probe is not distributed homogeneously on the contrary to the distribution of the condensation rate along the probe (see Fig. 4.18). The increase of temperature may be two times higher at the borders of the probe compared to that at certain positions in the middle of the probe. The contribution of particles on deposit formation may be significantly higher in case of co-firing BM1 with coal. However, the condensible species may still play a dominant role in terms of providing a sticky layer to arriving particles. In terms of deposition mechanism, thermophoresis has been also taken into account for the particle arrival rate. However, this mechanism has a very small contribution to the deposit formation due to a low temperature gradient near to the probe location in case of co-firing BM3 with coal.
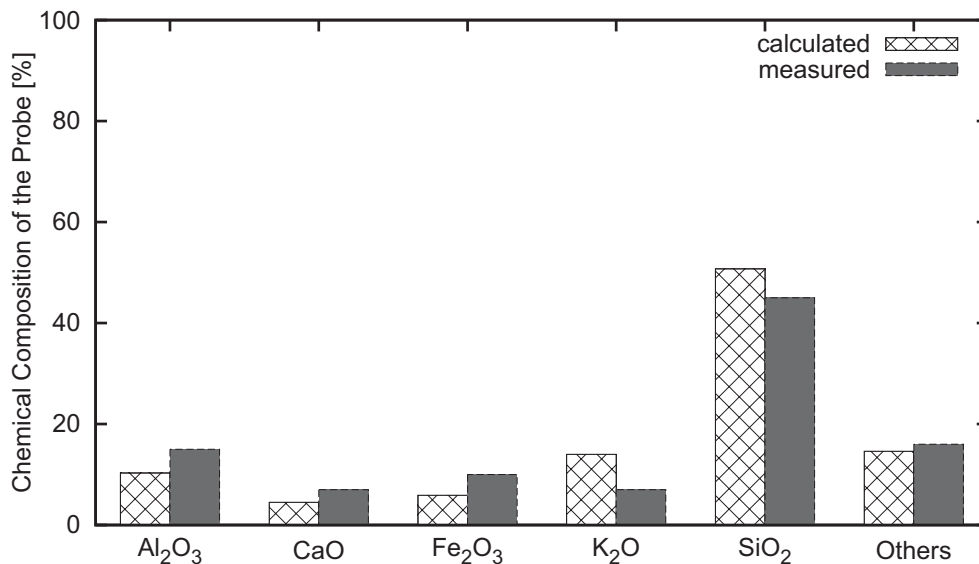

Figure 4.24: Composition of deposit ash on the probe for co-firing 25 % BM3 with coal.

Fig. 4.24 shows the chemical composition of deposit ash on the probe. The comparison between the predicted and the measured composition is made in order to validate the deposition model. In this case, the chemical composition of the probe obtained for co-firing BM3 with coal is utilized. From these results, good agreement is generally observed for all species. A quite big discrepancy is found with respect to the composition of condensible species which is presented as K_2O. This result can be attributed to the over-prediction of the condensation rate. The rate predicted by film theory is affected by the availability of K_2SO_4 concentration in the gas phase. In the model, K_2SO_4 in the gas phase acts as precursor of the condensible species. K_2SO_4 may condense homogeneously, and the condensed K_2SO_4 may serve also as condensation nuclei for KCl condensation in the boundary layer before condensing via direct condensation. The submicron particles will be transported to the deposition probe by thermophoresis instead of gas diffusion. It has been reported in the work of Hansen [39] that thermophoresis is a slower transport mechanism than gas diffusion modelled by the film theory. On the other hand, the ash particles may undergo complex transformation during combustion [56]. The chemical composition of ash obtained from fuel analysis (Table 4.4) may differ significantly to either the fly ash or the ash deposit composition. In this work, the composition of the arriving particles on the probe is obtained based on the composition of ash collected on slagging probe. This ash is collected using an uncooled probe at the same position as the deposition probe. This assumption may be applicable if there is no significant transformation of particle composition during the cooling process near to the deposition probe. The compositions of ash collected on the slagging probe for the BM3 particles as well as the coal particles are shown in Table.4.8. The compositions are obtained in case the fuels are fired with 100 % thermal shares, respectively. Please note that the compositions have been normalized to 100 %.

Table 4.8: Composition of the fuel ash and of the ash collected on the slagging probe

Component	Coal		BM3	
	Fuel analysis (%)	Slag. ash (%)	Fuel analysis (%)	Slag. ash (%)
SiO_2	45.31	46.15	73.68	79.0
Al_2O_3	26.67	24.62	0.43	2.0
CaO	6.21	5.13	4.62	4.0
Fe_2O_3	15.03	16.92	0.32	1.0
Others	6.51	7.17	20.94	14

From the table, only marginal difference is found between ash composition from fuel analysis and that from ash collected on the slagging probe for both fuels. Similar to the ash composition from fuel analysis, the major species of ash collected on the slagging probe for coal is made

up by SiO_2, Al_2O_3, and Fe_2O_3, whereas the ash collected on the slagging probe for BM3 is dominated by SiO_2. Furthermore, a simulation run has been performed also by using the ash composition from fuel analysis as input data, and the result is compared to the ash composition from Fig. 4.24 as shown in Table 4.9. The most remarkable effect of the utilization of fuel ash is the decrease in composition for some major species such as SiO_2, Al_2O_3, CaO and the increase in composition for other species such as Fe_2O_3 and K_2O. The predicted deposition indicates that most of the deposited particles are minerals derived from the coal particles. A higher SiO_2 content of deposit ash may be attributed to the effect of deposited BM3 particles with a high content of silica. The biomass particles have a relatively large size initially, however the particle diameter will decrease quickly due to the high volatile content of the biomass. Most of the particles will be carried by the secondary air to stick on the furnace wall. Co-firing BM3 with only 25 % thermal share may also an additional reason to the small contribution of biomass particles on the composition of the probe deposit.

Table 4.9: Predicted deposit composition from different input data

Component	Input data	
	Fuel ash	Slag. ash
SiO_2 (%)	50.4	50.7
Al_2O_3 (%)	9.4	10.3
CaO (%)	4.0	4.5
Fe_2O_3 (%)	6.5	5.9
K_2O (%)	14.6	14.0
Others (%)	15.1	14.6

Information about the melting behaviour of the participating species on deposit formation are required in the prediction of the sticking probability. In this work, the ash melting behaviour of ash collected on the slagging probe is used based on the work of Heinzel [42]. Regarding the melting behaviour of coal particles, the fraction of melt is estimated to increase linearly from zero to one as the temperature increases from 1200 $°C$ to 1300 $°C$. The BM3 particles are assumed to melt in the temperature range from 900 to 1100 $°C$ with a linear increase of the melt fraction. Afterwards, the sticking probability of the particles is related to the melt fraction as illustrated in Fig. 3.11. In this case, the melting behaviour is analysed for the temperature of the arriving particles. Furthermore, the melting behaviour of deposit surface is calculated as the function of surface temperature and deposit composition analog to equation 3.63. The melt fraction of each deposited species is evaluated at the surface temperature. In addition, the condensible species (K_2SO_4) is assumed to be fully in molten phase at the surface temperature.
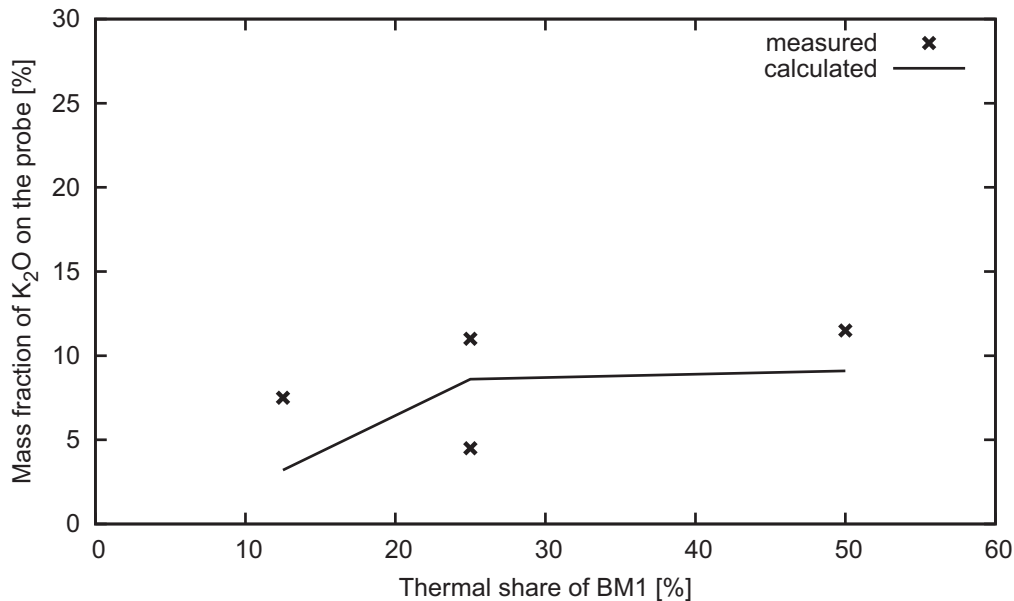
Figure 4.25: Potassium content of the deposition probe for co-firing BM1 with coal.

For sake of further validating the deposition models developed and implemented in the combustion simulation code AIOLOS, another experimental data set regarding the potassium content on the deposition probe is used [42]. Fig. 4.25 shows the measured and the predicted potassium content on the probe for different thermal shares of BM1. From these results, good agreement is found with respect to the trend of the potassium content increase related to the increase of the thermal share of biomass. However, the predicted values at the 12.5 % and 50 % thermal share of BM1 lie slightly below the experimental data. This is attributed to the release rate of potassium to the gas phase. As mentioned before, the release rate for biomass is assumed similar to the release rate of low rank coal. A difference in ash content may affect the behaviour of ash elements in controlling the potassium release. This has been experimentally studied by Novakovic et al. [75]. For the thermal share of 25 % BM1, there are two experimental values with respect to the potassium content obtained from different depths or different positions within the deposit layer. When preparing one joint sample from the surface of the tube, the operators took as much as possible ash samples from the tube. In addition, the specific individual values from the bulk ash sampling shall always be analysed in a statistical way and the analysis curves are considered as qualitative trends [43]. The upper limit may refer to the value at the initial stage of the deposit build-up. The predicted value is the average composition from all layers after 16 h which means that it should lie more or less in the middle of both values. These observations imply that the condensation rate is over-predicted for this thermal share. It can be related to the importance of aerosol formation which is not considered

in the present work. As mentioned before, a higher temperature gradient may imply a higher saturation ratio resulting in increasing aerosol formation which is not taken into account in this work. This observation is similar to what is found for coal $+$ 25 % BM3. This effect is not observed in 50 % thermal share due to the lower temperature gradient and in 12.5 % thermal share due to the low K_2SO_4 concentration in the gas phase.

4.2.2 Summary

In this section, simulation of deposit formation for coal-fired boilers with biomass co-combustion has been performed. Various simulation results with respect to the co-fired biomass type and the biomass thermal share were discussed and evaluated against the experimental data sets published by Heinzel [42]. The experimental work was conducted on the 0.5 MW semi-industrial pulverized-fuel combustion facility of IFK. The simulation runs were performed in two steps, simulation of the combustion process in the first step (basic simulation), and the simulation of deposit formation in the second step. In terms of the basic simulation, the temperature profile along the axis is found to be in agreement with the experimental data. The major discrepancy is most remarkable at the peak temperature due to a difficulty to determine the swirling factor of the injected secondary air.

In this study, two condensation models have been compared and discussed in terms of their applicability to the prediction of fouling phenomena in coal-fired utility boilers with biomass co-combustion. In general, the condensation rate calculated by film theory is five orders of magnitude lower than that calculated by Goldbrunner's model. By using Goldbrunner's model, the deposit composition is dominated by the condensible species which is far from reality based on the investigated cases. Hence, the film theory model was utilized to describe the condensation of K_2SO_4 on the deposition probe. The deposition probe is located at a distance of 2.67 m from the burner for co-firing BM3 with coal, and at a distance of 1.16 m from the burner for co-firing BM1 with coal. It is obvious that the condensation rate profile of co-firing BM3 differs from that of co-firing BM1 due to the different thermal behaviour near to the probes. Furthermore, it was shown that the film theory model is able to predict the condensation rate in the superheater section of utility boilers. However, some deviations between experiment and predictions have been found. This is attributed to the significant effect of aerosol formation which is not considered in the current work.

5 Conclusions and Outlook

5.1 Conclusions

The main objective of the present work is the modelling of deposit formation for coal-fired boilers with biomass co-combustion. In particular, the focus has been on the release of alkali and its effect on the deposit build-up. The models were integrated into the 3D combustion simulation code AIOLOS, developed at the Institute of Combustion and Power Plant Technology (IFK) at University of Stuttgart since the late 1970s. In the present work, the deposit formation models were implemented in a post-processing step. First, a basic simulation run involving the release of potassium species has to be performed, supplying flow, temperature, and the species concentration fields. Then, large numbers of particles are tracked through the furnace until they touch and eventually stick to the surface, or they simply leave the furnace through an outlet. Data calculated in the preceding basic simulation, e.g., concentrations of solids and gas phase properties are used as input data for actual deposit formation models.

Concerning the alkali release, the heterogeneous reactions as well as the homogeneous reactions are considered in the present work. The heterogeneous reactions are divided into the primary step of alkali release and the secondary reaction between the released alkali and the aluminosilicate in the fly ash. The primary step is modelled based on the work of Steffin [104], whereas the secondary reaction is modelled analogue to the char burn out model implemented in AIOLOS. Furthermore, the homogeneous reactions are modelled based on the reaction mechanism proposed by Srinivasachar [103] for the sodium-chlorine system. The same mechanism is implemented also for the potassium-chlorine system. The reaction kinetics and thermodynamical databases for potassium were taken from the work of Glarborg [30]. A global model proposed by Tomeczek [111] is used to describe the sulfation of the released alkali. The interaction between turbulence and chemistry for the homogeneous reactions in the gas phase is modelled by the Eddy Dissipation Concept (EDC). Furthermore, a global model for the homogeneous reactions is proposed as a simplification of the detailed model of Srinivasachar. To evaluate the validity of the global model, the results were compared to the ones obtained by the model of Srinivasachar.

In terms of deposit formation, the effect of alkali on the sticking probability of the arriving ash particles and the contribution of the released alkali to the deposit layer are modelled. Two

major deposition mechanisms are taken into account in the model, i.e. inertial impaction for the pulverized fuel particle and condensation for the released alkali. Inertial impaction on the cylindrical geometry is based on the model proposed by Wessel and Righi [123]. In order to obtain a first impression about the effect of condensible alkali on the deposition process, a condensation model by Hansen [39] is used, whereas the more complex models, i.e. Film theory and Goldbrunner's Model are used to investigate the deposit formation in the co-firing biomass systems. In order to take into account the sticking probability of the arriving particle on the surfaces, the melt fraction based sticking concept was implemented into AIOLOS. A heat transfer model considering the physical properties of deposit has been also included in this work to describe the effect of deposit formation on the temperature increase of the deposit surface.

For the sake of validating the models, simulation runs were performed on the entrained flow combustion reactor and on the semi-industrial pulverized-fuel combustion facility at the Institute of Combustion and Power Plant Technology of Stuttgart University. The results are compared to the experimental data and the main findings are summarized as follows:

- The results of sodium release are found in agreement with the experimental data for short residence times. However, a slight discrepancy can be observed for the higher residence time. This implies that the released sodium into the gas phase may be over-predicted at a higher residence time. For the residence times in the furnace of a typical pulverized coal fired utility boiler, the model predicts well the sodium release with an acceptable error.

- In terms of the homogeneous reactions of the released alkali species, the results obtained by the global model are in good agreement with the detailed model of Srinivashachar. The use of the global model can significantly reduce the computational effort when simulations with a large number of grid points are to be performed.

- The rate of alkali sulfation is relatively low for the case under investigation. The sodium sulfate concentration is found to be higher at a higher residence time.

- Simulations of potassium release with different alkali to chlorine ratios have been also conducted. In this case, the effect of the secondary reaction is neglected due to either the low content of ash in the fuel or the low residence time. In general, the results are in good agreement with the experimental findings. However, it seems that the reaction rate which is appropriate for a specific type of coal may not be applicable for another type of coal.

- In case of a biomass-fired boiler, the condensible KCl on the deposition probe has a significant effect on the deposition rate especially at the initial stage of deposit build-up.

- In case of co-combustion experiments with 75 % coal and 25 % biomass, the condensation rate calculated by the film theory is five orders lower than that calculated by Goldbrunner's model. Based on this observation, the film theory model was utilized to describe the condensation of K_2SO_4 on the deposition probe.

- In general, the simulation results are found in good agreement with the experimental data except for a co-combustion experiment with a thermal share of 25 % biomass. In this case, the potassium content on the deposition probe is slightly over-predicted. This can be attributed to the significant effect of aerosol formation which is not considered in the current work. In addition, ash stemming from the coal particles is the dominant species for all co-firing cases due to their higher deposition rate on the probe.

5.2 Model improvement and perspectives

This work focuses on the deposit formation occurring typically on the superheaters of utility boilers. In order to obtain a better prediction of the effect of deposit formation in the convective heat exchanger region, the following tasks are suggested as future work.

- Mineral matter in the fuel particles undergoes complex chemical and physical transformation towards the deposit surface. As a result, the chemical composition and the physical properties of the ash particles have a big influence on the sticking probability as well as the thermal behaviour of the deposit layer. Future work should address mechanistic models to predict these processes.

- The mineral composition may influence significantly the behaviour of alkali release during coal combustion. A more sophisticated model that takes into account this effect should be developed in future work.

- The formation and coagulation of aerosols near to the superheater with a high temperature gradient has a pronounced effect on the local deposition rates as well as the chemical composition of the deposit. To improve predicted deposit accumulation rates, this mechanism is suggested to be dealt with in further work.

- In case the deposit build-up occurs quickly, the temperature increase of the deposit surface will be relatively high. Furthermore, various layers will be formed with a big difference in thermal and physical properties. A model taking into account the effect of different layers on the heat transfer process should be developed.

- In this work, experimental data have been used which were obtained by inserting a deposition probe into a semi-industrial pulverized-fuel combustion facility simulating the

deposit build-up on the superheater tubes. Further work should address the question if the developed models are able to predict the phenomena occurring in the multi-tube arrangement of the superheater section in industrial utility boilers.

- In order to validate the prediction model more comprehensively, exploiting available data bases on full and pilot scale experiments should also be a major issue of future work. More detailed experimental data are required in terms of the temperature increase and the temperature distribution on the deposit surface.

A Appendix

A.1 Mechanism for Alkali Reactions

The kinetics of the reactions are calculated according to the Arrhenius expression which is written as:

$$k_i = k_{0,i} \, T^n \, exp(-E/\Re T)(cm^3/mol \, s) \tag{A.1}$$

Table A.1: Reaction rate coefficients for the Na-Cl system [103]

No.	Reaction	$k_{0,i}$	n	$E \, (cal/mol)$
1.	$NaOH + HCl \rightarrow NaCl + H_2O$	1.70E14	0	0
2.	$NaCl + H_2O \rightarrow NaOH + HCl$	5.94E09	0	0
3.	$Na + HCl \rightarrow NaCl + H$	1.20E15	0	8000
4.	$NaCl + H \rightarrow Na + HCl$	1.82E13	0	800
5.	$Na + Cl + M \rightarrow NaCl + M$	1.10E20	-1	0
6.	$NaCl + M \rightarrow Na + Cl + M$	4.17E19	-1	96400
7.	$NaO + HCl \rightarrow NaCl + OH$	1.70E14	0	0
8.	$NaCl + OH \rightarrow NaO + HCl$	4.93E09	0	0
9.	$H + HCl \rightarrow H_2 + Cl$	4.86E12	0	3179
10.	$H_2 + Cl \rightarrow H + HCl$	5.20E12	0	5700
11.	$H + Cl_2 \rightarrow Cl + HCl$	8.40E13	0	1152
12.	$Cl + HCl \rightarrow H + Cl_2$	3.72E13	0	47862
13.	$Cl + Cl + M \rightarrow Cl_2 + M$	7.20E14	0	-1800
14.	$Cl_2 + M \rightarrow Cl + Cl + M$	4.00E15	0	55050
15.	$O + HCl \rightarrow Cl + OH$	6.92E12	0	6700
16.	$Cl + OH \rightarrow O + HCl$	5.20E12	0	5700
17.	$OH + HCl \rightarrow Cl + H_2O$	7.80E12	0	0
18.	$Cl + H_2O \rightarrow OH + HCl$	5.78E13	0	16000

Table A.2: Reaction rate coefficients for the K/O/H system [30]

No.	Reaction	$k_{0,i}$	n	$E/\Re$
1.	$KOH + H \leftrightarrow K + H_2O$	5.00E13	0	0
2.	$K + O_2 \leftrightarrow KO_2 + M$	3.60E14	0	0
3.	$KO_2 + H \rightarrow KO + OH$	5.60E13	0	0
4.	$KO + H_2O \leftrightarrow KOH + OH$	1.3E14	0	800

Table A.3: Reaction rate coefficients for the K-Cl system [30]

No.	Reaction	$k_{0,i}$	n	$E/\Re$
1.	$KOH + HCl \leftrightarrow KCl + H_2O$	1.70E14	0	0
2.	$K + HCl \leftrightarrow KCl + H$	9.10E12	0	594
3.	$K + Cl + M \leftrightarrow KCl + M$	1.80E20	-1	0
4.	$KO + HCl \leftrightarrow KCl + OH$	1.70E14	0	0
5.	$H + HCl \leftrightarrow H_2 + Cl$	4.90E12	0	1599.90
6.	$H + Cl_2 \leftrightarrow Cl + HCl$	8.40E13	0	579.90
7.	$Cl + Cl + M \leftrightarrow Cl_2 + M$	7.20E14	0	-905.89
8.	$O + HCl \leftrightarrow Cl + OH$	6.90E12	0	3371.92
9.	$OH + HCl \rightarrow Cl + H_2O$	7.80E12	0	0

A.2 Equilibrium Condensation

The mole fraction of K_2SO_4 at the phase interface can be related to the saturation partial pressure, written as:

$$\psi_{K_2SO_4,s} = \frac{p_{s,K_2SO_4}}{p_{tot}}$$ (A.2)

In order to calculate the saturation partial pressure, the Clausius-Clapeyron equation is utilized in the present work, written by:

$$log\left(\frac{p_2}{p_1}\right) = \frac{\Delta H_v}{2.303 \cdot \Re} \cdot \left(\frac{T_2 - T_1}{T_1 \cdot T_2}\right)$$ (A.3)

The subscripts "1" and "2" denote the properties at the phase interface and at the gas state, respectively. The temperature at the phase interface is set equal to the deposit surface temperature. This assumption may be applicable if the film thickness is relatively small. Furthermore, the calculation of ΔH_v is based on the following equation:

$$\Delta H_v = \Delta G + T \cdot \Delta S$$ (A.4)

To determine ΔG and ΔS, the FactSage compound database 2009 [25] can be used, and the properties for K_2SO_4 are listed in Table A.4.

Table A.4: Thermal properties for the phase change of K_2SO_4 (FactSage 2009)

Temperature $T[K]$	Enthalpy ΔG $[J/mol]$	Entropy ΔS $[J/mol\ K]$
298.15	253786.41	154.53
300.00	253501.61	154.39
400.00	238474.46	147.32
500.00	224090.53	141.32
600.00	210281.92	135.60
700.00	197053.41	129.60
800.00	184445.30	123.13
900.00	171953.19	116.70
1000.00	160566.65	111.16
1100.00	149699.47	106.28
1200.00	139292.32	101.94
1300.00	129298.18	98.01
1400.00	119678.90	94.43
1500.00	110402.93	91.14
1600.00	101443.71	88.09
1700.00	92778.58	85.25
1800.00	84388.00	82.59
1900.00	76254.89	80.10
2000.00	68364.25	77.74
2100.00	60702.74	75.51
2200.00	53258.46	73.39
2300.00	46020.71	71.38
2400.00	38979.80	69.45
2500.00	32126.94	67.62

Bibliography

[1] AKBAR, S.; SCHNELL, U.; SCHEFFKNECHT, G.: Modelling Potassium Release and the Effect of Potassium Chloride on Deposition Mechanisms for Coal and Biomass-Fired Boilers. In: *"Combustion Theory and Modelling"* 14 (2010), pp: 315–329

[2] AKBAR, S.; SCHNELL, U.; SCHEFFKNECHT, G.: Numerical Simulation of Deposit Formation on Superheaters of Coal-Fired Boilers with Biomass Co-Combustion. In: *"9th Europ. Conference on Industrial Furnaces and Boilers, Estoril, Portugal, 26-29 April"* (2011)

[3] AKSOY, H.; CHEN, C.S.: Numerical Solution of Navier-Stokes Equations with Non-Staggered Grids using Finite Analytic Method. In: *"Numer. Heat Transfer, Part B"* 21 (1992), pp: 287–306

[4] ANANY, M. N.; SCHNELL, U.; SCHEFFKNECHT, G.: Implementation of A Smoothing Pressure Correction Approach to the Pressure-Correction Equation in order to Maintain the Use of SIMPLEC Algorithms on Non-Staggered Grids. In: *"Progress in Computational Fluid Dynamics"* 10 (2010), pp: 40–50

[5] BASSILAKIS, R.; ZHAO, Y.; SOLOMON, P.R.; SERIO, M.A.: Sulfur and Nitrogen Evolution in the Argonne Coals - Experiment and Modelling. In: *"Energy & Fuels"* 7 (1993), pp: 710–720

[6] BAXTER, L. L.: Ash Deposition during Biomass and Coal Combustion: A Mechanistic Approach. In: *"Biomass and Bioenergy"* 4 (1993), pp: 85–102

[7] BAXTER, L. L.: Ash Deposit Formation and Property Development. In: *"Course notes, Nordic Ash Seminar"* (1998)

[8] BAXTER, L.L.; MILES, T.; JENKINS, B.: *Alkali Deposits Found in Biomass Boilers*. National Renewable Energy Laboratory, 1999

[9] BENSON, S. A.; JONES, M. L.; HARB, J. N.: Ash Formation and Deposition. In: *"LD Smoot (Ed.), Fundamentals of Coal Combustion for Clean and Efficient Use"* (1993)

[10] BIRD, R. B.; STEWART, W.E.; LIGHTFOOT, E.N.: *Transport Phenomena, second edition*. John Wiley & Sons, Inc., 2002

[11] BOOW, J.; GOARD, P. R. C.: Fireside Deposits and their Effect on Heat Transfer in a Pulverized Coal Fired Boiler, Part 3 - The Influence of the Physical Characteristics of the Deposit on its Radiant Emittance and Effective Thermal Conductance. In: *"Journal of the Institute of Fuel"* 44 (1969), pp: 412

[12] BOTTERILL, J. S. M.; SALWAY, A. G.; TEOMAN, Y.: The Effective Thermal Conductivity of High Temperature Particulate Beds (Part 2). In: *"Int. J. Heat & Mass Transfer"* 32 (1989), pp: 585

[13] BRAILSFORD, A. D.; MAJOR, K. G.: The Thermal Conductivity of Several Phases, Including Porous Materials. In: *"Brit. J. Appl. Phys."* 15 (1964), pp: 313–319

[14] CASTILLO, J.L.; ROSNER, D.E.: A Nonequilibrium Theory of Surface Deposition from Particle-Laden, Dilute, Condensible Vapor-Containing, Laminar Boundary Layers. In: *"International Journal of Multiphase Flow"* 14 (1988), pp: 99–120

[15] CHRISTENSEN, K.A.; LIVBJERG, H.: A Plug Flow Model for Chemical Reactions and Aerosol Nucleation and Growth in an Alkali-Containing Flue Gas. In: *"Aerosol Science and Technology"* 33 (2000), pp: 470–489

[16] COUCH, G.: *Understanding Slagging and Fouling in PF Combustion*. IEA Coal Research, London, 1994

[17] CROWE, C.T.; SHARMA, M.P.; STOCK, D.E.: The Particle Source-in-Cell (PSI-Cell) Model for Gas-Droplet Flows. In: *"Trans. ASME, J. Fluids Eng."* 99 (1997), pp: 325

[18] DATE, A. W.: Complete Pressure Correction Algorithm for the Solution of Incompressible Navier-Stokes Equations on a Non-Staggered Grid. In: *"Numerical Heat Transfer"* 29 (1996), pp: 441–458

[19] DAVIDSSON, K.O; ENGVALL, K.; HAGSTROM, M.; KORSGREN, J.G.; LONN, B.; PETTERSSON, J.B.C.: A Surface Ionization Instrument for On-Line Measurements of Alkali Metal Components in Combustion: Instrument Description and Applications. In: *"Energy & Fuel"* 16 (2002), pp: 1369–1377

[20] DAVIDSSON, K.O; KORSGREN, J.G.; PETTERSSON, J.B.C.; JAGLID, U.: The Effects of Fuel Washing Techniques on Alkali Release from Biomass. In: *"Fuel"* 81 (2002), pp: 137–142

[21] DAVIDSSON, K.O; STOJKOVA, B.J.; PETTERSSON, J.B.C.: Alkali Emission from Birchwood Particles during Rapid Pyrolysis. In: *"Energy & Fuel"* 16 (2002), pp: 1033–1039

[22] DEEG, C.; SCHNEIDER, M.; SCHNELL, U.; SCHEFFKNECHT, G.: A Method for Modelling the Co-Combustion of Solid Recovered Fuels in Pulverized Fuel Power Plants. In: *"VDI-Berichte"* 1988 (2007), pp: 345–354

[23] EDGECOMBE, L.: The State of Combination of Chlorine in Coal. Extraction of Coal with Water. In: *"Fuel"* 35 (1956), pp: 1033–1039

[24] EYK, P. J.; ASHMAN, P. J.; NATHAN, G. J.: Mechanism and Kinetics of Sodium Release from Brown Coal Char Particles during Combustion. In: *"Combust. Flame, doi: 10.1016/j.combustflame.2011.05.005"* (2011)

[25] FACTSAGE2009: Facility for the Analysis of Chemical Thermodynamics. In: *"http://www.crct.polymtl.ca/fact"* (2009)

[26] FAN, F.; AHMADI, G.: A Sublayer Model for Turbulent Deposition of Particles in Vertical Ducts with Smooth and Rough Surfaces. In: *"J. Aerosol Science"* 24 (1993), pp: 45

[27] FOERTSCH, D.: *A Kinetic Model of Pulverized Coal Combustion for Computational Fluid Dynamics*. Stuttgart University, 2003

[28] FOERTSCH, D.; KLUGER, F.; SCHNELL, U.; SPLIETHOFF, H.; HEIN, K.R.G: A Kinetic Model for the Prediction of NO Emission from Staged Combustion of Pulverized Coal. In: *"Proceedings of the Combustion Institute"* 27 (1998), pp: 3037–3044

[29] GAUS-LIU, X.: *High-Temperature Chlorine Corrosion during Co-Utilization of Coal with Biomass or Waste*. Cuvillier Verlag Goettingen, 2008

[30] GLARBORG, P.; MARSHALL, P.: Mechanism and Modelling of the Formation of Gaseous Alkali Sulfates. In: *"Combustion and Flame"* 141 (2005), pp: 22–39

[31] GLAZER, M.P.: *Alkali Metals in Combustion of Biomass with Coal*. Delft Institute of Technology, 2007

[32] GODBEE, H. W.; ZIEGLER, W. T.: Thermal Conductivities of MgO, Al_2O_3, ZrO_2 Powders to 850 °C - Part 2. In: *"Theoretical J. Appl. Phys."* 37 (1966), pp: 55

[33] GOLDBRUNNER, M.: *Lokale Phaenomene bei der Kondensation von Dampf in Anwesenheit eines nichtkondensierbaren Gases*. TU Muenchen, 2003

[34] GREFFRATH, F.; SCHERER, V.; WIRTZ, S.; BOHNES, S.: Untersuchung der spektralen Emissionskoeffizienten und der Temperaturleitfaehigkeit von Aschen und Ablagerungen aus Kohlefeuerungen. In: *"VDI-Berichte"* 2056 (2009)

[35] GUPTA, R. P.; WALL, T. F.: The Thermal Conductivity of Ash Deposits: Particulate and Slag Structures. In: *"Proc. of the EF Conference, Kona, Hawaii"* (1997)

[36] GUPTA, R. P.; YAN, L.; GUPTA, S. K.; WALL, T. F.: Impact of Minerals and Macerals in Coal on Thermal Performance of PC Fired Boilers. In: *"Proc. of the EF Conference, Park City, USA"* (2000)

[37] HALD, P.: *Alkali Metals at Combustion and Gasification Equilibrium Calculations and Gas-Phase Measurings*. Technical University of Denmark, 1994

[38] HAN, X.: *Modelling and Simulation of SOx and NOx Reduction Processes in Pulverized Coal Furnaces*. Cuvillier Verlag Goettingen, 2003

[39] HANSEN, L.A.: *Melting and Sintering of Ashes*. Tekst & Tryk A/S Denmark, 1998

[40] HARLOW, F. H.; WELSH, J. E.: Numerical Calculation of Time Dependent Viscous Incompressible Flow with Free Surface. In: *"Phys. Fluids"* 8 (1965), pp: 2182–2189

[41] HEIN, K. R. G.; HEINZEL, T.; KICHERER, A.; SPLIETHOFF, H.: Deposit Formation during the Co-Combustion of Coal-Biomass Blends. In: *"Proc. of an Engineering Foundation conference on Applications of Advanced Technology to Ash-Related Problems in Boilers, Waterville Valley, New Hampshire"* (1995)

[42] HEINZEL, T.: *Ascheseitige Probleme bei der Mitverbrennung von Biomasse in Kohlenstaubfeuerungen*. Shaker Verlag, 2004

[43] HEINZEL, T.: Personal Communication. (2010)

[44] HELBLE, J.J.; NEVILLE, M.; SAROFIM, A.F.: Aggregate Formation from Vaporized Ash during Pulverized Coal Combustion. In: *"Twenty-First Symposium (International) on Combustion"* (1986), pp: 411–417

[45] HOPPE, A.: *Einfluss der Alkalien bei der Ansatzbildung in Kohlenstaubfeuerungen*. Der Andere Verlag, 2005

[46] HUFFAMAN, G.; HUGGINS, F.; SHAH, N.; SHAH, P.: Behaviour of basic elements during coal combustion. In: *"Prog. Energy Combust. Science"* 16 (1990), pp: 243–251

[47] IISA, K.; LU, Y.: Sulfation of Potassium Chloride at Combustion Conditions. In: *"Energy & Fuels"* 13 (1999), pp: 1184–1190

[48] JENSEN, J.R.; NIELSEN, L.B.; SCHULTZ-MOELLER, C.; WEDEL, S.; LIVBJERG, H.: The Nucleation of Aerosols in Flue Gases with a High Content of Alkali - A Laboratory Study. In: *"Aerosol Science and Technology"* 33 (2000), pp: 490–509

[49] JENSEN, P.; FRANDSEN, F.; DAM-JOHANSEN, K.; SANDER, B.: Experimental Investigation of the Transformation and Release to Gas Phase of Potassium and Chlorine during Straw Pyrolysis. In: *"Energy & Fuel"* 14 (2000), pp: 1280–1285

[50] JOKINIEMI, J.K.; LAZARIDIS, M.; LEHTINEN, K.E.J.; KAUPPINEN, E.I.: Numerical Simulation of Vapor-Aerosol Dynamics in Combustion Processes. In: *"J. Aerosol Sci."* 25 (1994), pp: 429–446

[51] KAER, S.K.: *Numerical Investigation of Deposit Formation in Straw-fired Boilers*. Aalborg University Denmark, 2001

[52] KEE, R. J.; RUPLEY, F. M.; MILLER, J. A.: *CHEMKIN-II: A Fortran Chemical Kinetics Package for the Analysis of Gas Phase Chemical Kinetics*. Sandia National Laboratories, USA, 1992

[53] KIM, J.P.: *Numerical Modelling of MILD Combustion*. Shaker Verlag, 2008

[54] KNAUS, H.: *Simulation turbulenter reagierender Zweiphasenstroemungen in industriellen Feuerungen mit komplexer Geometrie*. VDI Verlag, 2001

[55] KNAUS, H.; SCHNELL, U.; HEIN, K.R.G.: On the modeling of Coal Combustion in a 550 MWel Coal-Fired Utility Boilers. In: *"Progress in Computational Fluid Dynamics"* 1 (2001), pp: 194–207

[56] KUPKA, T.: *Ash Deposition Problems during Co-Firing of Alternative Fuels in Coal-Fired Power Plants*. Clausthal University of Technology, 2009

[57] KYI, S.; CHADWICK, B. L.: Screening of Potential Mineral Additives for Use as Fouling Preventatives in Victorian Brown Coal Combustion. In: *"Fuel"* 7 (1999), pp: 845–855

[58] LAUBITZ, M. J.: Thermal Conductivity of Powders. In: *"Can. J. Phys."* 37 (1959), pp: 798

[59] LAUNDER, B.E.; SPALDING, D.B.: The Numerical Computation of Turbulent Flows. In: *"Computer Methods in Applied Mechanics and Engineering"* 3 (1974), pp: 269–289

[60] LEISER, S.: *Numerical Simulation of Oxy-Fuel Combustion*. University of Stuttgart, 2010

[61] LEONARD, B. P.: A Stable and Accurate Convective Modelling Procedure Based on Quadratic Upstream Interpolation. In: *"Comp. Meths. Appl. Mech. Eng."* 19 (1979), pp: 59–98

[62] LEPPER, J.: *Numerische Simulation dreidimensionaler Stroemungs-und Verbrennungsvorgaenge unter Verwendung einer Gebietszerlegungsmethode auf Parallelrechnern.* Shaker Verlag, 1998

[63] LINDNER, E.R.; WALL, T.F.: Sodium Ash Reactions during Combustion of Pulverized Coal. In: *"Twenty-Third Symposium (International) on Combustion"* 23 (1990), pp: 1313–1321

[64] LOKARE, S.S.: *A Mechanistic Investigation of Ash Deposition in Pulverized-Coal and Biomass Combustion.* Brigham Young University, 1998

[65] MAGEL, H.C.; SCHNELL, U.; HEIN, K.R.G: Simulation of Detailed Chemistry in a Turbulent Combustor Flow. In: *"Proceedings of the Combustion Institute"* 26 (1996), pp: 67–74

[66] MAGNUSSEN, B.F.: *The Eddy Dissipation Concept, In: XI Task Leaders Meeting.* Energy Conversion in Combustion, IEA, 1989

[67] MAGNUSSEN, B.F.: *Modelling of NO_x and Soot Formation by the Eddy Dissipation Concept.* Int. Flame Research Foundation, 1989

[68] MAJUMDAR, S.: *Development of A Finite-Volume Procedure for Prediction of Fluid Flow Problems with Complex Irregular Boundaries.* Rep.210/T/29, SFB 210, University of Karlsruhe, Germany, 1986

[69] McCABE, W.L.; SMITH, J.C.; HARRIOTT, P.: *Unit Operations of Chemical Engineering, Fifth Edition.* McGraw-Hill, 1993

[70] MUYSHONDT, A.; ANAND, N.K.; McFARLAND, A.R.: Turbulent Deposition of Aerosol Particles in Large Transport Tubes. In: *"Aerosol Science and Technology"* 24 (1996), pp: 107

[71] MWABE, P. O.; WENDT, J. O. L.: Mechanisms Governing Trace Sodium Capture by Kaolinite in A Downflow Combustor. In: *"Proc. Combust. Inst."* 26 (1996), pp: 2447–2453

[72] NEVILLE, M.; SAROFIM, A.F.: The Fate of Sodium during Pulverized Coal Combustion. In: *"Fuel"* 64 (1985), pp: 384

[73] NIELSEN, H. P.: *Deposition and High-Temperature Corrosion in Biomass-Fired Boilers*. Department of Chemical Engineering, DTU Denmark, 1998

[74] NOLL, B.: *Numerische Stroemungsmechanik*. Springer-Verlag, 1993

[75] NOVAKOVIC, A.; LITH, S. C.; FRANDSEN, F. J.; JENSEN, P. A.; HOLGERSEN, L. B.: Release of Potassium from the Systems K-Ca-Si and K-Ca-P. In: *"Fuel"* 23 (2009), pp: 3423–3428

[76] OKSANEN, A.: Detailed Application of EDC-Reactor Technique with Extinction in Gas-Fired Furnaces. In: *"Proceedings of 4th International Conference on Technologies and Combustion for a Clean Environment"* 27 (1997), pp: 8

[77] OLSSON, J.G.; JAEGLID, U.; PETTERSSON, B.C.: Alkali Metal Emission during Pyrolysis of Biomass. In: *"Energy & Fuels"* 11 (1997), pp: 779–784

[78] OSBORN, G.A.: Review of Sulfur and Chlorine Retention in Coal-Fired Boiler Deposits. In: *"Fuel"* 72 (1992), pp: 131–142

[79] PATANKAR, S. V.: *Numerical Heat Transfer and Fluid Flow*. Taylor & Francis, 1980

[80] PRAKASH, A.; BAPAT, A.P.; ZACHARIAH, M.R.: A Simple Numerical Algorithm and Software for Solution of Nucleation, Surface Growth, and Coagulation Problems. In: *"Aerosol Science and Technology"* 37 (2003), pp: 892–898

[81] PUNJAK, W.A.; UBEROI, M.; SHADMAN, F.: High-Temperature Adsorption of Alkali Vapors on Solid Sorbents. In: *"AIChE Journal"* 35 (1992), pp: 1186–1194

[82] PYYKOENEN, J.; JOKINIEMI, J.: Modelling the Impact of Burner Arrangement on Pulverized Coal-Fired Boiler Slagging. In: *"Proc. of the EF Conference, Kona, Hawaii"* (1997)

[83] PYYKOENEN, J.; JOKINIEMI, J.: Modelling Alkali Chloride Superheater Deposition and its Implications. In: *"Fuel Processing Technology"* 80 (2003), pp: 225–262

[84] RAASK, E.: *Mineral Impurities in Coal Combustion*. Springer Verlag, 1985

[85] REICHELT, T.: *Freisetzung gasfoermiger Alkaliverbindungen bei atmophaerischer und druckaufgeladener Verbrennung*. VDI Verlag, 2001

[86] REICHELT, T.; HARTINGER, K.T.; SPLIETHOFF, H.: *In-situ Alkalimessungen an einem atmosphaerischen Flugstromreaktor des IVD unter Einsatz der ELIF-Messtechnik,internal report, University of Stuttgart, Institute of Process Engineering and Power Plant Technology, Stuttgart*. 1995

[87] REZAEI, H. R.; GUPTA, R. P.; BRYANT, G. W.; HART, J. T.; LIU, G. S.; BAILEY, C. W.; WALL, T. F.; MIYAMAE, S.; MAKINO, K.; ENDO, Y.: Thermal Conductivity of Coal Ash and Slags and Models Used. In: *"Fuel"* 79 (2000), pp: 1697–1710

[88] RHIE, C. M.: Transport-Induced Shifts in Condensate Dewpoint and Composition in Multicomponent Systems with Chemical Reaction. In: *"Chemical Engineering Science"* 40 (1985), pp: 177–186

[89] RICHARDS, G. H.; SLATER, P. N.; HARB, J. N.: Simulation of Ash Deposit Growth in a Pulverized Coal-Fired Pilot Scale Reactor. In: *"Energy Fuels"* 7 (1993), pp: 774

[90] RICHTER, S.: *Numerische Simulation der Flugaschedeposition in kohlestaubgefeuerten Dampferzeugern*. VDI Verlag, 2003

[91] RICHTER, S.; STROEHLE, J.; SCHNELL, U.; HEIN, K. R. G.: Application of the 3D Combustion Simulation Code AIOLOS to the Prediction of Ash Deposition in a Pulverized Coal-Fired Utility Boiler. In: *"Proc. 4th Intl. Symposium on Coal Combustion, Beijing, China"* (1999), pp: 369

[92] RISIO, B.; BUNDSCHUH, A.; FOERTSCH, D.; SCHNELL, U.; HEIN, K.R.G.; KLINGE, T.; DERICHS, W.: Industrial-Scale Validation of the 3D Furnace Simulation Code AIOLOS. In: *"Int. Symposium on Computational Technologies for Fluid/Thermal/Chemical Systems with Industrial Applications"* (1998)

[93] ROBINSON, A. L.; BUCKLEY, S. G.; YANG, N.; BAXTER, L. L.: Experimental Measurements of the Thermal Conductivity of Ash Deposits: Part 2: Effects of Sintering and Deposit Microstructure. In: *"Energy & Fuels"* 15 (2001), pp: 75–84

[94] ROSNER, D.E.; NAGARAJAN, R.: Transport-Induced Shifts in Condensate Dewpoint and Composition in Multicomponent Systems with Chemical Reaction. In: *"Chemical Engineering Science"* 40 (1985), pp: 177–186

[95] ROSNER, D.E.; NAGARAJAN, R.: Local Size Distributions of Particles Deposited by Inertial Impaction on a Cylindrical Target in Dust-Laden Streams. In: *"Journal of Aerosol Science"* 26 (1995), pp: 1257–1279

[96] SCHNEIDER, R.: *Beitrag zur numerischen Berechnung dreidimensional reagierender Stroemungen in industriellen Brennkammern*. VDI Verlag, 1998

[97] SCHNELL, U.: *Berechnung der Stickoxidemissionen von Kohlenstaubfeuerungen*. VDI Verlag, 1991

[98] SCHNELL, U.: Numerical Modelling of Solid Fuel Combustion Processes using Advanced CFD-Based Simulation Tools. In: *"International Journal of Progress in Computational Fluid Dynamics"* 1 (2001), pp: 208–218

[99] SCHNELL, U.; RICHTER, S.; HEIN, K. R. G.: Numerical Simulation of Slagging and Fouling in a Pulverized Coal-fired Utility Boiler. In: *"United Engineering Foundation Conference on Heat Exchanger Fouling, Davos, Switzerland"* (2001)

[100] SCHOEN, J.: *Effects of Temperature on the Liberation of Cl and Alkalis from Coal.* British Coal Utilization Research Association, 1956

[101] SCHUERMANN, H.; MONKHOUSE, P.B.; UNTERBERGER, S.; HEIN, K.R.G.: In Situ Parametric Study of Alkali Release in Pulverized Coal Combustion: Effects of Operating Conditions and Gas Composition. In: *"Proceedings of the Combustion Institute"* 31 (2007), pp: 1913–1920

[102] SHUEN, J.S.; CHEN, L.D.; FAETH, G.M.: Evaluation of a Stochastic Model of Particle Dispersion in a Turbulent Round Jet. In: *"AIChE"* 29 (1983), pp: 167–170

[103] SRINIVASACHAR, S.; HELBLE, J.J.; HAM, D.O.; DOMAZETIS, G.: A Kinetic Description of Vapor Phase Alkali Transformation. In: *"Progr. Energy Comb. Sci."* 16 (1990), pp: 303–309

[104] STEFFIN, C. R.: *Freisetzung und Einbindung von Alkalien bei der Verbrennung und Vergasung von Kohle unter Druck.* Shaker Verlag, 1999

[105] STOEVER, B. C.: *Experimentelle und Numerische Betrachtung der Vorgaenge bei der Demineralisierung eines festen Energietraegers.* Dortmund University, 2010

[106] STONE, H. J.: Iterative Solution of Implicit Approximations of Multidimensional Partial Differential Equations. In: *"SIAM J. Numer. Anal."* 5 (1968), pp: 530–558

[107] STROEHLE, J.: *Spectral Modelling of Radiative Heat Transfer in Industrial Furnaces.* Shaker Verlag, 2003

[108] STROEHLE, J.; KNAUS, H.; SCHNELL, U.; HEIN, K.R.G.: A Radiation Model for the Numerical Simulation of Coal-Fired Furnaces using Body-Fitted Grids. In: *"Combust. Sci. Technol."* 153 (2000), pp: 127–139

[109] STROEHLE, J.; RICHTER, S.; SCHNELL, U.; HEIN, K.R.G.: The Effect of Fouling and Slagging on Heat Transfer in Coal-Fired Utility Boilers. In: *"Proc. of the 5th European Conference on Industrial Furnaces and Boilers"* (2000)

[110] TALBOT, L.; CHENG, R.K.; SCHEFER, R.W.; WILLIS, D.R.: Thermophoresis of Particles in a Heated Boundary Layer. In: *"J. Fluid Mech."* 101 (1980), pp: 737

[111] TOMECZEK, J.; PALUGNIOK, H.; OCHMAN, J.: Modelling of Deposits Formation on Heating Tubes in Pulverized Coal Boilers. In: *"Fuel"* 83 (2004), pp: 213–221

[112] TOULOUKIAN, Y. S.: *Thermophysical Properties of High Temperature Solid Materials.* The MacMillan Company, New York, 1967

[113] TOULOUKIAN, Y. S.; POWELL, R. W.; HO, C. Y.; KLEMENS, P. G.: Thermal Conductivity, Nonmetallic Solids. In: *"Thermophysical Properties of Matter"* 2 (1970)

[114] TSUCHIYA, K.; KAMIYA, K.; MATSUI, H.: Studies on the Oxidation Mechanism of H_2 based on the Direct Examination of the Key Reactions. In: *"Int. J. Chem. Kinet."* 29 (1997), pp: 57–66

[115] VOS, J.B.: *The Calculation of Turbulent Reacting Flows with a Combustion Model based on Finite Chemical Kinetics.* TU Delft, 1987

[116] WALL, S.; JOHN, W.: Impact Adhesion Theory Applied to Measurements of Particle Kinetic Energy Loss. In: *"Aerosol Science and Technology"* 9 (1988), pp: 789–792

[117] WALL, S.; JOHN, W.; WANG, H. C.; GOREN, S. L.: Measurement of Kinetic Energy Loss for Particles Impacting Surfaces. In: *"Aerosol Science and Technology"* 12 (1990), pp: 926–946

[118] WALL, T. F.; BHATTACHARYA, S. P.; ZHANG, D. K.; GUPTA, R. P.; HE, X.: The Properties and Thermal Effects of Ash Deposits in Coal-Fired Furnaces. In: *"Prog. Energy Combust. Sci."* 19 (1993), pp: 487

[119] WALSH, P. M.; SAYRE, A. N.; LOEHDEN, D. O.; MONROE, L. S.; BEER, J. M.; SAROFIM, A. M.: Deposition of Bituminous Coal Ash on an Isolated Heat Exchanger Tube: Effects of Coal Properties on Deposit Growth. In: *"Prog. Energy Combust. Sci."* 16 (1990), pp: 327–346

[120] WARNATZ, J.; MAAS, U.; DIBBLE, R.W.: *Combustion.* Springer Verlag, 2001

[121] WEI, X.L.; LOPEZ, C.; PUTTKAMER, T. V.; SCHNELL, U.; UNTERBERGER, S.; HEIN, K.R.G.: Assessment of Chlorine-Alkali-Minerals Interactions during Co-Combustion of Coal and Straw. In: *"Energy & Fuel"* 16 (2002), pp: 1095–1108

[122] WEN, C.S.; COWELL, L.H.; SMIT, F.J.; BOYD, J.D.; LECREN, R.T.: Coal Alkali Retention in a Slagging Combustor. In: *"Fuel"* 71 (1992), pp: 219

[123] WESSEL, R.A.; RIGHI, J.: Generalized Correlations for Inertial Impaction of Particles on a Circular Cylinder. In: *"Aerosol Science and Technology"* 9 (1988), pp: 29–60

[124] WIBBERLEY, L. J.: Effect of Coal Composition on Deposit Formation in PF Boilers. In: *"An Extensive Course on the Characterisation of Steaming Coals, Institute of Coal Research, NSW, Australia"* (1985), pp: 1–9

[125] WIJNGAART, R. J. F. V.: *Composite Grid Techniques and Adaptive Mesh Refinement in Computational Fluid Dynamics*. Report ClaSSiC-90-07, Department of Computer Science, Stanford University, USA, 1990

[126] WILD, T.: *Demineralisierung und Mechanisch/Thermische Entwaesserung von Braunkohlen und Biobrennstoffen*. Dortmund University, 2006

[127] WORNAT, M.J.; HURT, R.H.; YANG, N.Y.C.; HEADLEY, T.J.: Structural and Compositional Transformations of Biomass Chars during Combustion. In: *"Combustion and Flame"* 100 (1995), pp: 131–143

[128] WU, B.; JAANU, K.K.; SHADMAN, F.: Multi-Functional Sorbents for the Removal of Sulfur and Metallic Contaminants from High-Temperature Gases. In: *"Environ. Sci. Technol."* 29 (1995), pp: 1660–1665

[129] ZELKOWSKI, J.: *Kohleverbrennung*. VGB Fachbuchreihe Band 8, 1986